6. PHYSICAL & APPLIED CHEMISTRY

6.1. Lectures

L01 PHOTOCATALYTIC PROCESSES AND THEIR UTILIZATION

MICHAL VESELÝ, JIŘÍ ZITA, MÁRIA VESELÁ,
JANA CHOVANCOVÁ, JANA CHOMOUCKÁ
and PETRA MOŽÍŠKOVÁ
Faculty of Chemistry, Brno University of Technology, Purkyňova 118, 612 00 Brno, Czech Republic, vesely-m@fch.vutbr.cz

Introduction

The photocatalytic method is based on the reactive properties of an electron-hole pair generated in semiconductor particles (TiO_2). Under illumination by light of energy greater than the semiconductor bandgap[1] electron is excited to the conduction band and both the hole in valence band and the electron in conduction band migrate to the particle surface. If no recombination occurs, this charge carriers can react with adsorbed molecules, e. g. with water, hydroxyl anion, oxygen or organic compounds. The hydroxyl radical generation can be expressed by following equations.

$$TiO_2 \xrightarrow{h\nu} TiO_2\,(e^-_{cb}, h^+_{vb}) \rightarrow \text{recombination}$$

$$TiO_2\ \ (h^+_{vb}) + H_2O_{ads} \rightarrow TiO_2 + HO^\bullet_{ads} + H^+$$

$$TiO_2\ \ (h^+_{vb}) + HO^-_{ads} \rightarrow TiO_2 + HO^\bullet_{ads}$$

$$TiO_2\ \ (e^-_{cb}) + O_{2ads} + H^+ \rightarrow TiO_2 + HO^\bullet_2 \rightleftarrows O^{\bullet -}_2 + H^+$$

$$TiO_2\ \ (e^-_{cb}) + HO^\bullet_2 + H^+ \rightarrow TiO_2 + H_2O_2$$

$$TiO_2\ \ (e^-_{cb}) + H_2O_2 \rightarrow TiO_2 + HO^\bullet + HO^-$$

$$2\ \ HO^\bullet_2 \rightarrow H_2O_2 + O_2$$

$$O^{\bullet -}_2 + H_2O_2 \rightarrow HO^\bullet + O_2 + HO^-$$

$$H_2O_2 \xrightarrow{h\nu} 2\ \ HO^\bullet$$

Furthermore, the organic molecule in close contact to TiO_2 undergoes oxidation, what can be described schematically:

$$HO^\bullet + D_{ads} \rightarrow D_{ox}$$

The photogenerated electron can reduce adsorbed species.

$$TiO_2(e^-_{cb}) + A_{ads} \longrightarrow TiO_2 + A^-_{ads}$$

where A can be oxygen or metallic ion with suitable redox potential and undergo transformation to other oxidation state:

$$M^{n+} + TiO_2(ze^-_{cb}) \rightarrow M^{(n-z)+}$$

Photocatalytic metal ion reduction

The photocatalytic processs can be used for metal ions reduction by i) direct way using photogenerated electrons, ii) indirect reduction using reactive intermediate created by reaction with photogenerated holes, iii) oxidative way of metal removal (Pb^{2+}, Mn^{2+} nebo Tl^+).

One of the most important parameters affecting the reduction process is the redox potential of metal/metallic ion pair. Only those pairs with more positive potential than the edge of TiO_2 conduction band can be reduced. The difference between these potentials[2] should be greater than 0.4 V.

The reactivity of metal ions on TiO_2 differs and decreases in the order:

$$Ag > Pd > Au > Pt >> Rh >> Ir >> Ni = Fe = 0$$

The metallic ion is reduced to metal and is deposited on the semiconductor particle surface. The metallic species can be generally extracted from the slurry by mechanical or chemical procedures at the end of the process.

At our department we are studying the photocatalytic process of metal ions reduction from water solution. On the immobilized titanium dioxide we have reduced silver, copper, mercury and nickel in a batch and in a flow reactor in presence of various electron donors. We have achieved rapid decrease of metal ion concentration in course of several minutes (silver and mercury ions) or several tens of minutes (copper ions). Their concentration was estimated under 1 ppm (silver and mercury ions) and 3 ppm (copper ions).

Photocatalytic reactors

Generally, the photocatalyst can be used in suspension or immobilized on inert support. Although the photocatalyst in powder form has an advantage of greater reactive surface compared to the immobilised one, required consecutive separation of colloidal particles is expensive and time-consuming and represents the main drawback. The photocatalyst surface becomes active only if the particles are irradiated. The irradiation of all photocatalyst particles in suspension is difficult, because of scattering and shadowing effects, mainly in greater distance from light source. It means that the depth of radiation penetration through the suspension is limited and this shadowing effect can dramatically decrease the photocatalytic reaction rate. On the other hand, it is possible to find such arrangement in immobilized system, in which there are all immobilized particles irradiated. Therefore, the elimination of TiO_2 particles is not necessary. The main disadvantage of this system is reduced mass transport.

In an optimally arranged reactor, the photocatalyst is fixed on its support in such a way to maximize the irradiated area. Nowadays, new possibilities of photocatalyst immobilization are studied. The supports are reactor walls, ceramic and glass tiles[3], active carbon black, metallic grains, crystals[4], zeolites[5] or glass fibres.

One of the most important photocatalyst layer parameter seems to be its thickness. If the layer is too thick, most of electrons and holes are generated relatively deep in layer and therefore they cannot reach the surface and take place in reaction within their lifetime. If the layer is too thin, only a small part of radiation would be absorbed and this can cause the photocatalytic efficiency decreasing again.

Photocatalytic oxidation

Considering photogenerated species reactivity, various applications could be offered (Fig. 1.): water and air treatment, bactericidal effect, self-cleaning effect connected with super-hydrophilicity effect. At our department, we are studying the water purification and antibacterial processes and TiO_2 thin layer preparation leading to self-cleaning properties of these layers.

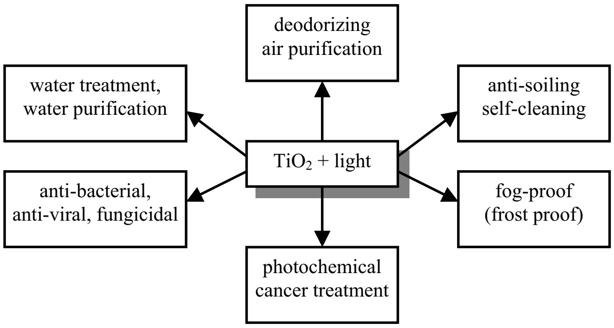

Fig. 1. **Major application areas of titanium dioxide photocatalysis[1]**

Water purification process

An organic water pollutant can be often transformed to more dangerous products, mainly chlorinated ones[6] by ordinary way of waste water treatment. The main advantage of photocatalytic process seems to be its reaction mechanism leading to a complete mineralization of organic compound to water and carbon dioxide. As other by-product, mineral acid can appear, if the degraded molecule contains halogen or sulphuric groups SO_2 and SO_4. The non-selectivity of this process could be possible drawback. On the other hand, simple products, which are often easily biodegradable, are created. The photocatalytic reactions can be used for a wide range of compounds. Successfully degraded organic compounds in water solution or suspension include phenol, cresol, chlorinated hydrocarbons derivatives, nitro- and amino derivatives, azo dyes, wide spectrum of pesticides and many others.

Anti-bacterial effect

The photocatalytic processes can be used also for water disinfection. For example, great difficulties with water quality in swimming pools were described. In these facilities, the occurrence of pathogenic yeasts, resistant to chlorine, should be prevented by another methods than the commonly used. Arising OH radicals on irradiated photocatalyst surface attack cell membrane and cause a quick cell death[7]. At our department, we have been studying the process of yeast cell killing on photocatylytical active surfaces and in flow systems. The strains *Hansenula anomala, Candida tropicalis and Saccharomyces cerevisiae* were studied.

The last mentioned strain was used for comparison, as it is widely utilised yeast in food industry. Yeast suspension dropped on the irradiated TiO_2 layer very sensitively reacts to sweeping conditions caused by the reactive radicals and as the result, rapid changes in yeast viability can be observed. This process was found to be the most rapid in *Candida tropicalis* strain, which is known to be pathogenic and occurs in swimming pools.

Self-cleaning effect

Surfaces of many materials repel water to some extent, which can be expressed by water contact angle. On glass and other inorganic materials, water shows contact angle between 2 and 30 degrees, on surfaces of plastic materials between 70 and 90 degrees and on water repeling plastics can the contact angle be greater than 90 degrees. A thin TiO_2 film with suitable additives shows the water contact angle several tens of degrees.

After irradiation of TiO_2 surface, the observed water contact angle decreased to zero, that means a complete wettability. This phenomenon is described as super-hydrophilicity. Without following irradiation, this persists over the course of several days before it turns back to the initial behaviour. The super-hydrophilicity is possible to restore by irradiation. But the photoinduced hydrophilicity mechanism is quite different from common photocatalytic reactions.

The wettability changes are caused by the changes in titanium dioxide surface lattice structure. The hydrophilicity conversion occurs after titanium dioxide photoexcitation and electron-hole pair generation. The electrons tend to reduce surface ions Ti^{4+} to Ti^{3+}, which is accompanied by oxygen vacancy creation and dissociative adsorption of water on the vacancies.

At our department we are dealing with titanium dioxide thin layers and transparent layers preparation on glass support by sol-gel method. It was found that this thin film shows a rapid water angle decreasing and after several minutes, the drops are getting spread and this surface becomes wettable. UV dosage required to this change was 72 mJ cm^{-2}. The prepared layers were used for photocatalytic yeast killing. The significant hydrophilicity increasing combined with a high photogenerated radical reactivity could be used for organic molecules degradation and their removal from this surface, leading to a self-cleaning ability.

REFERENCES

1. Fujishima A., Hashimoto K., Watanabe T., *TiO_2 Photocatalysis. Fundamentals and Applications*. BKC Inc. 1999, Tokyo.
2. Litter M. I.: Applied Catalysis B: Enviromental *23*, 89 (1999).
3. Boire P., Talpaert X.: U. S. Patent 6,103, 363.
4. Hermann J. M., Tahiti H., Ait-Ichou Y., Lassaletta G., Ginzáles-Elipe A. R., Fernandéz A.: Applied Catalysis B: Environmental *13*, 219 (1997).
5. Noorjahan M., Kumari V. D., Subrahmanyam M., Boule P.: Applied Catalysis B: Environmental *47*, 209 (2004).

6. Wei C., Lin W, Zainal Z., Williams N. E., Zhu K., Kruzic, A. P., Smith R. L., Rajeshwar K., Env. Sci. Technol. *28*, 934 (1994).
7. Herrera Melián J. A, Doña Rodríguez J. M., Viera Suárez A., Tello Rendón E., Valdés do Campo C., Arana J., Pérez Peña J.: Chemosphere *41*, 323 (2000).

L02 PHOTOCATALYTIC DEGRADATION OF HERBICIDES ATRAZINE USING TIO$_2$ SYSTEM

JOSEF KRÝSA[a] and JAROMÍR JIRKOVSKÝ[b]
[a]*Institute of Chemical Technology, Department of Inorganic Technology, Technická 5, CZ-166 28 Prague 6, Czech Republic, josef.krysa@vscht.cz,* [b]*Jaroslav Heyrovský Institute of Physical Chemistry, Academy of Sciences, Dolejškova 3, CZ-182 23 Prague 8, Czech Republic*

Introduction

Atrazine (2-chloro-4-ethylamino-6-isopropylamino-1,3,5-triazine) belongs to the group of symmetric triazine derivatives. It is used for weed pre- and post-emergence control, particularly in maize crops. It is not readily biodegradable, it persists in soil and even reaches the groundwater. Its solubility in water is low (1.61.10^{-4} M) and does not depend on pH[1].

Pesticides contaminate surface water mainly by washing from fields and crop-plant and by wind during aerial spraying. They may disrupt biologic equilibrium in streams due to their toxic effect on biocenosis. They can also unfavorably influence the self-cleaning ability of water, its odour and taste. Surface water is still treated and distributed as drinking water to more than half of the population in the Czech Republic supplied from public water conduits. The concentration of atrazine in drinking water varies in the range of 50–250 ng l^{-1} (ref.[2]).

Among classical methods, only adsorption on granulated activated carbon[3] is sufficiently efficient in removal of atrazine. However, it only passes into solid phase but its destruction does not take place. For this reason, so-called Advanced Oxidation Processes (AOP) are developed that generate a more reactive agent, the hydroxyl radical. These comprise either homogeneous or heterogeneous systems.

The heterogeneous photocatalytic systems are based on the light absorption by semiconductor particles, typically of TiO$_2$. Only photons with higher energy than the band gap energy can be absorbed. Corresponding maximum wavelength, depending on the crystallographic modification of TiO$_2$, is about 387 nm (anatase) or 413 nm (rutile). Consequently, pairs of separated positive holes (h_{VB}^+) in valence band and (e_{CB}^-) electrons in conduction band are generated. These charge carriers mainly rapidly recombine inside the particles but also partly migrate to the surface and can be directly transferred onto adsorbed molecules of electron donors (D) or electron acceptors (A):

According to their chemical nature, the trapped charges react with various dissolved components. The trapped positive hole, like surface bound OH radical[4], typically oxidizes organic compounds and thus induces their further oxidative degradation while the trapped electron, like surface bound Ti(III), typically reduces dioxygen to superoxide radical anion. On this basis, TiO$_2$ acts as a photocatalyst, being renewed after each redox circuit.

The photocatalytic degradation of atrazine has been extensively studied[5,6,7,8,9]. Maurino et al.[5] examined photocatalytic degradation of atrazine under simulated solar radiation in aqueous suspensions of various semiconductor powders (TiO$_2$, ZnO, WO$_2$, SnO$_2$ and Fe$_2$O$_3$). Among them, TiO$_2$ was found most efficient. Photocatalytic degradation of atrazine in TiO$_2$ suspension was successfully carried out in a large modular flow through system under solar light[6]. The degradation led to complete mineralization of alkyl substituent giving 2,4,6-trihydroxy-1,3,5-triazine (cyanuric acid) as a final product.

The aim of this study was to compare kinetics of oxidative photodegradation of herbicides atrazine (2-chloro-4-ethylamino-6-isopropylamino-1,3,5-triazine) in suspensions of TiO$_2$. Plate photoreactor with immobilized layer of TiO$_2$ was applied for 3rd step of raw water treatment. Atrazine was chosen as a model pollutant because of its occurrence in surface waters and well-known reaction mechanism[5,6,7,8,9].

Experimental

The used TiO$_2$ photocatalysts were P25 (Degussa) and quantum-sized colloids synthesized from TiCl$_4$ and FeCl$_3$ (both Fluka)[10]. All solutions were prepared with deionized ultrapure water (ρ = 18.2 MΩ cm). pH measurements were carried out with an ORION pH meter to 0.01 unit.

The irradiation experiments were performed in a self-constructed photoreactor placed in an elliptical stainless steel chamber. A high pressure mercury lamp surrounded by a glass filter bulb (Philips HPW type 125 W), which dominantly (93 %) emits radiation at 365 nm (so called "black light"), was placed in one of the focal axes while a water-jacketed Pyrex tube (diameter of 2.8 cm), as a photoreactor, was centered in the other one. The irradiated solutions or suspensions were magnetically stirred during whole experiment. Using the ferrioxalate actinometry, an average light intensity entering the irradiated solution (independently of volumes between 70 and 100 ml) was determined to be 4.5 . 10^{-6} einstein dm^{-3} s^{-1}.

The batch mode plate photoreactor were employed with a flowing film of aqueous solution irradiated with ultraviolet sun bed tubes (Eversun L40W/79K, Osram) emitting mainly in wavelengths range between 310 and 390 nm (maximum at 355 nm) (Fig. 1.). The incident photon flux was determined using filter transmitting light in the wavelength range 310–390 nm and photodiode HAMATSU (S 1337–BQ) as 7.1 . 10^{-5} einstein m^{-2} s^{-1} (3.2 . 10^{-6} einstein dm^{-3} s^{-1}).

A particulate TiO$_2$ layer was prepared on a glass plate (w = 0.3 m, L = 0.6 m) by sedimentation from an aqueous suspension of TiO$_2$ (P25, Degussa, (10 g dm^{-3}) with subsequent drying and annealing at 300 °C. The solution of atrazine was pumped from the holding tank employing a centrifugal pump (Nova, Sicce, Italy) to the higher reservoir. The overflow produced a liquid film flowing over the glass plate. The solution was collected in the lower reservoir and returned into the holding tank. The flow rate Q, $10.0 . 10^{-5}$ m^3 s^{-1} corresponding to 6 dm^3 min^{-1} was controlled by rotameter.

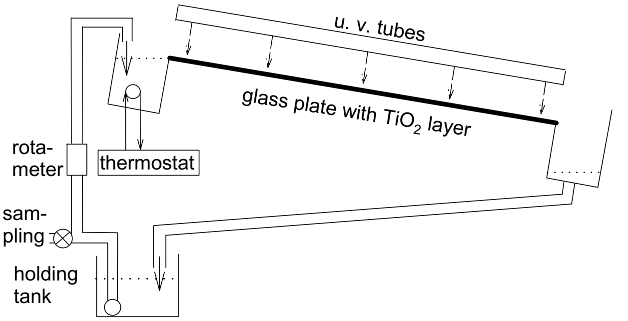

Fig. 1. **Schematic representation of a batch mode plate reactor with flowing film of aqueous solution, glass plate with TiO_2 layer – width, w = 0.3 m, length 0.6 m, inclination angle = 10°, distance between u. v. tubes and TiO_2 layer = 0.125 m**

Probes of reaction mixtures (0.5 ml) were taken at appropriate irradiation times. The HPLC analyses were carried out on a Beckman set with 163 Variable Wavelength Detector. A Merck column LiChroCART 250-4 filled with LiChrosphere 100 RP-18 (5 μm) together with mobile phases acetonitrile/water (2:3; v/v) or (1:9; v/v) and pure water were used. Injection loop was 55 μl, flow rate 1 ml min^{-1} and detection wavelength 220 nm were applied.

Results

A comparative kinetic study of photocatalytic degradation of atrazin was performed using heterogeneous aqueous suspensions of various TiO_2 photocatalysts (commercial material P25 of Degussa, synthesized quantum-sized particles either pure Q-TiO_2 or doped Q-TiO_2 (1 % Fe^{3+})). To quantify the degradation rates in particular reaction systems, the corresponding experimental dependences were treated as pseudo-unimolecular reactions (Table I). It is worth to note that the applied kinetic model approximated the measured dependences of the atrazine concentration on irradiation time very well (see Fig. 2.).

As shown in Table I colloidal suspensions of quantum-sized particles Q-TiO_2 were found more than one order of magnitude less photoactive than the P25 slurry. It was apparently due to the generally higher probability of recombination of separated positive holes with electrons in the small interior of Q-TiO_2 particles (diameter 2–3 nm) than inside larger P25 particles (30 nm). The rate constants for two differently concentrated colloidal suspensions of 3 mM Q-TiO_2 ($3.18 . 10^{-5}$ s^{-1}) and 9 mM Q-TiO_2 ($1.11 . 10^{-4}$ s^{-1}) increased almost proportionally due to the Q-TiO_2 concentration. Doping of the quantum-sized particles by Fe^{3+} caused a red shift of the semiconductor absorption but influenced the photocatalytic activity negatively.

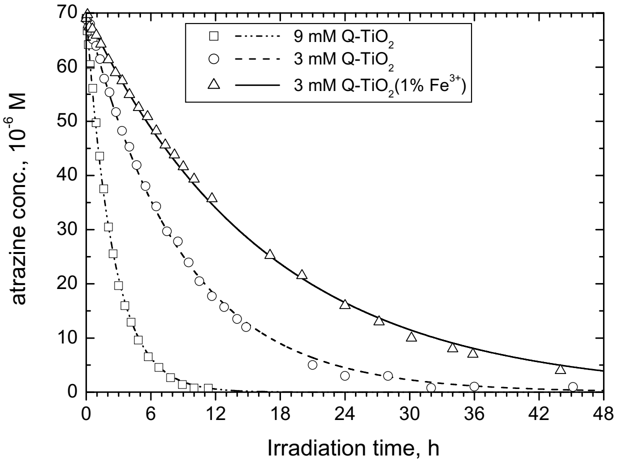

Fig. 2. **Kinetics of photodegradation of 0.069 mM atrazine in various heterogeneous TiO_2 systems**

Table I
Comparison of the first order rate constants for photodegradation of atrazine in various heterogeneous systems. Initial concentration of atrazine was 0.069 mM (λ = 365 nm)

System	k [s^{-1}]
9 mM TiO_2 P25 (Degussa)	$(1.49 \pm 0.04) . 10^{-3}$
9 mM Q–TiO_2 + 10 mM $HClO_4$	$(1.11 \pm 0.02) . 10^{-4}$
3 mM Q–TiO_2 + 10 mM $HClO_4$	$(3.18 \pm 0.04) . 10^{-5}$
3 mM TiO_2 (1 % Fe^{3+}) + 10 mM $HClO_4$	$(1.67 \pm 0.02) . 10^{-5}$

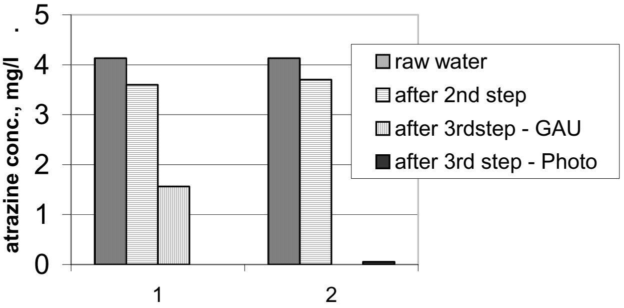

Fig. 3. **Atrazine concentration in the course of raw water treatment**

Photocatalytic degradation was applied as a third step of drinking water treatment and compared with adsorption on granulated active carbon. Plate phiotoreactor with flowing film of the solution was used (Fig. 1.). The course of raw water treatment simulating treatment in water stations is shown in Fig. 3. Stock solution of atrazine in destilled water was added to raw water before treatment to reach staring concentration around 3–4 mg l^{-1} (ref.[11]). While the classic two-step treatment (coagulation and filtration) did not practically change the starting atrazine concentration the filtration through active carbon caused its decrease by one order of magnitude to 0.5–0.2 mg l^{-1} and the photocatalysis by two orders of magnitude to 0.05 mg l^{-1}. However, a prolonged treatment process and increased operational costs are disadvantages of the photocatalytic method.

This research was supported by the Ministry of Education, Youth and Sports of the Czech Republic (project number MSM 6046137301).

REFERENCES

1. Ward T. M., Weber J. B., J. Agric. Food Chem. *16*, 959 (1968).
2. Kužílek V., Vodní hospodářství *8*, 247 (1997), (in Czech).
3. Knappe D. R. U., Snoeyink V. L., Roche P., Prados M. J., Bourbigot M. M., Journal AWWA *91*, 97 (1999).
4. Rajeshwar K., J. Appl. Electrochem. *25*, 1067 (1995).
5. Maurino V., Minero C., Pelizzeti E. and Serpone N., in: *Fine Particles Science and Technology* (Pelizzeti E., ed.), p. 707. Kluwer Academic Publishers 1996.
6. Minero C., Pelizzeti E., Malato S., Blanco J., Solar Energy *56*, 411 (1996).
7. Texier I., Ouazzani J., Delaire J., Giannoti Ch., Tetrahedron *55*, 3401 (1999).
8. Pellizeti E., Maurino V., Minero C., Carlin V., Pramauro E., Zerbinatti O., Toscato M. L., Environ. Sci. Technol. *24*, 1559 (1990).
9. Serpone N., Calza P., Salinaro A., Cai L., Emeline A., Hidaka H., Horikoshi S., Pellizeti E. : *Proceedings of the symposium on Photoelectrochemistry* (K. Rajeshwar, L. M. Peter, A. Fujishima, D. Meissner, and M. Tomkiewicz, ed.), p. 301. Proceedings Volume 97–20, The Electrochemical Society, Inc. 1997.
10. Krýsová H., Jirkovský J., Krýsa J., Mailhot G. and Bolte M., Appl.Catalysis B: Environ., *40*, 1 (2003).
11. Krýsová H., Krýsa J., Hubáčková J., Tříska J., Jirkovský J., Chemické listy, *99*, 179 (2005), (in Czech).

L03 PHOTOCATALYTIC PROCESSES ON DIFFEREN TYPES OF IMMOBILIZED TIO2

JIŘÍ ZITA, PETRA MOŽÍŠKOVÁ,
MARKÉTA PETEROVÁ, JANA CHOMOUCKÁ,
JANA CHOVANCOVÁ and MICHAL VESELÝ
Brno University of Technology, Faculty of Chemistry, Institute of Physical and Applied Chemistry, Purkyňova 118, 612 00 Brno, Czech Republic, zita@fch.vutbr.cz

Introduction

One of the most important aspects of environmental photocatalysis is the availability of a material such as titanium dioxide, which is close to being an ideal photocatalyst in several respects. For example, it is relatively inexpensive, highly stable chemically, and the photogenerated holes are highly oxidizing. In addition, photogenerated electrons are reducing enough to produce superoxide from dioxygen.

The heterogenous photocatalytic process is a complex sequence of reactions, that can be expressed by the following set of simplified Equations:

$$TiO_2 \xrightarrow{h\nu} TiO_2\left(e^-_{cb}, h^+_{vb}\right) \longrightarrow \text{recombination}$$

$$TiO_2(h^+_{vb}) + H_2O_{ads} \longrightarrow TiO_2 + HO^\bullet_{ads} + H^+$$

$$TiO_2(h^+_{vb}) + HO^-_{ads} \longrightarrow TiO_2 + HO^\bullet_{ads}$$

$$TiO_2(h^+_{vb}) + D_{ads} \longrightarrow TiO_2 + D^+_{ads}$$

$$HO^\bullet + D_{ads} \longrightarrow D_{oxid}$$

$$TiO_2(e^-_{cb}) + A_{ads} \longrightarrow TiO_2 + A^-_{ads}$$

where A represents acceptor of electrons (metal ion) and D donor of electrons.

The hole (h^+_{vb}) is a potential oxidant and can oxidize organic molecules at the surface, eventually mineralize them to CO_2. Similary, the hole can oxidize water or hydroxide ions to form hydroxyl radicals $OH^\bullet$, which are also efficient oxidants of organic molecules. In order for the oxidation processes to proceed effectively, the photogenerated electrons (e^-_{cb}) must also be removed from the TiO_2 particle[1].

Typically, oxygen is used as the electron acceptor. Oxygen can be reduced to the superoxide, $O_2^{\bullet-}$, which may also participate in the degradation reactions of the organic molecules, or be further reduced to hydrogen peroxide or water:

$$TiO_2(e^-_{cb}) + O_2 + H^+ \longrightarrow TiO_2 + HO_2^\bullet \rightleftharpoons O_2^{\bullet-} + H^+$$

$$HO_2^\bullet + TiO_2(e^-_{cb}) + H^+ \longrightarrow H_2O_2$$

$$2HO_2^\bullet \longrightarrow H_2O_2 + O_2$$

$$H_2O_2 + O_2^{\bullet-} \longrightarrow HO^\bullet + O_2 + HO^-$$

$$H_2O_2 + h\nu \longrightarrow 2HO^\bullet$$

$$H_2O_2 + TiO_2(e^-_{cb}) \longrightarrow HO^\bullet + HO^-$$

A variety of organic molecules can be photocatalytically oxidized and eventually mineralized according to the following general reaction:

$$\text{organic molecule} + O_2 \xrightarrow{h\nu \geq E_g\text{, semiconductor}}$$

$$\xrightarrow{h\nu \geq E_g\text{, semiconductor}} CO_2 + H_2O + \text{mineral acids}$$

As shown in the equations, the process of photocatalytic removal of metal ions and degradation of organic compounds can be use for water and air treatment.

Immobilization of TiO_2

Titanium dioxide is the mostly used photocatalyst. It is polymorphous, that is, it exists in three crystal structures, namely rutile, anatase, and brookite. Anatas has been found, in the most of the cases, to be photocatalytically more active than other modifications. The most popular commercial form of TiO_2 is produced by the German company Deggusa. The product name is Aeroxide P25. However, the manipulations of powdered semiconductors and their removal from water (by filtration and centrifugation) are difficult and recent research has focused on the preparation of active immobilized photocatalysts.

TiO_2 can be deposited in the form of thin coatings on different types supports, like glass, stainless steel, quartz, and different types of fibres. Preparation of the films can be described with two different mechanisms. The first is physical mechanism, which depends on fixation of TiO_2 particles to the surface of the support by using proper binder. The second is chemical mechanism, which depends on the direct reaction between compound containing required metal (in the most cases metal-alkoxide) and surface of the support where the active layer of the metal catalyst is created.

Photoactive thin-film catalyst is widely prepared at ambient temperatures using technique called sol-gel process. Basic parts of these films consist of organometal compounds, frequently metal alkoxides or colloidal metal solutions. During the sol-gel process, the sol is converted to the gel and then the process of changing the gel to the metal oxide proceeded.

The possibility of preparation films and materials of a particular purity, homogeneity and constitution is the main advantage. The useful catalyst modification of by dopants is possible by this sol-gel technique[2].

TiO_2 immobilized on PVA thin film

This thin film was prepared from 5 % poly(viny lalcohol) water solution modified with glycidylmethacrylate (PVA-GMA). For better diluting of the PVA-GMA, 50 cm^3 of ethanol was added. After complete dissolution, modification and photoinicator addition, TiO_2 powder was added and the mixture was than sonicated for 15 minutes. From this solution the thin film was prepared by filling into the form and drying. After this procedure the film was cured by UV radiation for 3 minutes from each side. Thus prepared film was used in the photocatalytic reactor close to the UV light source. The other way how to immobilize TiO_2 on to the PVA-GMA is not putting it exactly in to the solution, but after the film is created, the TiO_2 suspension (1 g of TiO_2 dispersed in 5 cm^3 of water) is coated onto the film. After drying, the film is then cured by UV radiation as is mentioned above.

TiO_2 immobilized on paper and glass from suspension

The suspension of TiO_2 was made from 5 g of powder TiO_2 and 200 cm^3 of water. The solution was sonicated for 15 minutes. In the case of paper carrier, the paper was dipped into the solution and dried for 3 hours at the temperature 100 °C. In the case of a glass plate (5 × 5 cm), the plate was coated by dip-coating (for 30 seconds) and spin-coating (200 rpm) by the prepared suspension, dried for 3 hours at the temperature 100 °C and than calcinated for 1 hour at 500 °C.

TiO_2 immobilization by sol-gel process on glass

Two types of sols were prepared: the first of titanium isopropoxide (TIP), the second of titanium tetrabutoxide (TTB). The preparation of the immobilized films is described in detail in the article written by Jana Chovancová, which is published in this proceeding.

Photocatalytic reactions

Reduction of Cu^{2+}

Because of relatively high rate of Cu^{2+} ions reduction in the presence of ethanol[2], we have chosen this reaction solution for characterization of our immobilized TiO_2 layers. The reactions have proceeded in presence of 0.05 M ethanol and

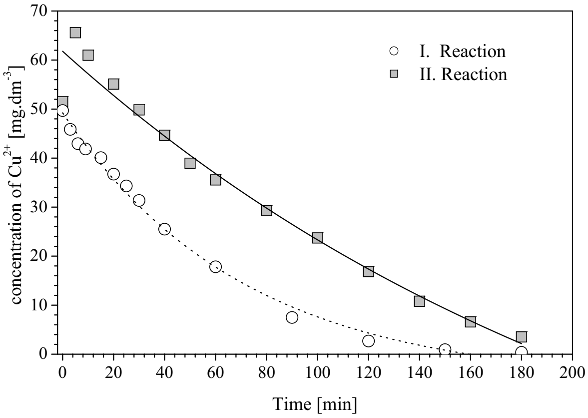

Fig. 1. **Two reactions of the photocatalytic Cu^{2+} ions reduction on the paper carrier**

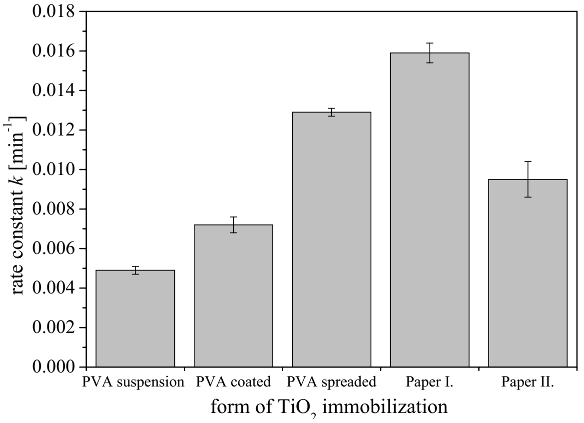

Fig. 2. **The formal first order rate constants of the photocatalytic reduction of Cu^{2+} ions on different forms of immobilized TiO2 catalyst**

acetate buffer solution setting pH at value 4 (295.2 cm^3 of 0.2 M acetic acid and 7.8 cm of 0.2 M sodium acetate). The reactions were performed in immersion-well reactor. The reduction of Cu^{2+} ions was tested on TiO_2 PVA-GMA thin film (one reaction on each carrier) and on TiO_2 immobilized on paper (two reactions on the same carrier Fig. 1.).

We can see, that the first reaction on paper carrier is quite fast ($k = 0.159\ min^{-1}$), but when the second reaction started, a part of metal Cu^0 (created in the previous reaction) has released from the carrier back into the reaction solution (as we can see increase the Cu^{2+} ions concentration in the first couple of minutes) and the rate constant of the second reaction was lower ($k = 0.0095\ min^{-1}$). That is caused by blocking of the photoactive places of the catalyst by reduced metal copper.

Oxidation of 2,6-DCIP

The photocatalytic activity of the TiO_2 films prepared by sol-gel process from TIP and TTB and also layers prepared by dip and spin-coating from TiO_2 suspension were evaluated by oxidation of 2,6-dichloroindophenol (2,6-DCIP) under UV irradiation. Photodecomposition reactions were performed in a beaker with stirring during the reaction to maintain uniform concentration and temperature.

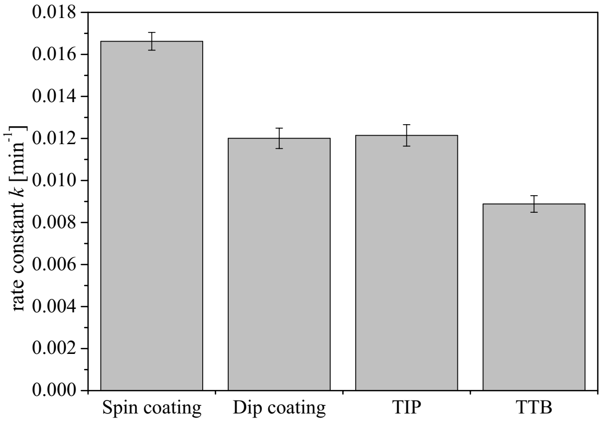

Fig. 3. **The first order rate constants of the photocatalytic 2,6-DCIP decomposition on immobilized TiO2 catalyst**

The Fig. 3. shows the formal first order rate constants of the photocatalytic 2,6-DCIP decomposition. We can see, that the highest rate constant was on the catalyst prepared from TiO_2 suspension by spin coating method. In the case of catalyst films prepared from suspension by dip-coating method and from TIP by sol-gel method, the rate constants were the same. The slowest reaction rate was observed on film prepared from TTB by sol-gel method.

On the other side, films prepared by sol-gel method were completely transparent and shows much better resistance to mechanical damage. The films covered by TiO_2 suspension were opaque and showed very small wear-resistant.

Conclusion

For the photocatalytic reduction processes we have found that when paper is used as carrier for TiO_2 catalyst, the reaction rates are the highest. The preparation of the catalyst layer is very easy and cheap and that is why it could be use in some practical applications as a replaceable cartridge for the photochemical reactor.

For the photocatalytic oxidation processes, we have found, that the films immobilized on glass plate by sol-gel process were less photoactive than the other films on glass, but the higher durability of the sol-gel layers is giving the main advantage for use in practical applications.

REFERENCES

1. Oppenländer T.: Photochemical purification of water and air; WILEY-VCH Verlag, 2003.
2. Zita J., Veselý M., Chovancová J., Možíšková P.: Chemické listy, *98*, 527 (2004).

Table I
The formal first order rate constants of the photocatalytic reduction of Cu^{2+} ions on different forms of immobilised TiO_2 catalyst

Form of TiO_2 catalyst	Initial concentration of Cu^{2+} C_{start} [mg dm^{-3}]	Final concentration of Cu^{2+} C_{final} [mg dm^{-3}]	First order rate constant *k* [min^{-1}]	Standard deviation [min^{-1}]
PVA+suspension	48.88	25.36	0.0049	0.0002
PVA+coated film	51.38	21.38	0.0072	0.0004
PVA+spreading	51.60	31.92	0.0129	0.0002
Paper I. reaction	49.70	0.38	0.0159	0.0005
Paper II. reaction	51.48	3.88	0.0095	0.0009

L04 PHOTOELECTROCHEMICAL PROPERTIES OF TiO_2 LAYERS

JOSEF KRÝSA[a] and GEORG WALDNER[b]
[a]*Institute of Chemical Technology, Department of Inorganic Technology, Technická 5, 166 28 Prague 6, Czech Republic*
[b]*ARC Seibersdorf GmbH, Materials Research, A-2444 Seibersdorf, Austria*

Introduction

Recombination of photogenerated positive holes and electrons inside semiconductor particles is generally responsible for a relatively low quantum yield of the photocatalytic degradation. A possible way to increase the electron-hole separation and consequently to enhance quantum yield is the application of a potential bias. Therefore the aim of the paper is the comparison of photoelectrochemical properties of various TiO_2 layers, namely particulate, sol-gel and thermally produced layers.

Experimental

Production of TiO_2 electrodes

A procedure similar to Vinodgopal *et al.*[1] was used for producing the particulate layers: a P25 slurry (10 g l^{-1}) was spread over the SnO_2-coated glass substrate, and after a settling time of one hour the remaining solution was decanted; the electrode was then dried at 300 °C for one hour. By this fixing procedure the properties of TiO_2 P25 (Degussa) are thus preserved, in particular the temperature is sufficiently low as to prevent sintering of the particles with its associated decrease in active surface area.

A simplified procedure for the preparation of sol-gel layers was used: the precursor solvent (isopropanol) was replaced with ethanol by rotary evaporation and successive addition of ethanol to maintain the initial concentration of 75 % (v/v). For this series of layers the full concentration of 2 M was used. The substrates were pretreated by washing with acetone and Millipore® water. A spin-coater (Specialty Coating Systems, SCS P6708 D) was used for coating of substrates at a rotation speed of 2000 rpm. 100 µl aliquots of the solution were applied onto the spinning substrate, the hydrolysis took place in the film under ambient conditions (purging of equipment by synthetic air, 30 % rh, 22 °C). Finally, the coated samples were heated for one hour at 550 °C under atmospheric conditions.

Titanium metal was thermally oxidized in air at 725 °C to form a homogeneous, compact rutile TiO_2 layer.

Polarization curves

Photoelectrochemical measurements were performed using a three-compartment electrochemical cell with a Pyrex window; the volume of solution was 15 ml. The experiments were done in a 3-electrode set-up consisting ofthe TiO_2 working electrode, a titanium metal wire or platinum mesh acting as counter electrode and a Ag/AgCl reference electrode (3 M KCl, saturated with AgCl). Therefore all potentials mentioned in this paper are referred to this reference electrode with a potential of 216 mV vs. NHE. Polarization curves on irradiated TiO_2 layers were measured in various electrolytes, namely sodium hydroxide, sulphuric acid and oxalic acid.

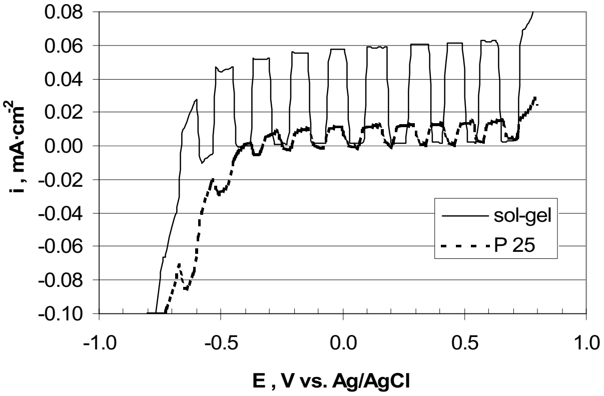

Fig. 1. **Polarization curves in 0.1 M NaOH**

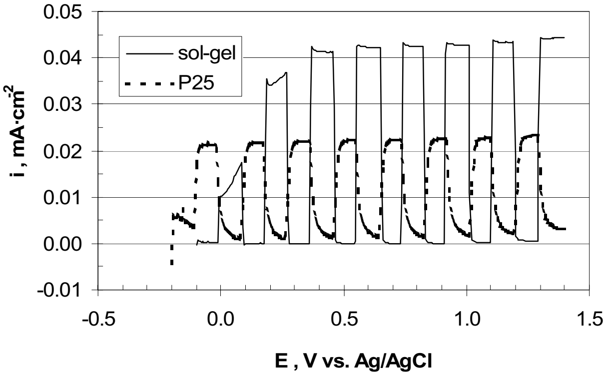

Fig. 2. **Polarization curves in 0.1 M H_2SO_4**

Results

Photocurrents measured in 0.1 M NaOH are very small but those in H_2SO_4 are about five times higher. Photocurrents for sol-gel TiO_2 layers in 0.1 M NaOH are about five times higher than that for Degussa P25 TiO_2 layers and increase with number of layers. The same holds for Na_2SO_4, but in H_2SO_4 the difference between P25 and sol-gel diminishes, however the sol-gel layers still show the higher currents. In solutions of oxidizable substrates the trend is inversed: P25 layers show higher currents, with a steep increase with concentration of solute. In 0.01 M $(COOH)_2$ the photocurrent at Degussa P25 TiO_2 layers is about 2.5 times higher than at the TiO_2 layer prepared by sol-gel. Photocurents for P25 particulate layers in the presence of $(COOH)_2$ are about an order higher than in 0.1 M H_2SO_4. The increase of the measured photo-current in the presence of oxalic acid is due to its strong adsorption and reaction with photogenerated holes.

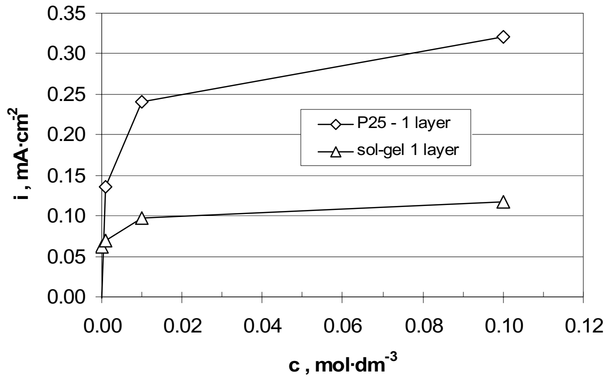

Fig. 3. **Photocurrent at 0.6 V as a function of $(COOH)_2$ concentration**

For comparing different layers and experiments at different lamp intensities, the IPCE (incident-photon-to-current conversion efficiency) is used[2].

Photocurent for thermal TiO_2 layers increases with time of annealing. This means that photocurrent increases with increase of layer thickness. Photocurrents have similar value as for sol-gel layers and about one order than particulate P25 layers. The main reason is higher electric resistivity of whole layer due to the presence of small particles and necessity of photogenerated electrons to cross many particle boundaries before reaching the back contact of electrode.

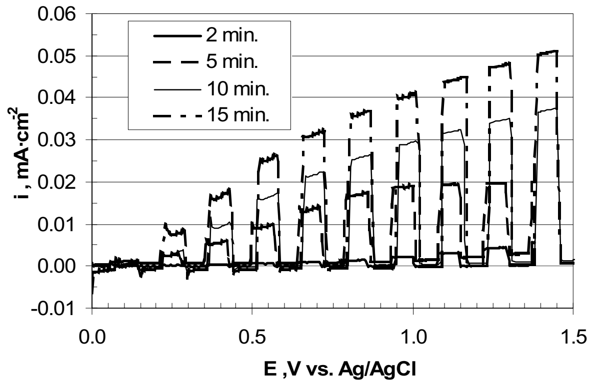

Fig. 4. **Polarization curves for thermal TiO_2 layers in 0.25 M H_2SO_4**

As shown in Table I the effect of applied potential on degradation efficiency depends strongly on the type of TiO_2 film. Photodegradation at open circuit is for particulate TiO_2 film about 3 times higher than that for sol-gel film and 2.5 times higher than for thermal TiO_2 film. Applying potential 0.6 V (SCE) on particulate film results in an only small increase about 12 % (in relation to open circuit degradation rate) while in the case of sol gel film the increase is much higher (about 400 %). It means that for bias application sol-gel layer is more appropriate and particulate layers are convenient only systems where application of bias is not possible.

The economic viability of applying bias for degradation processes is discussed in terms of lamp and bias power consumption. We concluded that only UV lamp's energy demand is relevant and bias power is a negligible cost factor.

Table I
Degradation efficiecy for 0.5 mM 4-CP degradation, irradiation at 365 nm, area = 1 cm^2, 0.1 M Na_2SO_4

E (Ag/AgCl) [V]	Photon flux [mol cm^{-2} s^{-1}]	Degr. flux [mol cm^{-2} s^{-1}]	J_{org}/J_{hv}	Increase with bias [%]
P 25, 1 layer				
Eoc = –0.1	1.385.10^{-8}	5.35.10^{-11}	*3.89.10^{-3}*	
0.6	1.366.10^{-8}	5.96.10^{-11}	*4.36.10^{-3}*	*12.1*
sol-gel 1 layer				
Eoc = –0.24	9.01.10^{-9}	1.07.10^{-11}	*1.18.10^{-3}*	
0.6	9.01.10^{-9}	5.36.10^{-11}	*5.95.10^{-3}*	*402.8*
Ti, 725 °C, 15 min				
Eoc = –0.2	1.20.10^{-8}	1.67.10^{-11}	*1.39.10^{-3}*	
0.6	1.13.10^{-8}	2.78.10^{-11}	*2.46.10^{-3}*	*76.6*

This research was supported by the Ministry of Education, Youth and Sports of the Czech Republic (project number 1M4531477201).

REFERENCES

1. Vinodgopal K., Hotchandani S., Kamat P. V.: J. Phys. Chem. *97*, 9040 (1993).
2. Finklea H. O.: Studies in Physical and Theoretical Chemistry, *53*, 43 (1988).

L05 TRIPLET ENERGY TRANSFER IN BICHROMOPHORIC AMINO ACIDS, DIPEPTIDES AND CARBOXYLIC ACID DIESTER

MIROSLAV ZABADAL[a], DOMINIK HEGER[a],
PETR KLÁN[a] and ZDENĚK KŘÍŽ[b]
[a]*Department of Organic Chemistry, Faculty of Science, Masaryk University, Kotlářská 2, 611 37 Brno, Czech Republic; zabadal@fch.vubr.cz,* [b]*National Centre for Biomolecular Research, Masaryk University, Kotlářská 2, 611 37 Brno, Czech Republic*

Intramolecular triplet-triplet energy transfer (ITET) has been extensively studied in view of structural and geometric effects of spacer between chromophores. Previous studies was focused on the ITET rate constants (k_{ITET}) in various flexible bichromophores with polymethylene chain D-$(CH_2)_n$-O-A (D = donor, A = acceptor) or polyoxymethylene chain and presented the decrease of k_{ITET} only one order of magnitude as the n increased from 5 to 15 (ref.[1,2]).

The ITET in various bichromophoric amino acids (glycine, valine, phenylalanine, and sarcosine), dipeptides (diglycine, diphenylalanine), and a simple diester, with the benzoyl and naphthyl terminal groups serving as donor and acceptor, respectively (Fig. 1.), were studied by the steady-state photokinetic measurements[3].

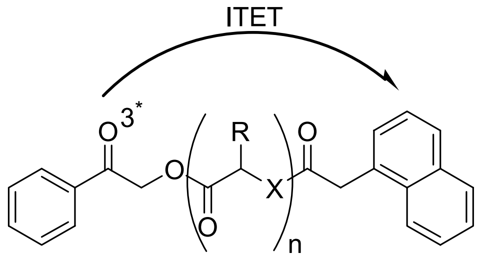

Fig. 1. **The ITET process in investigated bichromophoric amino acids, dipeptides X = NH (R = H, n = 1, 2; R = $CH(CH_3)_2$, n = 1; R = CH_2Ph, n = 1, 2), X = N-CH_3 (R = H, n = 1) and diester (X = O, R = H, n = 1)**

The efficiency of a through-space exothermic ITET was affected by the interchromophore distance (8 or 11 atoms), the nature of the connecting chain as well as the side chains. Rigidity of the peptide bond in short bichromophoric compounds causes that the ITET processes are controlled by ground-state conformational distribution[3,4]. Whereas a less rigid diester would allow that certain unfavorable conformations may coil to favorable ones within an excited-state lifetime ($<10^{-8}$ s). Flexibility of the bichromophore with ester moiety and the steric effect of the side hydrocarbon groups in valine- and sarcosine-based molecules lead into the most efficient energy transfer. While the benzyl groups in the phenylalanine and phenylalanylphenylalanine-based bichromophores had a suppressing effect on ITET.

The conventional steady-state kinetic methods were supported by computer modeling and simulation (a conformational search of the potential energy surface and molecular dynamics simulations) and some other physical analysis (NMR and X-ray)[3,4].

REFERENCES

1. Klán P., Wagner P.: J. Am. Chem. Soc. *120*, 2198 (1998).
2. Wagner P., Klán P.: J. Am. Chem. Soc. *121*, 9626 (1999).
3. Zabadal M., Heger D., Klán P., Kříž Z.: Collect. Czech. Chem. Commun. *69*, 776 (2004).
4. Zabadal M., Heger D., Nečas M., Klán P.: Acta Cryst. C *59*, 77 (2003).

L06 THEORETICAL QSAR STUDY OF POLYNITRO DERIVATIVES OF TOLUENE

KAREL BEDNAŘÍK and ZDENĚK FRIEDL
Brno University of Technology, Faculty of Chemistry, Institute of Chemistry and Technology of Environmental Protection, Purkyňova 118, 612 00 Brno, Czech Republic,
bednarik@fch.vutbr.cz, friedl@fch.vutbr.cz

Introduction

The toxicity of polynitroaromatic compounds was extensively studied and all of them were classified as highly persistent pollutants[1–3]. 2,4,6-Trinitrotoluene (TNT) was investigated most extensively, nevertheless, for other isomeric trinitrotoluenes (2,4,5-, 2,3,4- and 2,3,6-TNT's), dinitrotoluenes (DNT) and nitrotoluenes (NT) the toxicity data are scare.

The toxicities of TNT's and products of their biodegradation, as aminodinitrotoluenes (ADNT) and diaminonitrotoluenes (DANT), were investigated previously[4]. Also toxicity of the nitrotoluenes (NT), nitroanilines (NA), dinitrotoluenes (DNT) and dinitroanilines (DNA) was tested. The toxicity values obtained for altogether 54 nitro aromatic compounds (expressed as an effective concentration EC_{50} in mg l^{-1}) were processed on QSAR level and the dependence of $-\log EC_{50} = f\,(\mathrm{I}, \log P, \mu)$ was obtained. The term I reflects the number and mutual position of the nitro groups[5,6] and remaining variables log *P* and μ are standard QSAR descriptors[7].

This paper deals with theoretical interpretation of QSAR term I by means of *ab initio* DFT B3LYP/6-311+G(d,p) calculations of electron densities at nitro groups and benzene ring of polynitro derivatives of toluene.

Experimental

Toxicity testing on the bioluminescence bacteria *Vibrio Fischeri* NRRL B-11177 using luminometer ToxAlert®10 (MERCK) was described previously[4] and relevant effective concentrations EC_{50} (collecting time 30 min) of polynitro derivatives of toluene[4] are given in Table I. The log *P* values were calculated using ACD/log *P* software[8]. The electrostatic charges at the most positive NO_2 group and benzene ring were derived from the electrostatic potential of equilibrium geometries of all compounds studied. Calculations were performed at *ab initio* level by means of DFT B3LYP/6-311+G(d,p) method[9]. The calculated charges are given in Table I. The QSAR analysis of experimental and theoretical data was processed by Statgraphics software[10].

Results and discussion

In the QSAR analysis a sum of Hammett constants Σσ is mostly used for description of electronic effects and partition coefficients log P_{ow} characterize the lipophilic interactions[7]. The same approach was used in the study of acute toxicity of altogether 54 aromatic nitroderivatives[4] when the term Σσ was substituted by variable I which better characterizes the number and mutual position of nitro groups. Nevertheless, the more exact explanation of substrate-receptor interaction is desirable. For that purpose we have tried to explain the standard QSAR descriptors by means of theoretical electronic charge distribution.

The electrostatic potential map (EPM) gives the electrostatic potential at location on a particular surface, most commonly a surface of electron density corresponding to overall molecular size. The electron density isosurface than corresponds to a van der Waals surface[11]. Considering the substrate-receptor bulky interactions the EPM seems to be a good approximation especially when the alternative localized Mulliken and natural bond orbital (NBO) population analysis gives considerably worse fits.

Table I
Effective concentrations EC_{50} and 6–311+G(d,p) electrostatic charges (in electrons)

Compound	$-\log EC_{50}$	$q(NO_2)$[a]	q(ring)[b]
2-NT	–1.63	–0.1160	–0.4502
3-NT	–1.86	–0.1351	–0.4805
4-NT	–1.66	–0.1208	–0.4824
2,3-DNT	–1.23	0.0169	–0.4009
2,4-DNT	–1.96	–0.0889	–0.3799
2,5-DNT	–0.78	–0.0719	–0.3849
2,6-DNT	–1.57	–0.0885	–0.3602
3,4-DNT	–1.38	–0.0381	–0.4049
3,5-DNT	–1.83	–0.1261	–0.3498
2,3,4-TNT	0.43	0.0379	–0.3408
2,3,5-TNT	0.62	0.0361	–0.3329
2,3,6-TNT	0.85	0.0293	–0.3243
2,4,5-TNT	0.82	–0.0154	–0.3145
2,4,6-TNT	–0.61	–0.0557	–0.2860
3,4,5-TNT	0.66	0.0467	–0.3619

[a] Total charge of the most positive NO_2 group in molecule
[b] Total charge of the benzene ring

In this study the electrostatic charges at individual atoms were derived from the electrostatic potential which was calculated by DFT B3LYP/6-311+G(d,p) method. The total charge of the most positive nitro group (sum of charges at N and both O atoms) in molecule $\boldsymbol{q}(\mathbf{NO_2})$ was considered as a measure of $\Sigma\sigma$ or I electronic QSAR parameters. On the other hand the total charge of the benzene ring (sum of charges of six carbon atoms) ***q*(ring)** should simulate the lipophilic interaction expressed as log P values. The attempt to correlate the total charges of methyl groups $q(CH_3)$ failed ($r = 0.490$) so CH_3 group in polynitro derivatives of toluene serves as a constant steric factor.

The previous QSAR analysis[12] of EC_{50} values with standard parameters **I** and **log *P*** gave Eqs. 1 and 2:

$$-\log EC_{50} = 0.556(0.050)\,\mathbf{I} - 2.280(0.166) \qquad (1)$$
$$(n = 15,\ r = 0.951,\ s = 0.355)$$

$$-\log EC_{50} = -2.597(0.763)\,\mathbf{log}\,\boldsymbol{P} + 4.586(1.580) \qquad (2)$$
$$(n = 15,\ r = -0.686,\ s = 0.833)$$

The theoretically calculated $\boldsymbol{q}(\mathbf{NO_2})$ and ***q*(ring)** charges correlate with previously used QSAR descriptors **I** and **log *P*** according Eqs. 3 and 4. The relationship given by Eq. 3 shows satisfactory correlation between **I** and $\boldsymbol{q}(\mathbf{NO_2})$ electronic parameters and demonstrates in this way a similar nature of both terms:

$$\mathbf{I} = 26.422(2.827)\,\boldsymbol{q}(\mathbf{NO_2}) + 3.981(0.224) \qquad (3)$$
$$(n = 15,\ r = 0.933,\ s = 0.705)$$

$$\mathbf{log}\,\boldsymbol{P} = -4.272(0.709)\,\boldsymbol{q}(\mathbf{ring}) + 0.441(0.270) \qquad (4)$$
$$(n = 15,\ r = -0.858,\ s = 0.156)$$

Still satisfactory relationship between **log *P*** and ***q*(ring)** can be explained in terms of weak molecular interactions. The charges ***q*(ring)** represents mainly π-electron density of the aromatic toluene ring which corresponds with van der Waals forces and, to a certain extent, with hydrophopbic interactions.

From this perspective the Eqs. 1 and 2 can be rewritten by theoretically calculated $\boldsymbol{q}(\mathbf{NO_2})$ and ***q*(ring)** electronic parameters to Eqs. 5 and 6:

$$-\log EC_{50} = 14.083(2.415)\,\boldsymbol{q}(\mathbf{NO_2}) - 0.095(0.191) \qquad (5)$$
$$(n = 15,\ r = 0.851,\ s = 0.602)$$

$$-\log EC_{50} = 12.158(3.992)\,\boldsymbol{q}(\mathbf{ring}) + 3.841(1.522) \qquad (6)$$
$$(n = 15,\ r = 0.645,\ s = 0.875)$$

Conclusions

It has been shown that standard QSAR parameters as $\Sigma\sigma$, I and log *P*, respectively, can successfully be substituted by the theoretical charge distribution derived from an electrostatic potential at *ab initio* DFT level. In the series of polynitro derivatives of toluene the total charge on the most positive nitro group $\boldsymbol{q}(\mathbf{NO_2})$ is a decisive descriptor in theoretically modified QSAR analysis.

REFERENCES

1. Yinon J.: *Toxicity and Metabolism of Explosives,* pp. 3–21. CRC Press, Boca Raton 1990.
2. Palmer W. G., Small M. J., Dacre J. C., Eaton J. C., in: *Organic Energetic Compounds* (Marinkas P. L., ed.),pp. 289–372. Nova Science Publishers, New York 1996.
3. Picka K., Friedl Z.: Fresenius Environ. Bull. *13*, 789 (2004).
4. Bednařík K., Friedl Z.: Fressenius Environ. Bull. (2005), in press.
5. Lang P. Z., Ma X. F., Lu G. H., Wang Y., Bian Y.: Chemosphere *32*, 1547 (1996).

6. Hall H. L., Maynard L. E., Kier B. L.: Environ. Toxicol. Chem. *8*, 783 (1989).
7. Hansch C., Leo A.: *Exploring QSAR*. ACS, Washington 1995.
8. ACD/log *P* DB v.7.0. Advanced Chemistry Development, Toronto 2003.
9. TITAN v.1.0.8. Wavefunction, Schrödinger, Irvine 2001.
10. STATGRAPHICS 6 Pro. Manugistics, Rockville 2000.
11. Hehre W. J.: *A Guide to molecular Mechanics and Quantum Chemical Calculations,* pp. 72–80. Wavenfuction, Irvine 2003.
12. Bednařík K.: *Dissertation.* Brno University of Technology, Brno 2004.

L07 INFUENCE OF ACCELERATED AGEING ON MECHANICAL PROPERTIES OF DIFFERENT TYPES OF PAPERS

MIRIAM TURANOVÁ, BOHUSLAVA HAVLÍNOVÁ
and VLASTA BREZOVÁ,
Department of Graphic Arts Technology and Applied Photochemistry, Radlinského 9, 812 37, Bratislava, Slovak Republic, miria.turanova@stuba.sk

Introduction

In the evaluation of paper materials stability is durability the significant factor, which represents paper's mechanical properties preservation, stored despite of usage and external environment influence[1]. Mechanical parameters, like folding endurance, tensile strength and zero breaking length are monitored. The papers recommended for long-term storage should be stable and durable[7]. The process of paper ageing upon long-term storage is determined by different factors that can be divide in internal (glues, filling materials, additives, presence of acid groups, etc.) and external (storage conditions, temperature, relative humidity of air, light, pollution). Higher loss of mechanical properties occurs in case of higher acidity and copper number. The best evidence for thermal ageing sensitivity and paper's flexibility preservation during long-term storage is folding endurance examination[3,4].

The real process of paper ageing is very slow, consequently in this case it should be very difficult to obtain accurate and exact results in real time. For valuation of paper degradation is necessary to simulate conditions using methods of accelerated ageing. The accelerated ageing techniques represent simulations of conditions, which provide changes in paper properties faster than in reality. The important factor is relationship between degradation of papers by these artificial methods and deterioration of papers in reality. It is difficult to simulate conditions in limited time, to achieve the same changes as in exactly defined time[2,5].

This work is oriented on the investigations of changes in mechanical properties (breaking stress, tensibility, folding endurance, breaking index and zero span) of four different paper samples during accelerated ageing using dry air at temperatures 105 °C and 120 °C, moist heat ageing at temperature 80 °C and relative humidity 25 %, 45 % and 65 %. The results obtained during simulated accelerated ageing can predict changes in paper properties relative to hundreds years of documents storage in archives[6].

Experimental

Materials and methods

Four different types of paper were used wood-free **(A)** woody **(B, D)**, partly woody with different pH value **(C)**:

A classic, wood-free, alkaline, offset paper, grammage 80 g m^{-2}, pH = 9.6, supplied by Bratislava paper company, Slovakia;

B voluminous, classic, print paper, woody, slightly polished, unsized paper, paper pulp content 65 % and 35 % unbleached sulphite pulp, with grammage 50 g m^{-2}, pH = 5.9, made in South-Czech papermills, Větrní, Czech Republic;

C writing, partly woody, acid paper, grammage 80 g m^{-2}, pH = 4.4, made in Slavošovce papermills, Slavošovce, Slovak Republic;

D soft, woody, print paper, machine-glazed, sized paper with paper pulp content 54% and 18% unbleached sulphite pulp and sulphate pulp, with 15% kaolin, grammage 60 g m^{-2}, pH = 6.2, made in South-Czech papermills, Větrní, Czech Republic.

Before measuring of mechanical properties papers were conditioned according to standard STN ISO 187, at temperature 23 °C and relative humidity 50% during 24 hours. The paper properties were determined according to instructions described in STN and STN ISO standards. The experiments were performed using following devices:

- thickness meter, Lorentzen & Wettre, Sweden;
- universal instrument for mechanical tests INSTRON 1011 England;
- device for measuring of folding endurance according to Shopper.

The average value of breaking stress, tensibility, breaking index and zero-span was calculated from 10 measurements and folding endurance from 20 measurements. Papers samples A, B, C and D were exposed to dry air effect (105 °C and 120 °C) according to standard ISO 5630-1 in laboratory chamber WSU 100 (VEB MLW Laboratortechnik, Illmenau) for 0, 8, 24, 72, 168, 336 and 672 hours. We supposed that changes caused using 3 days of accelerated ageing at 105 °C are identical with 25 years of naturally ageing[8].

Samples **A, B, C** and **D** were exposed to the moist heat ageing at 80 °C and 65 % relative humidity in conditioning chamber Feutron GmBH Greis, Germany for 0, 8, 24, 72, 168, 336 and 672 hours using 45 % and 25 % relative humidity in conditioning chamber Challenge 160, 9286 Angelantoni Industrie, Italy.

Results and discussion

Fig. 1a shows decrease of folding endurance of paper **A** after application of dry air and moist heat ageing. Folding endurance expressed by number of double folds, measured using standard foldings in machine directions. The experimental data observed, which describe folding endurance decline during ageing, are exponentially dependent on the ageing time. The time changes in folding endurance can be mathematically described with formal first-order kinetic model. In accord with these assumption, experimental values showed in Fig. 1., and also other experimental changes observed during paper ageing, were fitted by general exponential equation, $y = P1 . \exp(-k . t) + P2$, using least square analysis (program Scientist MicroMath), where y is observed paper attribute and t is time of accelerated ageing influence on paper.. The parameters P1, P2 and formal first-order constant, k, were calculated.

The results evaluated for papers **B** and **C** are depicted in Fig. 1b. We obtained very good agreements of calculated and experimental values for these three papers, which were confirmed with high values of correlation statistical parameters. The application of first-order kinetic parameters (P1, P2, k) allows us to calculate values of folding endurance in optional time of artificial ageing. Fig. 1d shows decrease of folding endurance for paper **D**, where we have to use combined kinetic model of first- and second-order

$$y = 1/(P1 + k_1 . t) + P2 . \exp(-k_2 . t) + P3.$$

The application of combined kinetic model enables us to obtain good agreement of experimental and calculated values. The failure of simple first-order kinetic model in the monitoring of changes in folding endurance in time observed

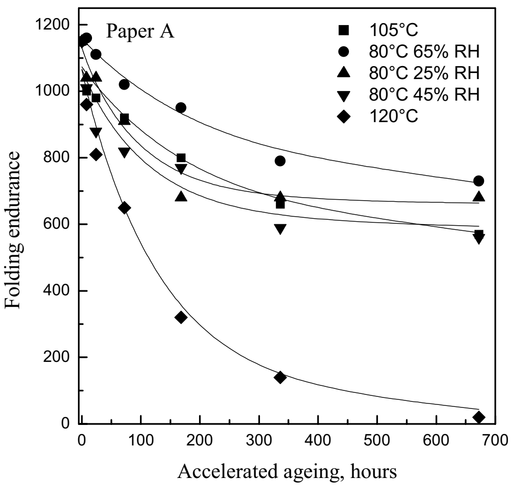

Figure 1a

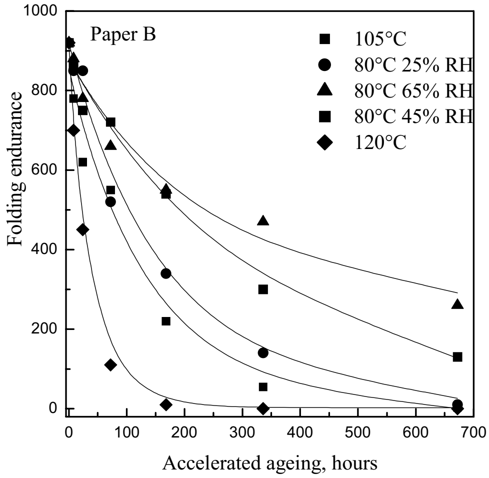

Figure 1b

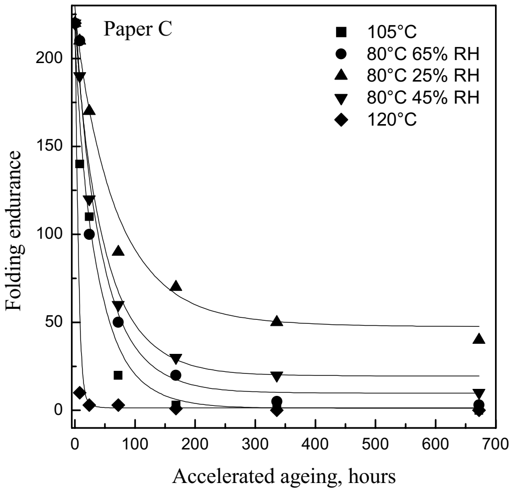

Figure 1c

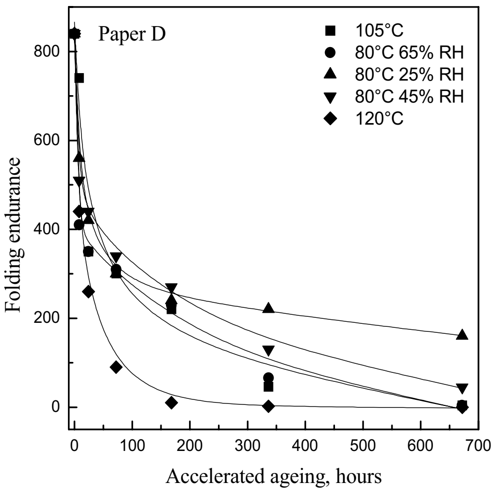

Figure 1d

Fig. 1a−1d **The dependence of folding endurance on time of accelerated ageing after application of 5 types of ageing on 4 types of papers (A−D)**

Table I
Calculated parameters of kinetic models for all types of paper

Paper A	P1	P2	k	$R_{squared}$		
Type of ageing						
120 °C	1025	38	0.008	0.995		
105 °C	518	555	0.005	0.978		
80 °C, 65 % RH	460	698	0.004	0.999		
80 °C, 45 % RH	472	593	0.009	0.995		
80 °C, 25 % RH	466	663	0.011	0.998		
Paper B	P1	P2	k	$R_{squared}$		
Type of ageing						
120 °C	908	2	0.030	0.999		
105 °C	859	–4	0.008	0.992		
80 °C, 65 % RH	904	14	0.006	0.996		
80 °C, 45 % RH	847	33	0.003	0.997		
80 °C, 25 % RH	621	257	0.004	0.996		
Paper C	P1	P2	k	$R_{squared}$		
Type of ageing						
120 °C	218	1.4	0.400	0.999		
105 °C	207	1	0.032	0.990		
80 °C, 65 % RH	219	10	0.028	0.986		
80 °C, 45 % RH	200	20	0.025	0.996		
80 °C, 25 % RH	178	48	0.017	0.997		
Paper D	P1	P2	P3	k1	k2	$R_{squared}$
Type of ageing						
120 °C	0.0019	338	–4.7	0.0005	0.0223	0.999
105 °C	0.0014	316	–145	8.0739	0.0014	0.983
80 °C, 65 % RH	0.0022	449	–54	0.0054	0.0033	0.998
80 °C, 45 % RH	0.0024	442	–8.4	0.0011	0.0033	0.999
80 °C, 25 % RH	0.0016	–231	466	0.0002	–0.0033	0.999

for paper **D** is probably caused by glue sizing of paper, and consequently changes of degradation mechanism. Kinetic parameters (k, P1, P2...) for papers **A, B, C** and **D** for folding endurance are summarized Table I. Our experiments confirmed, that paper A fits the demands for paper durability according to ISO 9706 standard.

Before accelerated ageing reached this paper high folding endurance, but after dry ageing at 120 °C shows significant loss of this value. Paper **B** possessed high initial folding endurance, but after dry air ageing 120 °C, 105 °C and moist heat ageing at 80 °C and 65 % relative humidity decreased to zero. Paper **D** with high initial folding endurance revealed significant lowering for both types of dry air ageing, also for moist heat ageing at 65 % and 45 % relative humidity.

The influence of accelerated ageing on breaking stress, tensibility and breaking index for all papers is not so significant as on folding endurance. The best ageing resistance was observed for paper **A** and the worst for paper **C**. Papers **B** and **D** are not suitable for archive applications.

Distribution and size of pores and capillaries on the paper surface can also contribute to the changes induced by accelerated ageing (papers **B** and **D**). In our set of experimental values paper **A** had reached best results with cold extract pH 9.6 before ageing and 9.5–9.1 after ageing. Alkaline reserve of this paper it was 4.3 mol kg^{-1} and after ageing at 105 °C remained high enough 3.5 mol kg^{-1}. This paper also shows the best resistance to all five types of accelerated ageing. Figs. 2., 3., 4. and 5. shows percentage decrease of breaking stress, tensibility, folding endurance and zero-span for all papers **A, B, C** and **D** after 72 hours and 672 hours of artificial ageing.

Fig. 6. shows percentage decrease of folding endurance at 105 °C after 72 hours and 672 hours for papers **A, B, C** and **D**. We can see that only paper A (characterized with high alkaline reserve) lost after 72 hours 20% and after 672 hours 50%, other three papers had lost 100%.

Conclusions

The resistance of mechanical properties for four paper samples were investigated during five types of accelerated ageing procedures; two types of dry ageing (105 °C and 120 °C) and three types of moist heat ageing (80 °C and 25 % RH, 45 % RH, 65 % RH). Upon accelerated ageing of papers

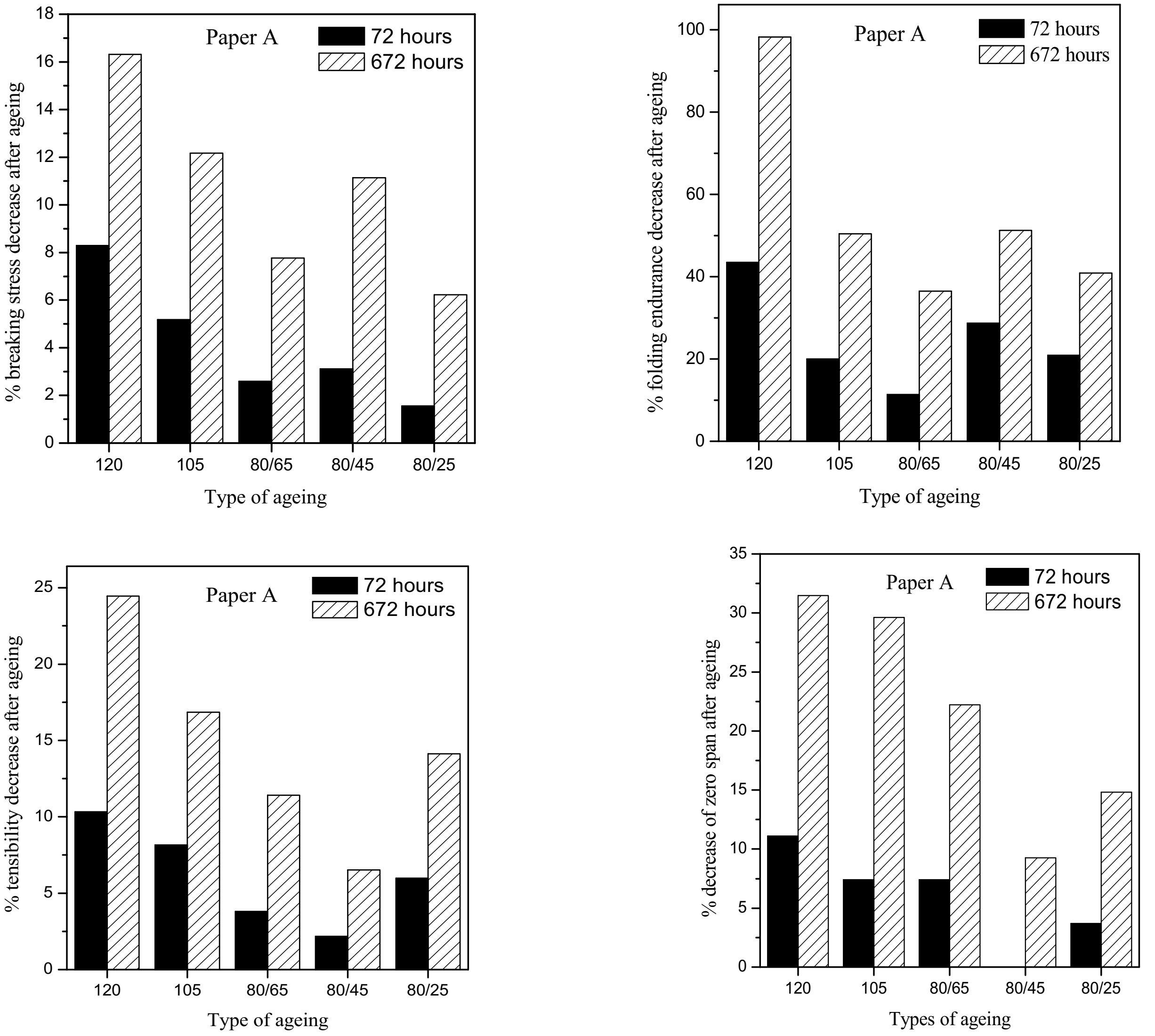

Fig. 2. **Mechanical properties decrease of paper A after application of different types of accelerated ageing**

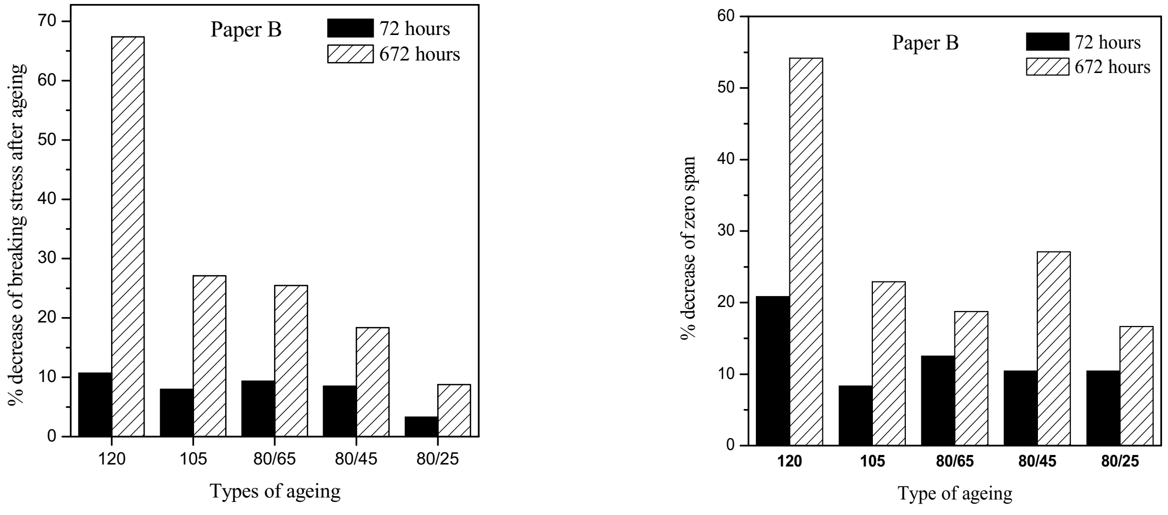

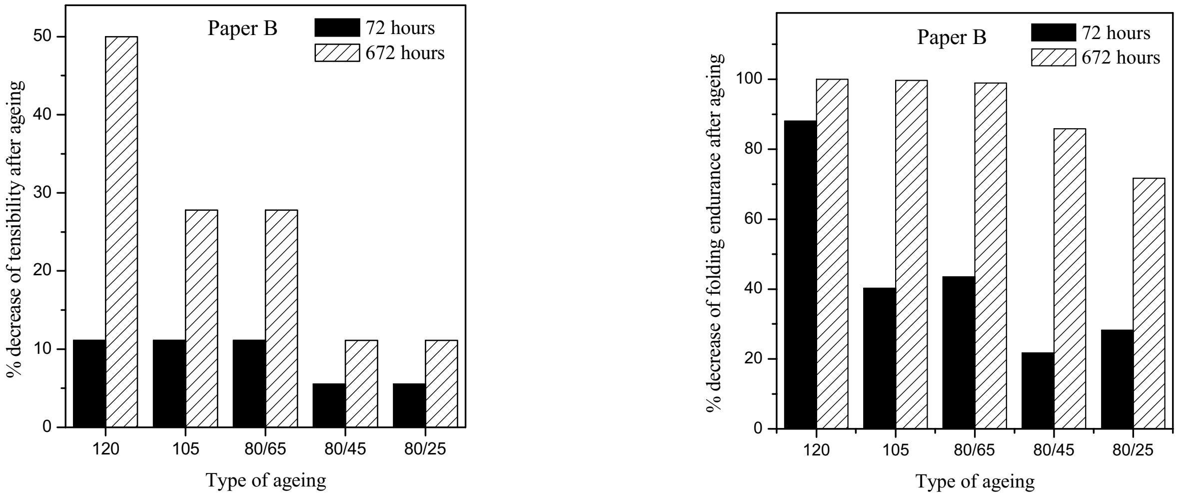

Fig. 3. **Mechanical properties decrease of paper B after application of different types of accelerated ageing**

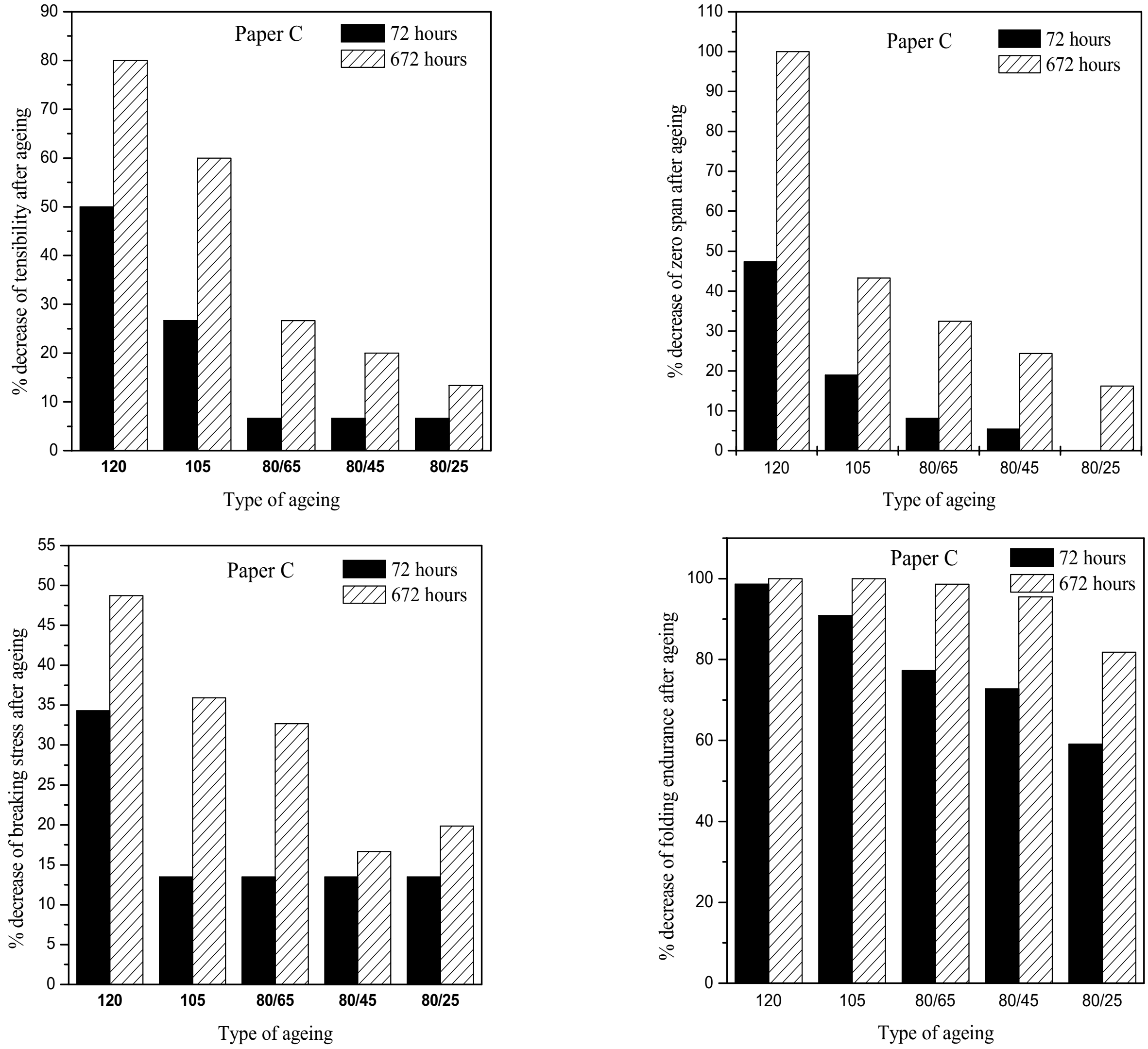

Fig. 4. **Mechanical properties decrease of paper C after application of different types of accelerated ageing**

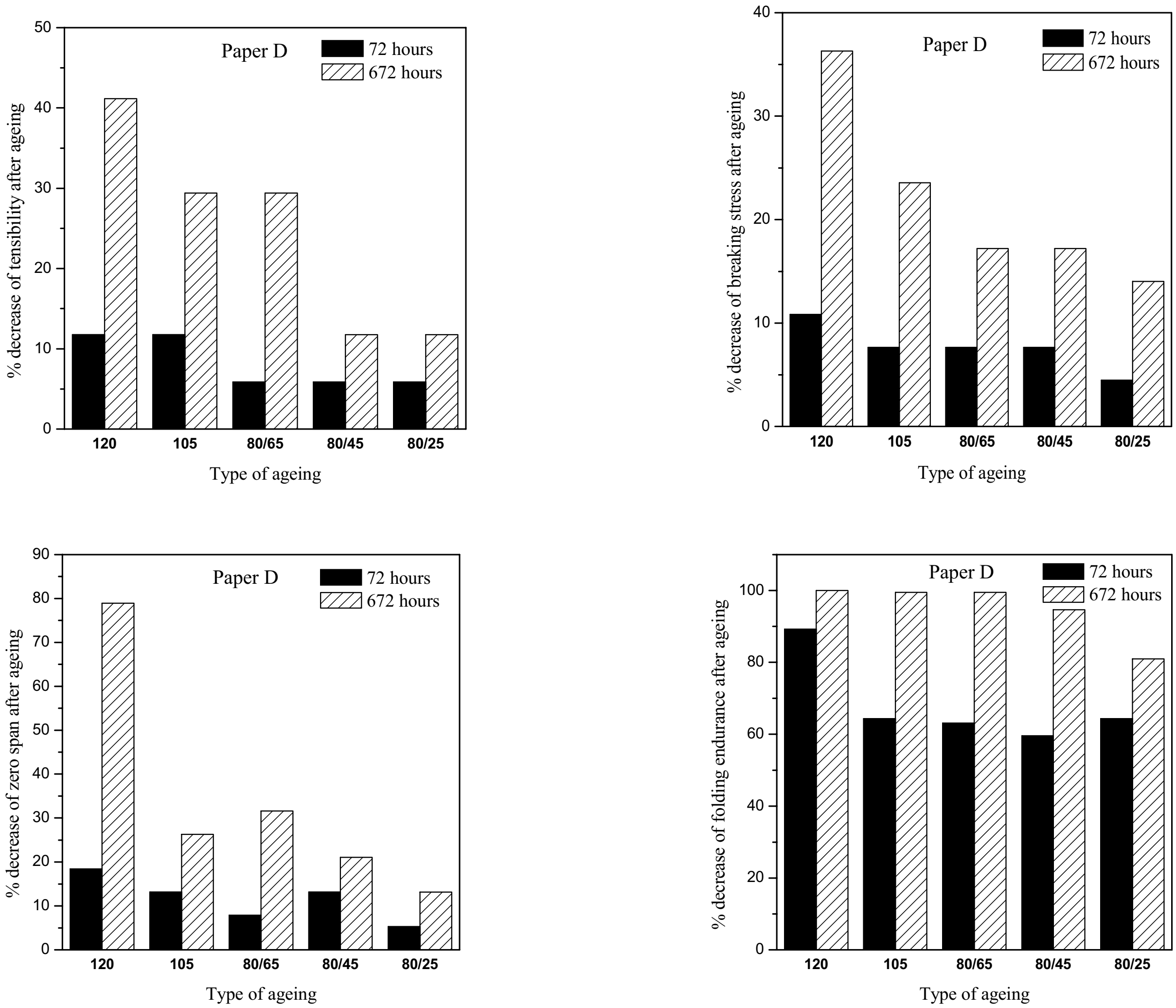

Fig. 5. **Mechanical properties decrease of paper D after application of different types of accelerated ageing**

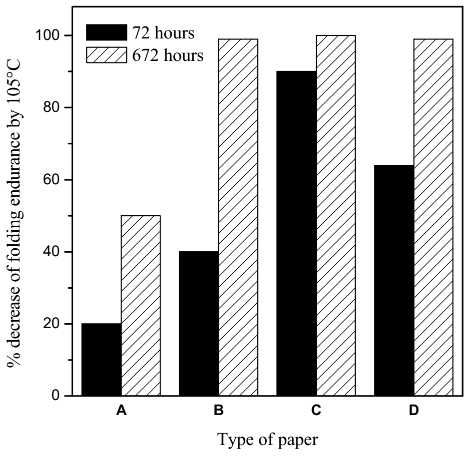

Fig. 6. **Decrease of folding endurance for dry air ageing at 105 °C**

under experimental conditions, the significant decrease of observed properties occurred. This decrease for three papers is possible to describe by the first-order kinetic model, but for paper **D** the application of combined kinetic equation is suitable. Mathematical description of experimental values enabled us to calculate the values of observed properties after required accelerated ageing time. The best durability after accelerated ageing procedures was observed for paper **A,** which is suitable for permanent and archives documents.

We thank Ministry of education of Slovak Republic for the financial support of project KNIHA.Sk, and Technology Assistance Agency (Slovakia) under the contract No. APVT–20–03 4202.

REFERENCES

1. Bredereck K., Siller-Grabenstein A.: Restaurator *9*, 113 (1988).

2. Havermans J. B. G. A.: Restaurator *16*, 209 (1995).
3. Konva A., Krause T.: Papier *36*, 263 (1982).
4. Wedinger R.: Abbey Newslett. *13*, 126 (1989).
5. Bukovsky V.: Restaurator *20*, 77 (1999).
6. Havlínová B., Brezová V., Horňáková L., Mináriková J., Čeppan M.: M. J. Mat. Sci. *37*, 303 (2002).
7. Kolar J., Strlic M., Pihlar B.: Anal.Chim. Acta *43*, 313 (2001).
8. ISO Standard 5630-1 to 4 (50 0375) Paper and cardboard, Accelerated ageing.

L08 BARRIER PROPERTIES OF POLYMER COATINGS BASED ON MODIFIED WATER SOLUBLE POLYMERS

VIERA JANČOVIČOVÁ, IVANA LÖRINCZOVÁ,
IVETA MRLLÁKOVÁ and ZDENKA IŽDINSKÁ
Department of Printing Arts Technology and Applied Photochemistry, Faculty of Chemical and Food Technology SUT, Radlinského 9, 812 37 Bratislava, Slovak Republic, viera.jancovicova@stuba.sk

Introduction

The materials based on cellulose fibres like a paper or a cardboard are widely used in the printing and the packaging industry. They are sensitive to humidity and oxygen, what is unwelcome. Today, the barrier properties of standard packaging materials are commonly achieved by a lamination. An alternative to the lamination can be a modification of the paper fibres or an introduction of the polymer coating for the paper surface processed by suitable technology in order to enhance protective properties of printing or packaging materials.

To protect prints or paper substrates from the influence of the atmosphere humidity and the oxygen it is possible to use the hydrophobic protective coatings. On the other hand, the hydrophilicity of printing media is required in the case of widely used waterbased inks. The possible solution is resulting from the introduction of the coating with the switchable properties, it means it shows both hydrophilic character before the printing process to ensure printability and required final quality of print, and the hydrophobic character induced after printing to improve weather fastness. The methods of this program hydrophobisation after printing are described in several works[1,2] and it can be achieved by the photochemical modification of a coating, the thermal polymerization, the complex formation or by some other methods.

The suitable solution to comply this special requirement can be presented by introduction of the hydrophilic waterbased systems and their realization by UV-curing technology in order to achieve the hydrophobic surface of a print by a simple exposure to the UV-light after the printing. Moreover, the UV-curable waterbased systems[3,4] offers a number of advantages, mainly no VOC emission, low irritability, high speed processing, high gloss and the possibility of a thin layer preparation. The disadvantages are partly offset by the necessity to introduce a drying step before UV-exposure to remove water and produce a cohesive film.

The poly(vinyl alcohol) (PVA) is a water soluble polymer with applications in paper coating, textile sizing and packing. It is the only polyvinyl-type synthetic polymer which has been confirmed to be biodegradable[5]. This feature and its water solubility infer the advantage of easier degradation and elimination after use[6,7]. Due to its biocompatibility, PVA can be used for a variety of biomedical applications, preferably in the form of hydrogel PVA can be used to improve the strength properties and the brightness stability of the treated paper sheets particularly in a mixture with chitosan[8]. The influence of the poly(vinyl alcohol) film applied to the paper surface can be reflected in better barrier properties of the coated paper, such as the lower air permeability, the lower water vapour transmission rate and the better grease resistance.

Before applying of the PVA water solution on the paper surface two approaches to modify the paper surface were used. First, mainly of a physical character, includes the paper calendaring and the second one the corona treatment[9].

The drawback of films based on PVA is its insufficient water resistance. The modification of PVA by different organic compounds such as aldehydes, carboxylic acids or anhydrides can improve barrier properties of PVA coatings, what allows their application in the food packaging industry[6,10]. The furan- and tiophene-based chromophores bearing a terminal aldehyde function were synthesize according Fang[11]. The terminal aldehyde function allows appending the chromophores to PVA and obtained polymer is photocrosslinkable.

The objective of our work was to synthesize two types of unsaturated PVA derivatives and to perform UV-curing of dried waterborne coating applied on the paper sheets in the presence of a radical type photoinitiator. The surface energy of cured coatings was evaluated by measuring the contact angle using different testing liquids (water, glycerol, ethylene glycol, formamide, aniline, benzyl alcohol, bromo naphtalene)[12], the water diffusion by swelling measurement and the water vapour permeability by means of gravimetry. The effect of the acrylic acid (AA) and the polyester acrylate (PE) addition on the barrier properties of coating based on PVA derivatives was investigated.

Experimental part

Materials

Poly(vinyl alcohol) POVAL 205 (Kuraray, Japan) of a degree of hydrolysis of 88 %, poly(vinyl alcohol) Sloviol 10–98 (NCHZ, Slovakia) of a degree of hydrolysis of 98.6%, malein anhydride (Lachema, Czech Republic), 4-dimethylaminopyridine (DMAP) (Fluka, Switzerland), acrylic acid (Merck, Germany), glycidylmethacrylate (Merck, Germany), dimethylformamid (DMF, Lachema, Czech Republic), dimethyl sulfoxide (DMSO, Merck, Germany), Irgacure 2959 (Ciba SC, Switzerland), polyester acrylate Laromer PE 55 WN (BASF, Germany) and Acetone (Merck, Germany) were used.

Preparation of PVA derivatives

In this work two types of modified poly(vinyl alcohol) (PVA) were used, such as poly(vinyl alcohol) modified by malein anhydride and poly(vinyl alcohol) modified by glycidylmethacrylate.

The first type of PVA derivative was prepared by the reaction of the poly(vinyl alcohol) (Sloviol, Poval) with a malein anhydride in a solvent (DMF and water). The mixture was steered at 60 °C for 1, 5 and 10 hours and subsequently the modified poly(vinyl alcohol) was obtained by a precipitation using an acetone treatment. To increase a product yield the catalysator dimethylaminopyridine (DMAP) was added to mixture at the concentration of 1–5 wt % for the malein anhydride content.

The second way to obtain the photocrosslinked polymer was by the reaction of the poly(vinyl alcohol) with a glycidylmethacrylate (GMA) in a solvent mixture (DMF and DMSO). During steering of a mixture at 70 °C a solution of a glycidylmethacrylate in KOH was added. The final product was obtained again by a precipitation using an acetone treatment following by drying of a product at the room temperature. The content of double bonds in prepared PVA derivatives was determined by three different methods, namely titration, UV/VIS spectroscopy and FTIR spectroscopy.

Preparation of samples

The solution of the poly(vinyl alcohol) derivatives (10 wt %) in water was prepared and cast onto aluminium plates (to evaluate a diffusion of the water to the coating) and onto paper sheets (to quantify the water vapour permeability and the surface energy of the coating). Also free films based on PVA derivatives were prepared just allowing the evaluation by infrared spectroscopy. Waterborne layers were dried at ambient temperature until a cohesive clearcoat was obtained. The samples containing the fotoinitiator Irgacure 2959 were cured by a medium pressure mercury lamp at the light intensity 20 mW cm^{-2}.

Measurements

The surface energy of the UV-cured coatings was determined by measuring the contact angle of a drop of different organic solvents by means of a goniometer equipped with a CCD camera. The water diffusion to the UV-cured polymer coatings was investigated through swelling measurements by a Dogatkin device, thus allowing measuring a volume of water absorbed by a coating Q.

The water vapour permeability (WVP) was quantified according to a German norm DIN 53122 and determined as an amount of the water vapour in grams passed through paper coated with UV-curable coating of a certain thickness within 24 hours at the temperature of 20–23 °C and relative humidity of 85 % provided by saturated KCl solution. Water vapour was quantitative absorbed on silicagel.

Results and discussion

The hydroxyl groups of the PVA were esterified by introducing groups with unsaturated fotochemically active bonds. This reaction was carried out from the both PVA (Poval, Sloviol) by the method described in the experimental part. We prepared the derivatives of Sloviol with malein anhydride, but the esterification degree 1.5–3 % was insufficient for further experiments. The derivatives of Poval with malein anhydride without catalyst – PVAMA (estrification degree 11 %), and with catalyst DMAP – PVAMA1 (1 % of DMAP related to PVA weight, esterification degree 16 %), PVAMA3 (3 % of DMAP, e. d. 17 %) and *PVAM5* (5 % of DMAP, e. d. 21 %) were prepared by the same reaction. The product PVAGMA was prepared by the reaction of Poval with glycidyl methacrylate.

So prepared derivatives were fotochemically active and in the presence of the photoinitiator Irgacure 2959 (1 wt. %)

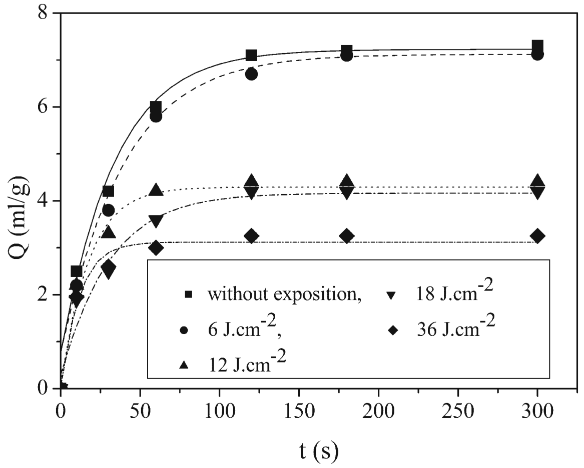

Fig. 1. **Swelling degree as a function of the swelling time for PVAMA1 samples (initiator Irgacure 2959) exposed with various UV-dose (0–36 J cm^{-2})**

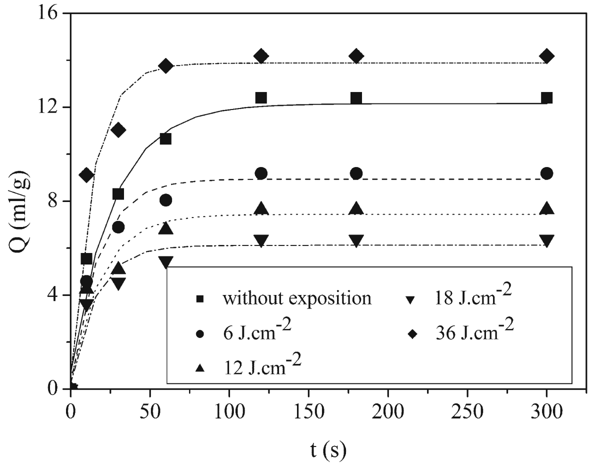

Fig. 2. **Swelling degree as a function of the swelling time for PVAGMA samples (initiator Irgacure 2959) exposed with various UV-dose (0–36 J cm^{-2})**

and UV light occurred the photopolymerisation reaction which improved barrier properties.

The penetration results were characterized by exponential function $Q = Q_{max}(1 - e^{-kt})$. It is evident, that the swelling grade of modified poly (vinyl alcohol) PVAMA1 decreased with the UV-exposure dose (Fig. 1.). The lowest swelling value was achieved by the exposure dose 30 J cm^{-2}, which is against unexposed layer lower about 60 %. The additional extension of exposure increased water diffusion into polymer layer, hence caused the deterioration of barrier properties. The similar results were obtained by PVAGMA, the lowest swelling was achieved by 15 J cm^{-2} then its value increased (Fig. 2.). The addition of polyester acrylate (PE) and acrylic acid (AA) reduced the water penetration into the polymer layer only in the case of modified PVA with a low esterification degree (less then 5 %), PVA derivatives with the esterification degree more than 10 % caused moderate deterioration of barrier properties.

The UV curing of layers could be established with the contact angle measurement. Changes of hydrophilicity were not significant. The contact angle of water slightly increased with the UV light exposure of PVAMA during first 15 minutes till the dose 18 J cm^{-2}. The contact angle of water for PVAGMA during first 10 minutes (exposure dose 12 J cm^{-2}) increased and subsequently began to decrease. The effect of hydrophilization occurred at lower light dose than the increase of water penetration, what is probably related with rather degradation on the layer surface. The influence of PE and AA was similar as by penetration measurements.

The surface energie of unexposed and exposed coatings was calculated and its values are ranging from 47 to 51 mJ m^{-2}, (polar component from 6 to 9 mJ m^{-2} and dispersive component from 41 to 43 mJ m^{-2}). The effect of the UV-curing was not registered.

The water vapour permeability is very important in order to evaluate barrier properties of polymers. The PVA solutions were cast onto paper sheets by a cylinder and air dried. The layer thickness was established gravimetrically. The weight of absorbed water vapour on the silicagel was obtained from the weight differences before experiment and after 24 hours at air humidity of 85 %. The ratio of absorbed water vapour and area of coated paper represents the WVP value.

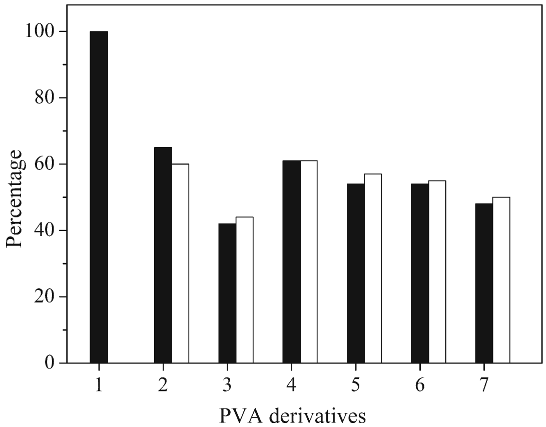

Fig. 3. **The decrease of WVP of paper coated with UV-curable PVA derivatives relative to uncoated paper (black fields) and the decrease of swelling by curing of PVA derivatives (white fields); 1-uncoated paper, 2- PVAMA, 3-PVAMA1, 4-PVAMA5, 5-PVAMA1+PE, 6-PVAMA1+AA, 7-PVAGMA**

The Fig. 3. demonstrates the influence of cured layer of modified poly(vinyl alcohol) on the WVP. Applied polymer layers generally decreased the WVP value of paper, the most important was the effect of the poly(vinyl alcohol) modified with malein anhydride PVAMA1 and with glycidylmethacrylate PVAGMA. The addition of PE or AA to modified PVA slightly deteriorated the barrier properties. The Fig. 3. shows the decrease of swelling values by curing PVA derivatives. The correlation between the decrease of WVP and the water swelling decrease was very good.

Conclusions

The photochemically active polymer films were prepared by addition of the radical-type photoinitiator to synthetized unsaturated derivatives of poly(vinyl alcohol). The changes of barrier properties of coatings during the UV-curing process were observed by surface energy, swelling and water vapour permeability measurement. The optimal UV-exposure leads to lower swelling degree, water vapour permeability and hydrophilicity of layers.

We thank the Slovak Grant Agency VEGA (project VEGA 1/2454/05) for financial support.

REFERENCES

1. Lörinczová I., Jančovičová V., Čeppan M.: Chem. Listy *97*, 265 (2003).
2. Lörinczová I., Jančovičová V., Čeppan M.: Papír a celulóza *1*, 22 (2003).
3. Decker C., Lörinczová I.: Proceedings of RadTech. Europe Conf., Berlin, 3–5 November 2003, Vol. II, p. 699.
4. Decker C., Masson F., Schwalm R.: JCT Research 1, 127 (2004).
5. Alexy P., Bakoš D., Crkoňová G., Kramárová Z., Hoffmann J., Julinová M., Chiellini E., Cinell P.: Polymer Testing *22*, 811 (2003).
6. Giménez V., Reina J. A., Mantecón A., Cádiz V.: Polymer *40*, 2759 (1999).
7. Döppers L. A., Breen C., Sammon C.: Vibrational Spectroscopy *35*, 27 (2004).
8. Kamel S., El-Sakhavy M., Nada A. M. A.: Thermochimica Acta *421*, 81 (2004).
9. Schuman T., Wikström M., Rigdahl M.: Surf. Coat. Techn. *183*, 96 (2004).
10. Moritani K., Kajitani K.: Polymer *38*, 2933 (1997).
11. Fang S. W., Timpe H. J., Gandini A.: Polymer *43*, 3505 (2002).
12. Jakubíková Z., Mikula M., Prosnan B.: Int. conf. Silicon – News in Science and Technology, Podbanské, 2004, Proceedings, p. 50 (Poster).

L09 DEGRADATION AND OPTIMAL TREATMENT OF POLYPROPYLENE BY ATMOSPHERIC DB DISCHARGE

MILAN MIKULA, BRANISLAV PROSNAN
and ZUZANA JAKUBÍKOVÁ
Department of Graphic Arts Technology and Applied Photochemistry, Faculty of Chemical and Food Technology, Slovak University of Technology, Radlinského 9, SK-812 37 Bratislava, milan.mikula@stuba.sk

Abstract

Plasma treatment is a widely accepted technique in printing and packaging industry to improve surface wettability and adhesive characteristics of polymer foils. However, the plasma surface interaction is quite complicated and not completely understood. Discharge improvements are implemented to make the treatment more homogeneous, stable and effective. Simple and reliable methods are required to control the treatment leading to better adhesion and bonding. Several simple experiments indicating optimal treatment are discussed and correlated with surface analysis. The treatment level was characterized besides standard methods by changes of optical density, gloss, zeta potential, UV absorption and pH of a rinse.

Introduction

Common polymer foils used in packaging industry ought to be printed, varnished, glued, laminated, metalized, heat sealed, etc. to increase mechanical, barrier, optical properties and information and esthetical value. Low surface energy of inert non-polar polymers (polypropylene, polyethylene,…) causes their low wettability and adhesion that plays the key role in overall stability and functionality of the composition. So substrate polymer surfaces require activation in order to increase the surface energy and adhesion to the next layer[1].

Various physical/chemical processes are used to activate the polymer surfaces, while plasma based methods are widely accepted in printing and packaging industry to improve surface wettability and adhesive characteristics of polymer foils. Low-pressure plasmas are impractical for industrial application to treat large scale polymer and coated substrates. However, the atmospheric pressure plasma treatment has been successfully tested on various polymer foils, textile and nonwovens, using several discharge types, mostly high frequency, after glow flame and dielectric barrier ones, with a range of reactive gases[2].

The widely used method of industrial foil treatment is an exposure in active zone of AC (50 Hz–100 kHz) dielectric barrier discharge (DBD) in common air atmosphere, (in "corona"). Capacitively coupled discharge burns in an air gap separated from electrodes by dielectric barrier placed on one or both electrodes. Adhesion of treated foils increases due to higher surface roughness, the elimination of weak boundary layers, introduction of polar groups and other chemical changes in the surface region and electret formation[3]. Recommended treatment level of energy density applied on is up to 3 kJ m^{-2} to reach the sufficient surface energy (above 40 mJ m^{-2}). On the other hand overtreatment leads to the surface degradation (particularly in the presence of oxygen), low molecular products creation and adhesion decrease. Also the wetting and adhesion characteristics tend to decay with time after treatment; however, they don't reach the original characteristics of the untreated polymer[3,4].

Higher efficiency and limited ageing of the treatment are possible to achieve with the different atmosphere compositions and more effective discharges. It is important to adjust diffuse regime of standard DBD instead of spark one[5], (better to use two barriers at both electrodes, Fig. 1.).

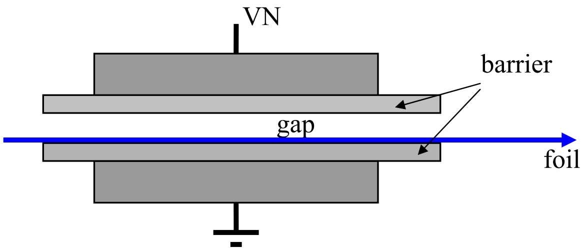

Fig. 1. **Standard DBD arrangement (used gap: 2 mm, glass barrier: 1 mm)**

The new surface DBD treatment buried at a ceramic plate[6] (particularly coplanar) seems to be more effective and more stabile, namely in nitrogen atmosphere. It is very promising solution for flat polymer surfaces because of more effective, homogeneous and diffuse discharge. The advantage of atmospheric discharges is in higher affectivity of free radical, metastables and excimers creation[7,8] and in the ability of high rate and large scale of technological treatment.

Discharge plasma breaks the molecular bonds at a thin surface layer (up to 10 nm) of the substrate. The broken bonds recombine with free radicals from the plasma and from the substrate to form additional functional groups or to perform crosslinking, grafting or polymerization. However, the plasma surface interaction is quite complicated and not completely understood. Generally, it includes surface charging, chemical modification, mechanical etching, material sputtering and/or deposition, etc.

The aim of the work is to find simple tests for optimal treatment determination. Standard methods are based on adhesion tests, contact angle measurements, ATR-IR spectroscopy, scanning electron microscopy SEM, atomic force microscopy AFM for the roughness determination and x-ray photoelectron and secondary ion mass spectroscopy (XPS and SIMS) for chemical analysis of the changes[4]. Rarely zeta potential of treated foils is measured[7,9]. In manufacturing processes involving coating or printing the major interest of the end user is not the science behind, but rather optimal treatment, simple and easy measurable results and better bonding. Several simple experiments indicating optimal treatment are discussed and correlated with surface analysis.

Experimental

The standard volume DBD (Fig. 1.) was used for the treatment of biaxially oriented polypropylene foil (BOPP, 40 µm, not treated at the production line). Air gap, frequency and voltage (2 mm, 5 kHz, 15 kV) were adjusted to keep the most diffuse discharge regime. The treatment was performed at the atmospheric pressure in the air and technical nitrogen (N_2) at various exposure times. The changes of the exposed samples were determined measuring gloss and light scattering by the optical density measurement of treated foils at a black background, zeta potential of foil surfaces in water solution and the, UV absorption and pH of water and methanol solutions rinsed of treated foils, besides the standard methods as SEM and tape test of adhesion.

Gloss of the foils was measured relative to the black glossy standard by red laser light reflection at the angle of 20°.

The treated foil becomes a little matt, so it decreases the optical density of black color under the foil due to the light scattering. The reflection optical density D of the treated foil backgrounded by a black paper was measured by X-Rite densitometer. D = –log(R), where R is remission.

Zeta potential (ζ) of the foil surfaces was measured via streaming potential (U) in water solution of KCl (10^{-4} mol l^{-1}) using the flat sample chamber according the Fig. 2. and determined from Hemoltz – Smoluchowski equation:

$$\zeta = \frac{U}{\Delta p}\cdot\frac{\eta\sigma}{\varepsilon},$$

where Δp is the pressure difference at the measuring channel and η, σ and ε are viscosity, conductivity and permeability of the solution, respectively.

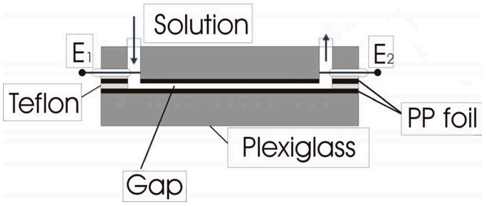

Fig. 2. **The flat chamber (EKA Paar) for streaming potential measurements (gap: 12 mm × 0.3 mm)**

Treated foils were rinsed in water, in methanol and in n-heptane (10 cm^2 of a treated foil in 10 ml of solution, 1 minute). Afterwards pH and UV absorption spectra of the solutions were measured in 3 cm cuvette by Spectrometer PayUnicam 8800.

Results and discussion

Plasma generally changes the surface topography of treated foils. When the foil is overtreated, degradation occurs and low-molecular degradation products created at the foil surface can be found as a weak light scattering or as a lost of gloss. The gloss changes with time of the treatment in air and nitrogen DBD are illustrated in Fig. 3. As expected the treatment in air plasma is much more destructive with higher roughness[1]. A short induction period can be found at the beginning of the treatment just in the case of air.

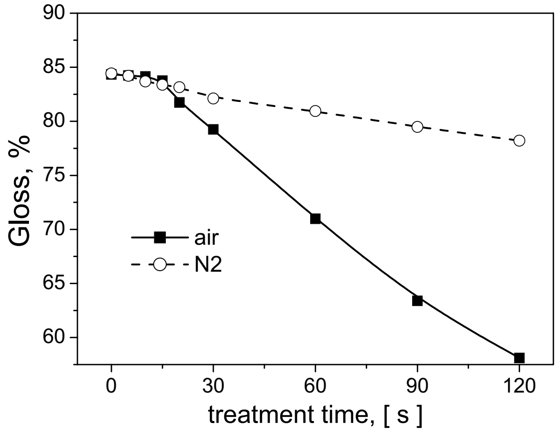

Fig. 3. **The gloss changes of treated foils in air and N_2 DBD plasma**

Similar results gives the measurements of optical density, however, a saturation of light scattering has occurred (Fig. 4.). The weak white haze appears after treatment in air DBD and so the measured mutual optical density of black paper (background) covered by initially transparent treated foils decreases. The reverse density proportional to the light scattering increases as can be seen in Fig. 4. The start position of the slope of "s-curve" (induction period of degradation) can be taken as the optimal exposition: maximal exposition without the creation of remarkable degradation products at the foil surface (~ 12 s). Generally, the amount of degradation products is much less when treated in nitrogen atmosphere

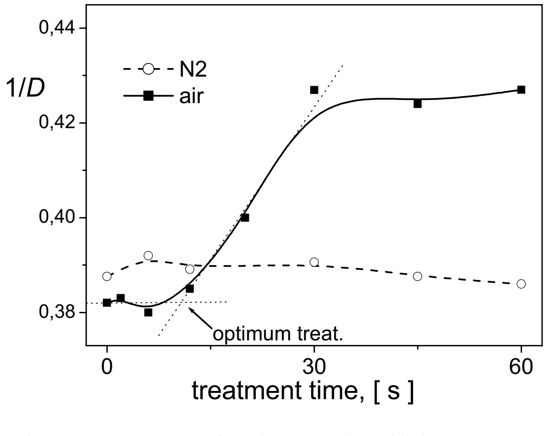

Fig. 4. **Reverse value of optical density of foils on black paper as a function of treatment time (proportional to ligth scattering)**

than in common air. This confirms also the SEM pictures of nontreated and treated PP surfaces in DBD (Fig. 5.).

On the contrary, zeta potential of foils treated in common air atmosphere did not change practically, however, the potential of PP foils treated in nitrogen were changed considerably, Fig. 6. The initial acidic groups present at the original surface of the PP foil were suppressed and replaced by nitrogen basic groups[3,7,9] represented by the decrease of negative zeta potential in basic region. So the surface treated in nitrogen is more basic with the isoelectric point shifted a little to the higher pH position.

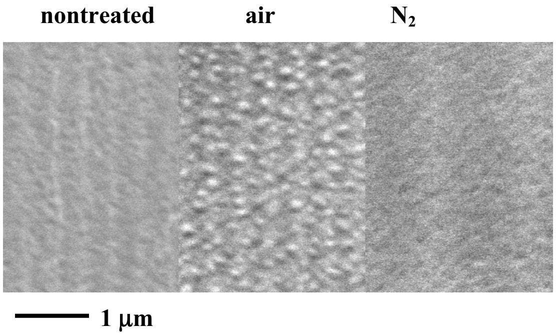

Fig. 5. **SEM of PP foils, initial and after 30 s treatment in air and N_2**

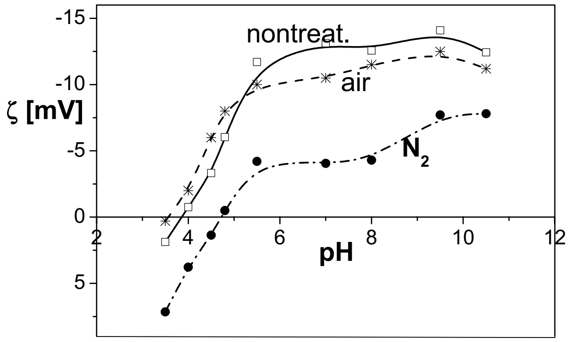

Fig. 6. **Zeta potential of PP foils, initial and after 30 s treatment in air and N_2**

The polar character of degradation product confirms also rinsing of treated foils in different solutions and measuring the UV absorption of resulted solutions (Fig. 7., 8.). The volume of the rinsed product by n-heptane is practically zero (Fig. 7.). On the other hand, the absorption of polar solutions achieves high values, however, no induction period at treatment time dependence was found (Fig. 8.). pH dependence on treatment time indicates the increase of basic groups in nitrogen DBD treatment and acidic groups (carboxyls) in the air treatment (Fig. 9.).

Adhesion of gravure ink applied on treated PP foils was tested by adhesive tape stripping. Ink adhesion was generally higher (or the same) in the case of nitrogen than of the air DBD treatment.

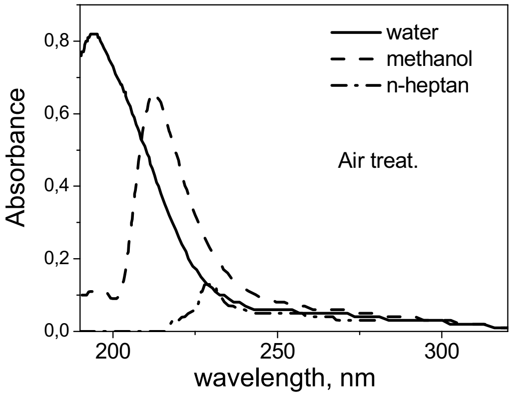

Fig. 7. **UV absorption spectra of rinsed foils solutions after 30 s in air DBD**

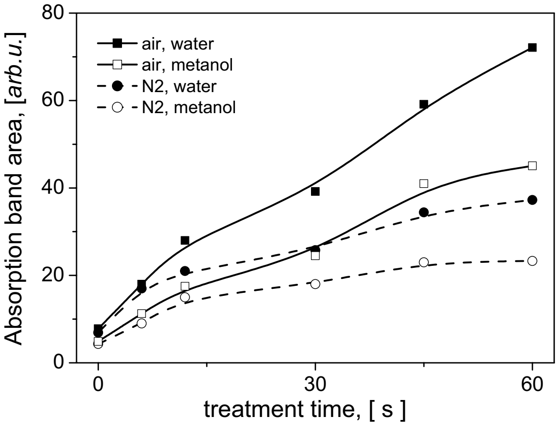

Fig. 8. **UV absorption band areas of rinsed foils solutions as a function of treatment time**

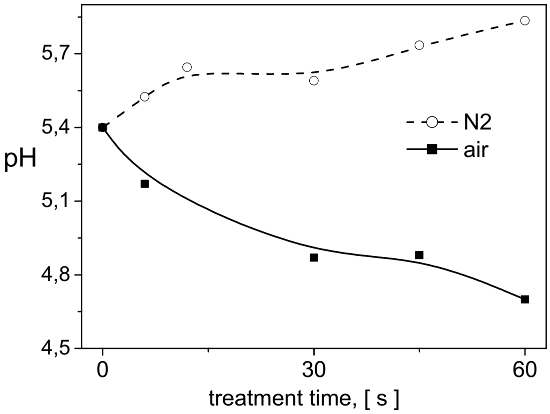

Fig. 9. **pH dependence of rinsed foils solutions on treatment time**

Conclusion

Application of DBD plasma in air at atmospheric pressure onto the BOPP surface creates a rather high amount of degradation products and increases roughness. The gloss or density measurements can be used to determine the optimum exposition.

Nitrogen plasma is less destructive, PP surface remains smooth and compact with a low amount of degradation products, while the adhesion to ink is as high as in the case of air DBD. However, the optimum treatment can not be found easily from gloss or density measurements. Zeta potential and pH measurements confirm that air DBD plasma creates acidic groups and nitrogen plasma basic groups at the PP surface.

This study was supported by Slovak Scientific Grant Agency, VEGA, Ministry of Education of the Slovak Republic, No. 1/2454/05.

REFERENCES

1. Mikula M., Jakubíková Z., Zahoranová A.: J. Adhesion Sci. Technol. *17*, 15, 2097–2110 (2003).
2. Murokh I.: *Atmospheric Plasma Surface Treatment Technique,* Tri-Star Technologies, El Segundo, California 2000.
3. Sun C. Q., Zhang D., Wadsworth L. C.: Advances in Polym. Technol. *18*, 2, 171 (1999).
4. Boyd R. D., Kenwright A. M., Badyal J. P. S., Briggs D.: Macromolecules *30*, 5429 (1997).
5. Sira M., Trunec D., Stahel P., Bursikova V., Navratil Z., Bursik J.: J. Phys. D-Appl. Phys. *38,* 621 (2005).
6. Černák M., Ráhel J., Štefečka M., Kando M.: Proc. of The 17th *Symposium on Plasma Processing,* Nagasaki, Japan 26–28 January 2000, pp. 535–538.
7. Tušeka L., Nitschke M., Werner C., Kleinschek K. S., Ribitsch V.: Colloids and Surfaces A: *195*, 81 (2001).
8. Kogelschatz U., Eliasson B., Egli W.: *Dielectric Barrier Discharges, Principles and Application.* Proc. of Int. Conf. on Phenom. in Ionized Gases, ICPIG XXIII, Toulouse 1997, p. C4–47.
9. Jaehnichen K., Frank J., Pleul D., Simon F.: J. Adhesion Sci. Technol., *17*, 1635 (2003).

L10 METHODS FOR PRINTABILITY DETERMINATION OF THIN POLYMER LAYERS

IVA KRÁLOVÁ, MICHAL VESELÝ
and OLDŘICH ZMEŠKAL
Brno University of Technology, Faculty of Chemistry, Department of Physical and Applied Chemistry, Purkyňova 118, 612 00 Brno, kralova@fch.vutbr.cz

Introduction

The quality of inkjet printing depends on printers and its printing media and is evaluated by means of practical printing tests and subsequent fractal analysis of printed test patterns. By this method, the size of a visually different fraction of the studied surface can be easily determined. This paper describes traditional and new methods of surface area calculation, their comparison and practical use. Image analysis is used to determine the ink coverage in a study of the printability of new inkjet media based on modified PVAl, which is coated as thin polymer layer onto substrate (paper, film,…).

The parameters of inkjet quality and materials

The most of inkjet printing media are coated bearing surface as paper or thin polymer layer. The ink receiving layers consist thin layer of hydrophilic, water-swellable polymer (PVAl, gelatine and their derivatives). When an ink drop is deposited on the surface, the ink is absorbed by the polymer layer.

There are many parameters, which is evaluated as important for printing quality, it means the complex of usable properties, which comply with requirements of usefulness for customer, Such properties include: quality of handwriting, image original, quality of graphic and typographic design, but also quality of own realisation of printing[1]. High quality ink jet printers are often named as „photorealistic“, meaning the quality of prints they produce approaches the colour gamut, resolution, sharpness, dynamic range, gloss, permanence and durability.

The print quality is also influenced by surface defects and as point of view of printing materials is related with area non-symetricity as thickness, area weight, translucence, porosity, suction capacity, anisotropy (rigidity, expansibility), different quality of front and reverse side (roughness, suction capacity, gloss, brightness) and at the end with hygroskopicity (it means influence of temperature and humidity on properties changes).

The most usual print medium is paper based on cellulose. This paper has got some disadvantages and problems as porosity structure, the roughness and heterogeneity of its surface. So ink is soaked and transported to the inside of paper and it leads to low optical density.

A significant increase ink inkjet print quality was achieved by the introduction of dedicated media, which is called ***barrier-type.*** These media consist of inert (water resistant) base, which is usually made of paper double-sided laminated by PE. Another type of media consist inert base (paper, foil …), which is coated by thin polymer layer with specific properties. This special ink receiver layer consists of hydrophilic, water-swellable polymer as PVAl, gelatine and their derivative responsibility, which developed inkjet quality. When an ink drop is fallen down to surface, the ink is absorbed by the polymer layer. This design brings major improvement compared to paper: the media surface can be produced with high smoothness and gloss, such the sharpness and excellent resolution are obtained.

The methods of image analysis

The special instruments as densitometers (determined to measuring of optical density) and colorimeter (measuring the coloured print quality) are used to measuring of density as classical methods. At the other hand there are used instruments for digitised image templates which are named image-forming photometers. The speed, quality, objectivity, infallibility and reproducibility of computing image analysis are the most important parameters, which lead to expansion of these methods. There is concretely fractal image analysis, which is based on the determination of image segmentation. Such we obtain these two important parameters: the fractal measure K and fractal dimension *D*. The value of ink coverage can be obtained by determining these parameters, because we calculate number of black, white and black-white pixels[2]. The evaluation of ink coverage was determined by image analysis methods as Classic Box Counting and Box Counting method based on wavelet transformation[3]. The coefficients (fractal measure *K* and fractal dimension *D*) show characteristic data about analysing structure. We used special software with these transformations for image analysis as programs AnalySIS, LUCIA, LabVIEW, BENOIT and owner software HarFA. However, it obtains two different transformations – Fourier and wavelet, both of them determine segmentation masking image[4].

Experimental comparison of two methods

Classic Box Counting method

Fractal dimension and fractal measure are obtained by using variation of Box Counting Method. By this technique we can examine black & white fractal structures which come into existence during process called "thresholding", which transforms coloured image object into black & white one. If you want to characterize image by its fractal dimension, you don't know which of them is appropriate, so it must be applied range analysis on analyzed image, which was sampled to 256 levels of grey. Then, using HarFA's function "Fractal Analysis/Range", the recorded grey-scale image was 256 times converted into black-and-white image, each time with different threshold level. The fractal dimension was then calculated for each of the 256 levels, which gives us information about optimal masking threshold level. Afterwards the image was masked and result of this analysis is plot showed the ln N (*r*) vs. ln (*r*) dependence, from which the numbers of black, white and partially black and white pixels could be calculated. These numbers of black pixels plus a half of black-and-white pixels corresponds to the ink coverage of the print[5].

Box Counting method based on wavelet transformation

Wavelet analysis means 1D or 2D Haar transform of image information. Wavelet analysis is provided by using fast algorithm calculation, where we use analysed area, which can be set on 32, 64, 128, 256, 512, 1024 or 2048 pixels. We can measure values of intensity (shades of grey), hue, red, green or blue components of colour information in 1D space or in 2D space. Such we can obtain some different plots and also 3D graph of image as is showed on the picture below.

For special case is equal with classical box-counting method. So method is the same. We must find the best masking threshold level ("Fractal Analysis/Range").

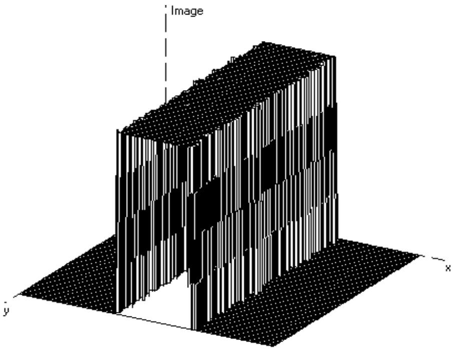

Fig. 1. **Fractal spectrum – 3D graph**

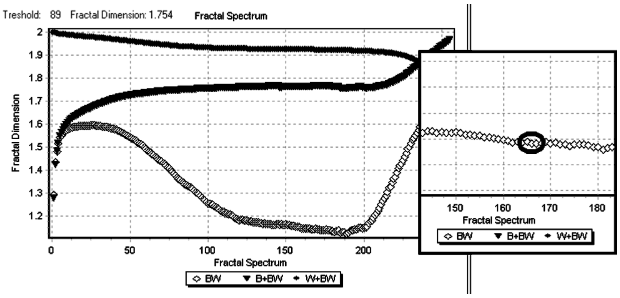

Fig. 2. **Fractal spectrum of study image and ideal treshold level**

The graph below shows the ideal point on the curve (the part of curve parallel with greyscale level axis which is near fractal dimension value 1). Further the image is masked on the chosen threshold level in our case 165.

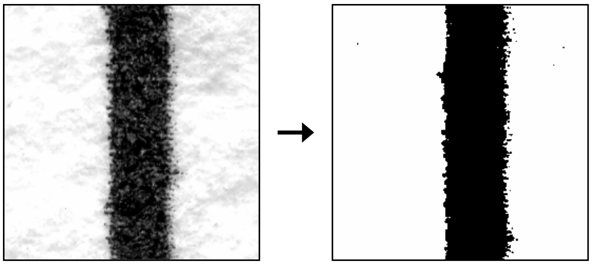

Fig. 3. **Analysed image and image masked at the treshold level 165**

Afterwards is calculated the number of black pixels, white pixels and black & white pixels (Fig. 4.). These numbers corresponds to the ink coverage of the printed surface.

The advantages of wavelet analysis are method speed, reproducing and math accuracy. The amount of black, white and black & white pixels is calculated according to formula below:

$$B\,[\%] = \frac{BW + BW/2}{BBW + WBW + BW/2} \cdot 100\,,$$

where *BBW* is sum of black and black & white pixel, *BW* is number of black & white pixel and *WBW* is sum of white and black & white pixel. These numbers are obtained by regress straight line antilogarithm of dependence ln (N) vs. ln (r):

$$BW = e^{\mathrm{bw}}$$

$$BBW = e^{\mathrm{bbw}}$$

$$WBW = e^{\mathrm{wbw}} ,$$

where *BW, BBW* a *WBW* are fractal measure (logaritmus values) of regress straight line translation (ln (N) = a ln (r) + b), where "a" is fractal measure and "b" is fractal dimension.

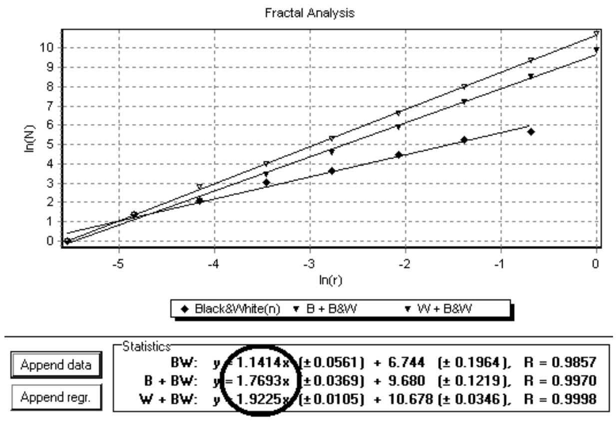

```
BW:     y = 1.1414x (±0.0561) + 6.744  (± 0.1964),  R = 0.9857
B + BW: y = 1.7693x (±0.0369) + 9.680  (± 0.1219),  R = 0.9970
W + BW: y = 1.9225x (±0.0105) + 10.678 (± 0.0346),  R = 0.9998
```

Fig. 4. **Data of fractal analysis for tresholded image**

Comparison of several methods

We choose classical method – densitometry and new methods Classic Box Counting and Box Counting method based on wavelet transformation for evaluation of ink coverage of printing surface. The figure below shows that both methods of image analysis reached similar results. The classical method densitometry doesn't reach exact results and demand calibration process. On the other hand, the methods of fractal analysis – both reach the same values if ink coverage in percentages for evaluation of printing surface.

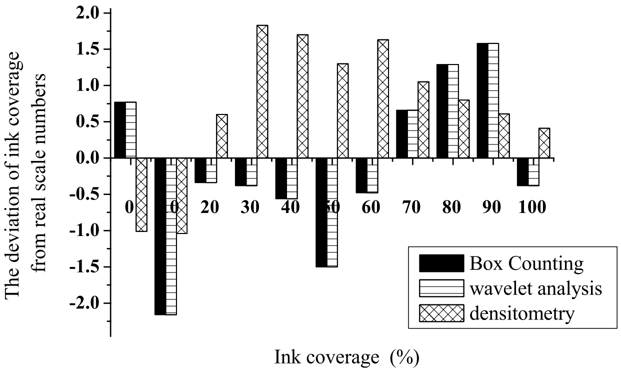

Fig. 5. **The comparison of methods box counting, wavelet transformation and densitometry**

Conclusion

When speaking about the ink coverage determination, it is important to note that the new methods of image analysis as fractal methods have one significant advantage over the classical way of determining the ink coverage, i. e. the reflection densitometry. Reflection densitometers have to be carefully calibrated, while these methods require no calibration at all.

The results show that methods of image analysis – box counting and wavelet transformation give the same values of ink coverage in evaluation of printing surface. So we can say that the advantages of wavelet analysis as method speed, reproducing and math accuracy are suitable for other evaluation.

REFERENCES

1. Panák, J., Čeppan, M., Dvonka V., Karpinský L´, Kordoš P., Mikula M., Jakucewicz S.: *Polygrafické minimum,* TypoSet, Bratislava 2000.
2. Zmeškal O., Nežádal M., Sedlák O.: *The Usage of Fractal Analysis for Evaluating the Quality of Print, IV. Polygraphic Conference,* University of Pardubice, 2003.
3. Zmeškal O., Julinek M., Bzatek T.: *The Image Analysis of print materials and printed surfaces, V. Polygraphic Conference,* University of Pardubice, 2003.
4. Zmeškal O., Nežádal M., Buchníček M.: *The Box Counting-Critical Study,* http://www.fch.vutbr.cz/lectures/imagesci/boxconting.htm, Brno, 2000.
5. Dzik P.: *Fractal analysis – a different approach to the study of printability, 4th International conference of PHD students,* University of Miskolc, 2003.

L11 STUDY OF INFLUENCE OF UNI-UNIVALENT ELECRTOLYTE TRACES ON DIELECTRIC PROPERTIES OF HYDROXYETHYLCELLULOSE

ALENA MACHÁČKOVÁ, PAVEL URBAN
and LIBOR INDRÁK
Institute of Physics and Material Engineering, Faculty of Technology, Tomas Bata University, Nad Stráněmi 4511, 760 05 Zlín, Czech Republic

Abstract

There was studied an influence of small traces of NaF, KBr, LiI and two types of tenzides (sodium laurylsulphate, cetylpyridinium bromide) on dielectric properties of hydroxyethylcellulose (HEC) thin films in the range of frequencies from 100 MHz to 1.2 GHz, and at the constant temperature 25 °C. Three types of HEC of industrial provenience were subjected to this study (Natrosol 250L, Natrosol 250MR and Natrosol 250HHBR); all samples of purity “for scientific use” from Hercules Inc..

Introduction

Dielectric properties measurements belong to elegant methods to investigation of intra- and intermolecular dynamics of polymer in general. In all polysaccharides there are three types or modes of dielectric relaxation processes[1]. The so called β- and γ-relaxation at low temperatures (–135 °C to 0 °C): the β-relaxation is associated to the local main chain motion of the polymer and the γ-relaxation to thermal activated side group motion of the anhydroglucose unit. In the middle temperature range (0 °C to 60 °C) a further relaxation process exists, which is attributed to motions in regions in a polysaccharide-solvent mixing state. This so called β_{wet}-relaxation-relaxation is very sensitive to small traces of electrolytes and water[2–4].

The complex dielectric constant

$$\varepsilon^*(\omega) = \varepsilon'(\omega) - i\varepsilon''(\omega) \qquad (1)$$

has two parts: the real part of the complex permittivity (CP), ε’(ω) (dielectric store coefficient) and ε’’(ω) is the imaginary part of the CP (dielectric loss coefficient). The symbol ω in Eq. 1 is the angular frequency:

$$\omega = 2\pi f \ . \qquad (2)$$

All separable relaxation processes (index i) in a complex polymer molecule influence the mean measured values of complex permittivity:

$$\varepsilon^*(\omega) = \varepsilon_\infty + \sum_i \Delta\varepsilon_i^* \ , \qquad (3)$$

where ε_∞ is extrapolated real part of the high frequency end of the measuring window. For the complex contribution of the i^th^ relaxation process S. Havriliak and S. Negani[5] have introduced the following equation:

$$\Delta\varepsilon_i^* = \Delta\varepsilon / [1 + (i\omega\tau_i)^{\alpha_i}]^{\beta_i} \ , \qquad (4)$$

which describes each relaxation process by four relaxation parameters:

1. τ_i(T), the relaxation time,
2. $\Delta\varepsilon_i$(T), the relaxation strength,
3. α_i(T), the shape parameter, illustrates the width of relaxation response and
4. β_i, the asymetry parameter (for Debye process $\alpha = \beta = 1$).

Results and Discussion

The results of measurement were taken from the one on the thin solid films prepared by fast plaster casting from 2% wt. water solutions of HEC:

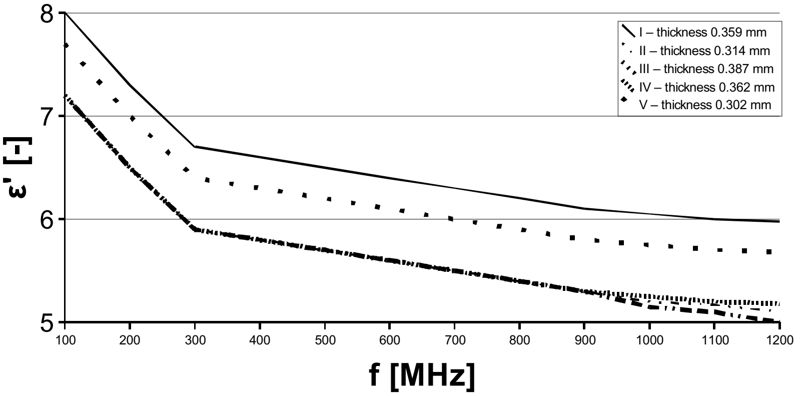

Fig. 1. **The dependence of real part of permittivity on frequency for HEC 250L for sample No. 1.2 in 5 points**

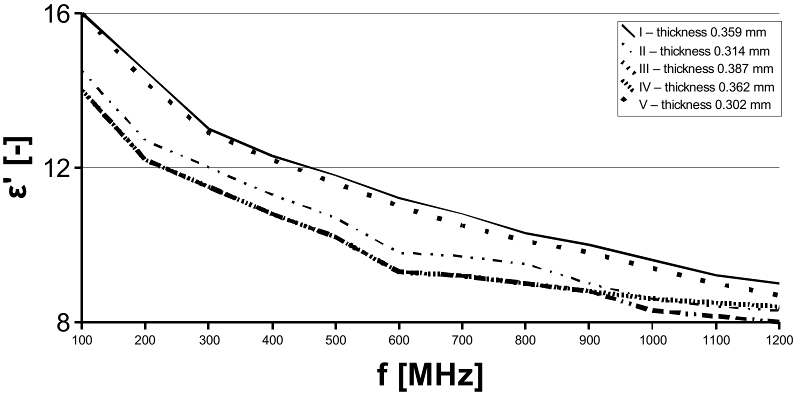

Fig. 2. **The dependence of imaginary part of permittivity on frequency for HEC 250L for sample No. 1.2 in 5 points**

Table I
The starting solution of Natrosol 250L composition before solvent evaporation (wt. %)

			Component concentration			
	Derivative		Electrolyte		Tenside	
Sample No.	HEC	NaF	KBr	LiI	$C_{12}H_{25}NaO_4S$	$C_{12}H_{38}BrN . H_2O$
1.2	3.85	–				
1.3	3.85	–				
1.4	3.84	$3.85 . 10^{-4}$				
1.5	3.88	–	$3.84 . 10^{-4}$			
1.6	3.88	–		$3.84 . 10^{-4}$		
1.7	3.84	$3.84 . 10^{-4}$			$3.84 . 10^{-4}$	
1.8	3.84	$3.84 . 10^{-4}$			$3.84 . 10^{-4}$	
1.9	3.84	$3.84 . 10^{-4}$				$1.15 . 10^{-3}$
1.10	3.84	$3.84 . 10^{-4}$				$1.15 . 10^{-3}$
					(*)[1]	(*)[2]

(*)[1] sodium laurylsulphate
(*)[2] cetylpyridinium bromide

In all cases the concentration of polymer in solution was 3.85 wt. % (Table I) and the electrolyte and tenside concentrations were the same as in given for Natrosol 250L.

The results of measurements were realized with Impedance Hewlett-Packard 4291 A Analysator at constant temperature 25 °C in an isolated measuring chamber with controlled atmosphere of extremally dry air.

The frequency dependences of real part of CDC ε'(f) are for illustration given in Fig. 1., and for imaginary part ε''(f) in Fig. 2. There is quite evident great influence of specimen thickness on the received data. There are also another possibilities to an explanation: surface of HEC samples could be easily effected by sorption of small amounts of water vapours. With increasing thickness of polymeric film probably increases also amount of water traces inside of the sample. On the other hand, the strong abbility of HEC to create organized aggregates through hydrogen bonds could contribute to the variety of structural modes and then to differentiation in surface and bulk structural arrangement. In general, three types of aggregates may be supposed: star-type, H-type and comb-type. A detailed study of this aggregation during solvent evaporation from polymer solution has been given by S.Sakurai and co-workers[6]. According to authors[5] a dominant factor influencing the self-aggregation is velocity of evaporation. With increasing thickness of the final film decreasing diameter of structural cell-type arrangement on the surface is evident. There is also evident that the process of gelation is closely connected with convection of heat in the surface which leads to a periodic structural elements creation.

Small amounts of the binary electrolytes (NaF, KBr, LiI) and cation-active and anion-active tenside decrease real and imaginary parts of dielectric constant in all measured frequency range for all studied samples.

REFERENCES

1. Einfeldt J., Kwasniewski A., Klemin D., Dicke R., Einfeld L., Polymer *41*, 9273 (2000).
2. Crofton D. J., Pethrick R. A., Polymer *22*, 1048 (1981).
3. McBrierty V. J., Faraday Discuss *103*, 254 (1996).
4. Einfeldt J., Das Papier *53*, 1774 (1996).
5. Sakurai S., Furukawa K., Okutsu A., Miyoshi A., Nomera S., Polymer *43*, 3101 (2002).

L12 STEADY STATES ESTABLISHMENT DURING PYRITE OXIDATION

IVA BARTÁKOVÁ[a, b] and JOSEF ZEMAN[a]
[a]*Department of Mineralogy, Petrography and Geochemistry, Faculty of Science, Masaryk University, Kotlářská 2, 611 37 Brno, Czech Republic, 15124@mail.muni.cz,* [b]*Department of Biochemistry, Faculty of Science, Masaryk University, Kotlářská 2, 611 37 Brno, Czech Republic*

Introduction

The weathering of pyrite by ferric iron is usually expressed as

$$FeS_2 + 7\ Fe_2(SO_4)_3 + 8\ H_2O \rightarrow 15\ FeSO_4 + 8\ H_2SO_4 \qquad (1)$$

Several reactions have the key role during chemical oxidation of pyrite. The first of these reactions is pyrite oxidation by ferric iron, the second is oxidation of ferrous iron by dissolved oxygen to ferric iron and the third is precipitation of ferric hydroxide. The oxidation rate of ferrous iron to ferric iron is slow reation in sulfuric acid solution below pH value of 2. Ferric hydroxide is probably a catalyst for the oxidation of ferrous iron in neutral solution[1]. Wiersma and Rimstidt expressed the rate of pyrite degradation by ferric iron under the conditions of pH 2 in hydrochloric acid solution by the equation[2]:

$$-\mathrm{d}m_{\mathrm{Fe}^{3+}} / \mathrm{d}t = \mathrm{k} \cdot (A/M) \cdot m_{\mathrm{Fe}^{3+}} \qquad (2)$$

where $m_{\mathrm{Fe3+}}$ is the molality of the noncomplexed Fe^{3+}, *A/M* is the rate of surface area and solution volume, k is the rate constant. It was found by Boogerd et al. that the sulfur moiety of pyrite was oxidized completely to sulfate in hydrochloric acid[3]. Ferrous iron formed during the reaction slows down the oxidation of pyrite by ferric iron. The reaction of ferric iron with pyrite starts very far from equilibrium, so there is no significant back reaction. The initial rate of pyrite oxidation can be fitted to a general differential rate law of the form $r = \mathrm{k} . m^{\mathrm{n}}$, where r is the decrease of Fe^{3+} in mol kg^{-1} m^{-2} s^{-1}. Rimstidt and Newcomb found $\mathrm{k} = 3.0(\pm 2.0) . 10^{-5}$ mol m^{-2} s^{-1} and $\mathrm{n} = 0.62\ (\pm 0.10)$ in hydrochloric acid[4]. The results suggested the existence of some inhibitor among the products of this reaction in the later phase. The effect of SO_4^{2-}, Cl^-, ionic strength, and dissolved oxygen on the rate of reaction of pyrite with ferric iron was studied. Of these, only dissolved oxygen was found to have any appreciable effect. The pyrite dissolution rate (mol m^{-2} s^{-1}) for the range of pH 0.5–3.0 without dissolved oxygen in the system was described by the Equation[5]:

$$\nu = 10^{-8.58(\pm 0.15)} \cdot m_{\mathrm{Fe}^{3+}}^{0.30(\pm 0.02)} \cdot m_{\mathrm{Fe}^{2+}}^{-0.47(\pm 0.03)} \cdot m_{\mathrm{H}^{+}}^{-0.32(\pm 0.04)} \qquad (3)$$

Similarly, the pyrite dissolution rate (mol m^{-2} s^{-1}) in the system with dissolved oxygen was described by the Equation[5]:

$$\nu = 10^{-6.07(\pm 0.57)} \cdot m_{\mathrm{Fe}^{3+}}^{0.93(\pm 0.07)} \cdot m_{\mathrm{Fe}^{2+}}^{-0.40(\pm 0.06)} \qquad (4)$$

Because the fractional orders of reaction were difficult to explain with a purely molecular-based mechanism, a cathodic-anodic electrochemical mechanism was favoured to explain the transfer of the electron from pyrite to the aqueous oxidant. Nayak et al. observed that the initial dissolution is a transient phenomenon characterised by decay in dissolution rate with time[6]. The rate correlated strongly with Eh. The effect of the redox potential on the ferric leach rate was investigated by dynamic redox potential measurement[7]. Chemical oxidation rate of pyrite increases with increasing ferric to ferrous iron concentration ratios $[Fe^{3+}]/[Fe^{2+}]$(ref.[8]).

Experimental

Pulp density of 2 % was used, 100 ml of solution was added to 2 g of pyrite (the mean partical diameter under 0.1 mm). The composition of the solution was distilled water acidified to pH 1.0–1.7 by sulfuric acid, the iron concentration was adjusted by standardized ferric sulfate or ferrous sulfate (p. a. purity). The suspension was incubated in 500 ml round bottom flasks at 26 °C on a rotary shaker. $[Fe^{3+}]$ was determined spectrophotometrically at 300 nm using a Shimadzu UV 3000 spectrophotometer (Japan) or Ultrospec 2000 UV/Visible spectrophotometer (Sweden)[9]. $[Fe^{2+}]$ was determined by titration with $KMnO_4$ in sulfuric acid. Total iron concentration was obtained as sum of ferric and ferrous iron concentration and several samples were determined by atomic absorption spectrometry (Perkin-Elmer 4000, USA) in an acetylene air flame. pH was determined from pH values using Radiometer PHM 93 pH meter. Redox potential was monitored using platinum electrode (Radiometer Copenhagen) against Ag/AgCl electrode and recalculated to absolut hydrogen scale value.

Results and discussion

The most significant decrease of ferric iron concentration and production of ferrous iron appear at the beginning of the reaction of ferric iron and pyrite, and these trends are not transparent in the later period due to steady states establishment. The concentrations of all soluble components depend on each other due to the existence of cycle of iron oxidation and reduction and due to chain of the reaction resulting to the formation of complexes. It is evident from the development of total iron concentration with time that the chemical degradation of pyrite continues under the conditions of steady state. The value of the slopes from linear plots of total iron concentration against time increases with increasing initial concentrations of ferric iron in the system. During our experiments the redox potencial values decreased to the values characteristic for steady state (Fig. 1.). The abrupt decrease of redox potential at the beginning of the reaction is the consequence of the changes of $[Fe^{3+}]/[Fe^{2+}]$ ratio during the fast reduction of ferric iron to ferrous iron. No precipitates of ferric hydroxide and secondary minerals were observed in the studied systems. The time trends in the plot of log [Fe^{3+}] against pH (Fig. 2.) viewed left downwards reflect the ferric iron decrease caused by the reduction processes and sulphuric acid production.

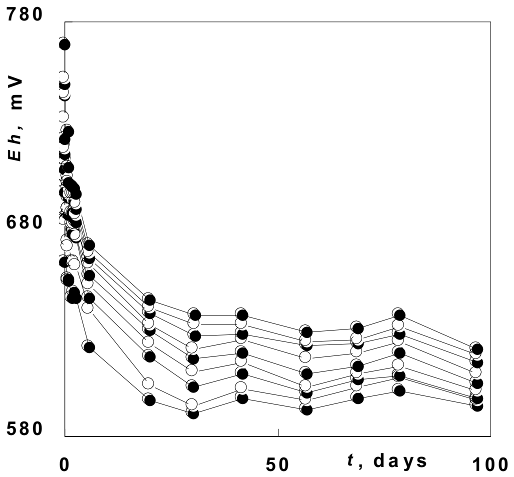

Fig. 1. **Decrease of redox potential in time during the long time oxidation of pyrite by ferric sulfate under conditions of a pulp density of 2 %. Initial concentrations of ferric iron corresponding to the particular curves bottom-up mM were: 11.8, 20.2, 39.0, 57.0, 75.8, 93.9, 111.0, 143.0, 203.0 mM**

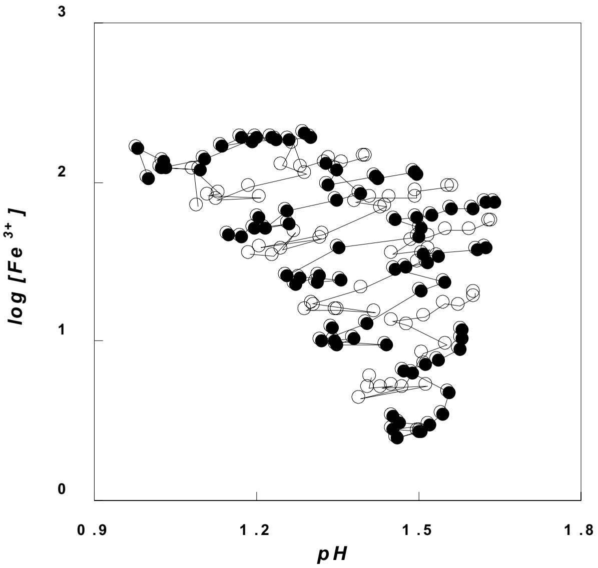

Fig. 2. **Long time oxidation of pyrite by ferric sulfate under conditions of a pulp density of 2 %. The initial concentrations of ferric iron were: 11.8, 20.2, 39.0, 57.0, 75.8, 93.9, 111.0, 143.0, 203.0 mM. Plot of log [Fe^{3+}] (the concentrations were used in mM) against pH**

Fig. 3. demonstrates the dependence of [Fe^{3+}]/[Fe^{2+}] ratio on the total soluble iron concentration for the systems in steady states. The aim of the system to adjust [Fe^{3+}]/[Fe^{2+}] to the value characteristic for the steady state is realized by ferric iron reduction in the case of initial ferric iron prevalence and by acceleration of ferrous iron oxidation in the case of initial ferrous iron prevalence. The more total iron is present in the solution, the higher is the rate of ferric form. The disagreement of our observation of the increased rate of pyrite oxidation in relationship with the increased initial total iron concentration compared with the consideration of Maye et al. about independence of the pyrite oxidation rate on the total iron concentration is apparent, because May et al. obtained the results under the conditions of constant redox potential[7]. Our study describes the natural development of the parameters including the natural redox potential.

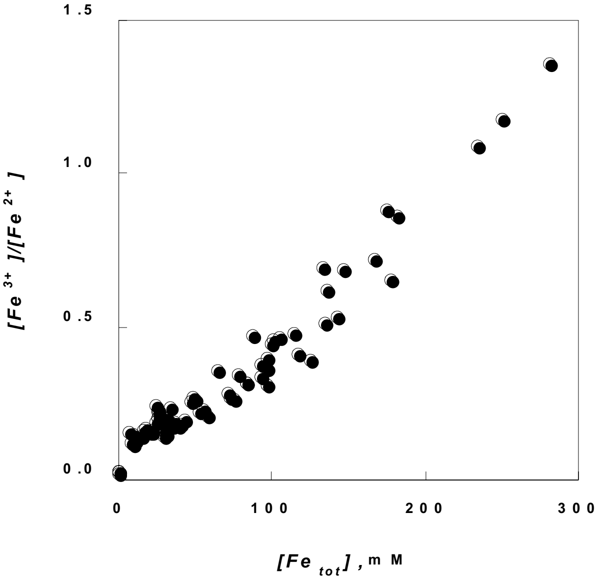

Fig. 3. **The concentration parameters of the systems in steady states. Plot of [Fe^{3+}]/[Fe^{2+}] against [Fe_{tot}] in mM**

It is evident from Fig. 4., that the steady state concentration of Fe^{2+} tends in respect of increasing concentration of H^+ to some limit, whereas the concentration of Fe^{3+} in relationship with increasing acidity permanently increases.

The slope of the linear plot log ([Fe^{3+}]/[Fe^{2+}]) against pH was nearly –2 for the experiments performed in the pH less than 1.52. Therefore, the plot of the square of concentration of [H^+] against the [Fe^{3+}]/[Fe^{2+}] ratio is linear with the equation:

$$[H^+]^2 = k_1 \cdot ([Fe^{3+}]/[Fe^{2+}]) \quad (5)$$

where $k_1 = 7315$ mM^2.

The comparison of the position of the observed steady-states systems in the plot of Eh against pH and the Eh-pH diagram of ascendant composition (Fig. 5.) shows that the experimental values are placed in the area with ferrous iron as the main component near the border Fe^{2+}/mineral. This position is a result of simultaneous existence of pyrite as reduced component and ferric iron as oxidized component together. The placing of the experimental values near the border Fe^{2+}/mineral bear on the tendency of the systems to

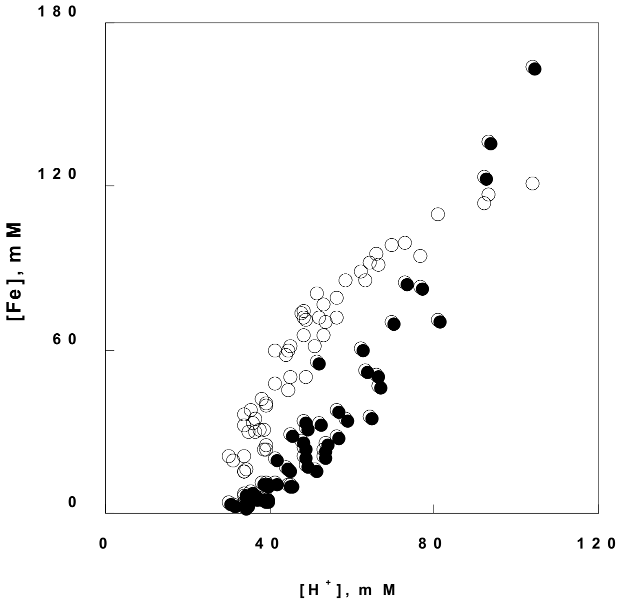

Fig. 4. **The concentration parameters of the systems in steady states. Plot of $[Fe^{3+}]$ (●) and $[Fe^{2+}]$ (○) (in mM) against $[H^+]$ (in mM) for the experiments with pH less than 1.52**

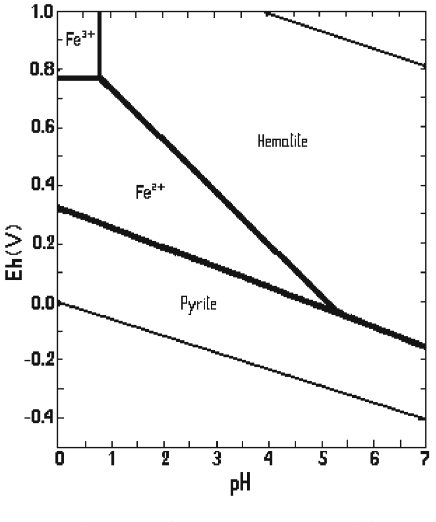

Fig. 5. **Eh-pH diagram of ascendant composition**

exist under the conditions of limiting saturation values. The appearance of the steady states system in the area with predominance of ferrous iron is in agreement with our knowledge of the most frequent ratio $[Fe^{3+}]/[Fe^{2+}]$ value less than 1. The development along the bevel trajectory upwards entail the decrease of the free form Fe^{2+} in favor of the Fe^{3+} form since the system converge to the border partitioning the Fe^{3+} area from Fe^{2+} area.

Conclusions

Chemical steps of pyrite oxidation were studied under different initial conditions of pH, Eh, concentration of ferric and ferrous iron. The dissolution rate of pyrite increased with increasing ferric iron concentration. After initial transient period, steady-state with dynamic character seemed to be established in all systems. The initial conditions in the system, i. e. the difference between the initial and steady state concentrations, influence the time required for reaching of the steady state. The simple equation describes relationship between the steady state parameters: $[H^+]^2 = k_1 . ([Fe^{3+}]/[Fe^{2+}])$, the k_1 value was estimated 7315 mM^2. Aiming to reach of steady state is a phenomenon observed in majority of natural systems. Apparently, owing to this mechanism, these systems are able to balance the exterior intervention.

This work was supported by grant No. 525/97/0340 from the Grant Agency of the Czech Republic.

REFERENCES

1. Lowson R. T.: Chem. Rev. *82*, 461 (1982).
2. Wiersma C. L., Rimstidt J. D.: Geochim. Cosmochim. Acta *48*, 85 (1983).
3. Boogerd F. C., van den Beemd C., Stoelwinder T., Bos P., Kuenen J. G.: Biotechnol. Bioeng. *38*, 109 (1991).
4. Rimstidt J. D., Newcomb W. D.: Geochim. Cosmochim. Acta *57*, 1919 (1993).
5. Williamson M. A., Rimstidt J. D.: Geochim. Cosmochim. Acta *58*, 5443 (1994).
6. Nayak B. B., Paramguru R. K., Ray H. S.: Transactions of the Indian institute of metals *48*, 35 (1995).
7. May N., Ralph D. E., Hansford G. S.: Minerals Eng. *10*, 1279 (1997).
8. Boon M., Heijnen J. J.: Hydrometallurgy *48*, 27 (1998).
9. Mandl M., Nováková O.: Biotechnol. Technique *7*, 573 (1993).

L13 THE APPLICATION OF FACTOR ANALYSIS OF VIS-NIR SPECTRA TO IDENTIFICATION OF IRON-GALL INKS

MICHAL ČEPPAN[a] and JOHANN G. NEEVEL[b]
[a]Faculty of Chemical and Food Technology, Slovak University of Technology, Radlinského 9, 81237 Bratislava, Slovakia, michal.ceppan@stuba.sk, [b]Conservation Research Dept, Netherlands Institute for Cultural Heritage, P. O. Box 76709, 1070 KA Amsterdam, The Netherlands, Han.Neevel@icn.nl

The identification of brown inks is of importance to understand the history and aesthetics of an object, to evaluate the risks involved with its use, and to judge the effects of conservation treatments. Drawings may contain different brown shades side-by-side, which could be due to the use of different drawing inks. Traditionally, to obtain brown shades, bistre, sepia, carbon black and iron gall inks were used[1]. Iron gall inks contain transition metals, such as iron and copper, catalysing the radical oxidation of the substrate, as well as acids, catalysing its hydrolysis[2]. These degradation processes, generally known as "ink corrosion", lead to the formation of fluorescent and brown degradation products, followed by mechanical weakening of the paper and formation of cracks. If none of these phenomena are observed, it is not easy to visually distinguish iron gall inks from other, potentially less aggressive, brown inks.

Different instrumental analytical methods, e. g. SEM/EDX, have been applied to identify inks[3]. As most collection keeping institutes do not have access to these techniques, there is a need for "hands-on" methods that do not require sampling or transport of the object outside the institute. Nowadays, Fibre-Optics Reflectance Spectrometers (FORS) have reached dimensions which allow them to be transported easily to the objects to be measured.

It is shown in this paper, that these inks can be distinguished by the reflectance spectra obtained from visually comparable shades of sepia, bistre and iron gall inks, covering a range of compositions, processed by chemometric factor analysis methods.

Experimental

In order to test the possibilities of the fibre-optics spectrophotometer to distinguish bistre, sepia and iron gall ink by their spectral characteristics, samples of these inks were prepared according to the traditional recipes and applied in different layer thicknesses to paper by the aid of computer-guided plotter equipped with refillable pen. All model samples were artificially aged an oven at 90 °C and RH cycling every 3 hrs between 80 and 35 %.

Applying the AvaSpec-2048 fibre optic spectrophotometer[4] and a halogen lamp, the reflectance spectra of the artificially aged model samples and reflectance spectra of inks on original 17th century drawing (kindly provided for by Teylers Museum, Haarlem, The Netherlands) were determined over the wavelength range between 350 and 1100 nm. An area of blank paper, near the ink application, was used as a white calibration standard.

Computational

Factor analysis is generally preferred for its ability to determine the number of components or factors creating the given spectra set and for its ability to classify and characterize these factors[5,6].

Let n_S be the number of spectra in a studied set sampled at n points. Spectra are arranged in column in matrix $\boldsymbol{R}$, and each spectrum is represented by an n-dimensional vector $\boldsymbol{r}$. The first step of factor analysis, principal component analysis (PCA), is diagonalization of square symmetrical matrix $\boldsymbol{Z}$ ($\boldsymbol{Z} = \boldsymbol{R}\ \boldsymbol{R}^{\mathrm{T}}$; also called the scatter matrix). Orthonormal matrix of eigenvectors $\boldsymbol{Q}$ (with single eigenvectors $\boldsymbol{q}_{\mathrm{k}}$ in its columns) ordered according to the descending values of corresponding eigenvalues is obtained. Matrix $\boldsymbol{R}$ can be now expressed as

$$\boldsymbol{R} = \boldsymbol{Q}\ \boldsymbol{U} \tag{1}$$

where

$$\boldsymbol{U} = \boldsymbol{Q}^{\mathrm{T}}\ \boldsymbol{R} \tag{2}$$

A set of eigenvectors $\boldsymbol{Q}$ forms the orthonormal basis of a space of spectral data $\boldsymbol{R}$. Each spectrum of image represented by a corresponding vector $\boldsymbol{r}_{\mathrm{j}}$ can be expressed as

$$\mathbf{r}_{\mathrm{j}} = \sum_{k=1}^{n_F} u_{\mathrm{kj}} \mathbf{q}_{\mathrm{k}} \tag{3}$$

Because real spectral data are affected by experimental errors, determining the dimension of the factor space n_{F} is not a trivial problem. Malinowski[5] developed the theory of errors in factor analysis and divided a set of eigenvectors into two groups:

1. The primary eigenvectors $\boldsymbol{Q}^{\neq}_{\mathrm{k}}$, $k = 1 \rightarrow n_{\mathrm{F}}$
2. The secondary eigenvalues $\boldsymbol{Q}^{\mathrm{o}}_{\mathrm{k}}$, $k = n_{\mathrm{F}}+1 \rightarrow n_{\mathrm{s}}$

The set of primary eigenvectors $\boldsymbol{Q}^{\neq}_{\mathrm{k}}$ is directly related to the chemical information contained in a spectral data and defines the factor space basis with the dimension n_{F}. Reconstruction (3) using correct dimension of spectral space lead to the best reconstruction of spectral data with the lowest portion of experimental errors. The secondary eigenvalues are related exclusively to the experimental error in spectra data. Inclusion of secondary eigenvalues into the reconstruction (2) would lead to the reconstruction spectral data with excessive portion of experimental error

Various methods defining the dimension n_{F} have been developed[5,6]. The cross validation method using target factor analysis[5] is considered to be one of the most reliable approach.

Target Factor Analysis (TFA)[5] is a procedure projecting a test vector r_{l} to the primary factor space $\boldsymbol{Q}^{\neq}_{\mathrm{k}}$:

$$\boldsymbol{r}_{\mathrm{l}}^{*} = \boldsymbol{Q}^{\neq}_{\mathrm{k}}\ \boldsymbol{Q}^{\neq\,\mathrm{T}}_{\mathrm{k}}\ r_{\mathrm{l}} \tag{4}$$

where r_{l}^{*} is a projection of the test vector. The AET_{l} (apparent error of the target vector) is the measure of the difference between the target vector and its projection. TFA enables one to test individually, whether the particular spectrum (test) falls into the primary factor space.

In the cross validation method using target factor analysis a single spectral vector $\boldsymbol{r}_{\mathrm{l}}$ is removed from the spectral matrix $\boldsymbol{R}$. Resulting matrix $\boldsymbol{R}_{\mathrm{a}}$ (dimension n (n_{S}–1)) is submitted for principal component analysis, and the eigenvector set $(\boldsymbol{Q}_{\mathrm{m}})_{\mathrm{a}}$, $m = 1 \rightarrow n–1$ is obtained. Spectral vector $\boldsymbol{r}_{\mathrm{l}}$ is projected to the factor subspaces defined successively by first m vectors arranged in the submatrix $(\boldsymbol{Q}_{\mathrm{m}})_{\mathrm{a}}$, $m = 1 \rightarrow n–1$:

$$\boldsymbol{r}_{\mathrm{l}}^{*}(m) = \boldsymbol{Q}_{\mathrm{a}}(m)\ \boldsymbol{Q}_{\mathrm{a}}^{\mathrm{T}}(m)\ \boldsymbol{r}_{\mathrm{l}} \tag{5}$$

where $\boldsymbol{r}_{\mathrm{l}}^{*}$ is the reconstructed spectral vector. The above procedure is repeated until all spectral vectors (all columns of $\boldsymbol{R}$) have been reconstructed. The match between original and reconstructed spectra becomes closer with increasing dimension of factor subspace, e. g. with increasing number of eigenvectors m used in reconstruction (5). Reaching the arbitrary value of the chosen parameter of the match indicates the proper dimension of the factor space.

Results and discussion

The set of analyzed reference spectra of brown inks is on the Fig. 1. The set consists of five iron gall inks, three bistre inks and four sepia inks. Original reflectance spectra were transformed into Kubelka-Munk[7] spectra. Kubelka-Munk spectra are generally preferred in the methods using linear algebra[8]. Also, each spectrum was normalized to have maximum value equal one to enhance shape analysis. After the preliminary search a wavelength range 500–1100 nm was used.

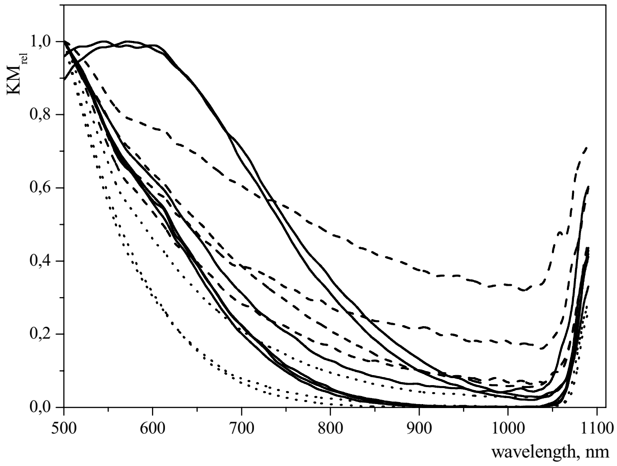

Fig. 1. **Set of spectra of reference samples of brown inks: solid lines – iron gall inks; dot lines – bistre inks; dashed lines – sepia inks**

First question to be solved is: Are the spectra of inks creating this set linearly independent? Only linearly independent spectra of individual components can be resolved.

The results of Cross Validation Analysis for the subset of five iron gall inks reference spectra are on the Fig. 2. We can see, that the standard deviation of the cross validation decrease until three eigenvectors are added and does not change significantly for the size of factor space 4 and 5. It suggests that the subset of reference iron gall inks spectra is created by three primary factors.

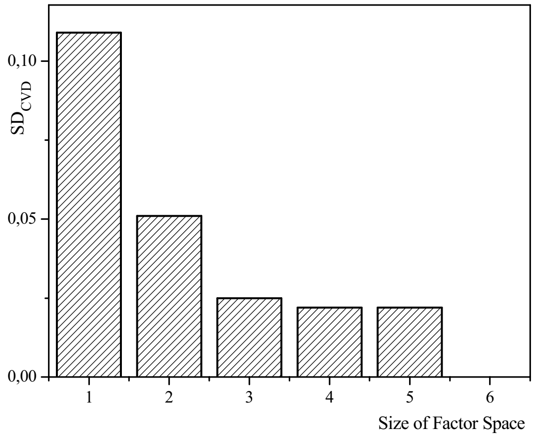

Fig. 2. **Cross Validation Analysis for the subset of iron gall ink reference spectra**

The same analysis for the subset of reference iron gall inks spectra with spectra of bistre inks added is on the Fig. 3. Estimated size of factor space in this case is 4, as the standard deviation decrease until four eigenvectors are added. This means, that addition of spectra of bistre inks increases the number of factors and so, the spectra of iron gall inks and bistre inks are linearly independent and can be resolved.

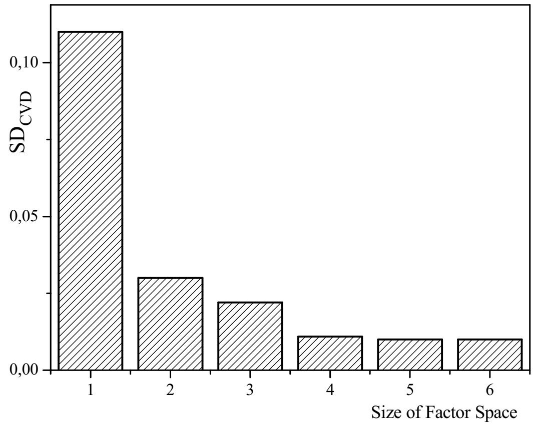

Fig. 3. **Cross Validation Analysis for the subset of iron gall ink reference spectra with spectra of bistre ink added**

The same results were obtained for Cross Validation Analysis of the subset of reference spectra of iron gall inks and sepia inks (Fig. 4.). The size of factor space of this subset of spectra is four, what means, that the spectra of iron gall inks and sepia inks are linearly independent and can be resolved.

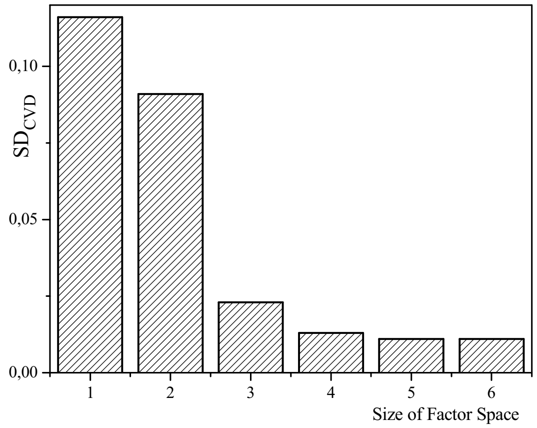

Fig. 4. **Cross Validation Analysis for the subset of iron gall inks reference spectra with spectra of sepia ink added**

Cross Validation Analysis was applied to the spectra taken at the four location of the drawing from 17th century

(Fig. 5.). Spectra of the drawing are presented on the Fig. 6. together with reference spectra of iron gall inks.

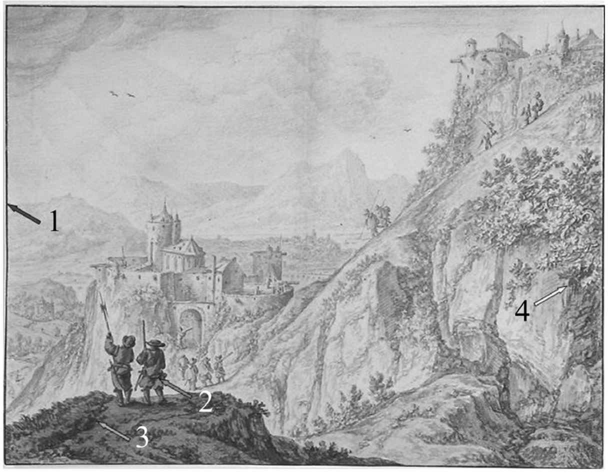

Fig. 5. **Mountain landscape with two fortresses by Herman Saftleven (1609–1685), Teylers Museum, Haarlem, The Netherlands, Inventory no. P49**

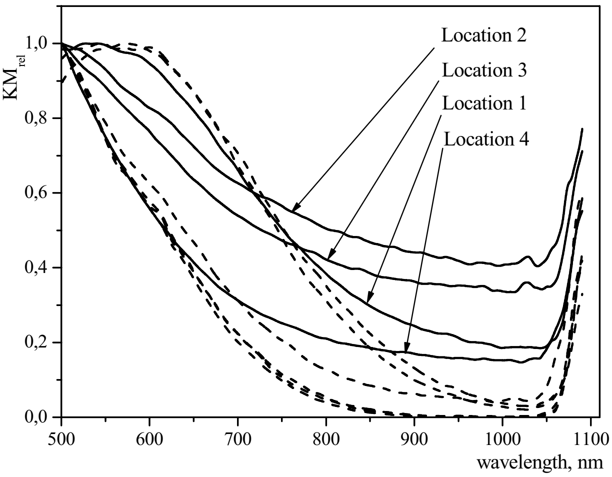

Fig. 6. **Spectra of the locations 1–4 of the drawing on the Fig. 5. (solid lines) and reference spectra of the iron gall inks (dash lines)**

Subset of spectra of reference iron gall inks with spectrum of location 1 has size of the primary factor space equal to three (Fig. 7A). It means that the drawing at the location 1 is composed of iron gall ink only.

Similar subsets of reference iron gall inks with spectra of locations 2, 3 and 4 added have size of the primary factor space equal to four (Fig. 7B, 7C, 7D). This means, that drawings at these locations are composed either of some other inks or of combination of other ink and iron gall ink. The Cross Validation analysis itself is not capable to distinguish these cases.

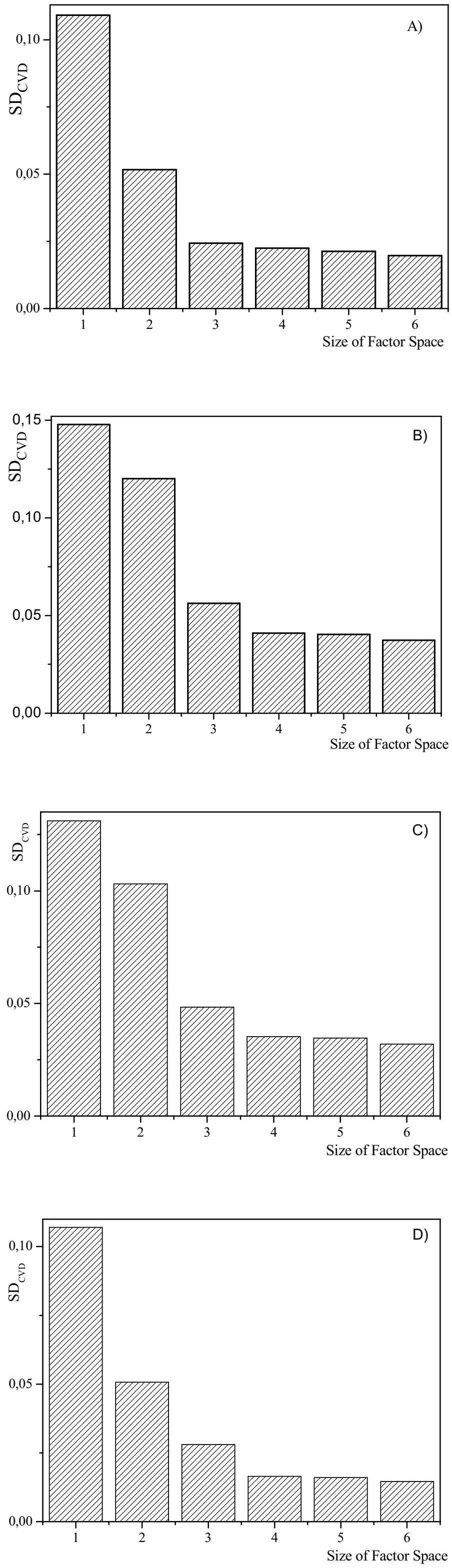

Fig. 7. **Cross Validation Analysis of subsets of spectra of reference iron gall inks with spectrum of location 1A, spectrum of location 2B, spectrum of location 3C and spectrum of location 2D**

Table I contains the AETs of Target Factor Analysis projections of the spectra of location 1, 2, 3 and 4 to the primary factor space of the reference iron gall inks spectra. While the errors of projections of the spectra of locations 1 and 4 are of the lower magnitude and indicate that the spectra of locations 1 and 2 contain spectra of iron gall inks, the errors of projections of the spectra of locations 2 and 3 significantly exceeding the SD_{CVD} (3) = 0.025 (Fig. 2.) of the Cross Validation of the set of reference iron gall inks indicates, that these spectra are not iron gall ink spectra.

Table I
AETs of Target Factor Analysis of spectra of locations 1, 2, 3 and 4

Location	AET
1	0.05
2	0.15
3	0.12
4	0.06

Based on the results of both Cross Validation Analysis and Target Factor Analysis the location 1 is composed of iron gall ink only, locations 2 and 3 do not contain iron gall ink and location 4 contains combination of iron gall ink and other ink.

This work was supported by Science and Technology Assistance Agency (Slovakia) under the contract No. APVT-20-034202.

Part of the research presented in this paper has been conducted within the European Project InkCor, *which was supported by funding from the European Commission, the 5th Framework Programme, the Key Action* City of tomorrow and cultural heritage *within the* Energy, environment and sustainable development programme, *Contract No. EVK4-CT-2001-00049*

The cooperation on this research was based on the thematic network of the 5th Framework Programme of the European Commission Transitional Metals in Paper (MIP), *Contract No. EVK4-2001-00215.*

REFERENCES

1. Corrigan C.: *Drawing Techniques,* in: *Old Master Prints and Drawings – A Guide to Preservation and Conservation* (Cohn M., ed.), pp. 76–78 Amsterdam University Press, 1997.
2. Neevel J. G.: *The Development of a New Conservation Treatment for Ink Corrosion Based on the Natural Anti-oxidant Phytate,* in: *Preprints of the 8th International Congress of IADA,* pp. 93–100, The Royal Danish Academy of Fine Arts, School of Conservation, Copenhagen 1995.
3. Neevel J. G., Mensch C. T. J.: *The Behaviour of Iron and Sulphuric Acid During Iron-Gall Ink Corrosion,* in: *Preprints of the 12th Triennal Meeting of the ICOM Committee for Conservation – Lyon, International Council of Museums,* (Bridgland J. , Brown J., ed), pp. 528–533, Paris, 1999.
4. http://www.avantes.com/Spectrometers/AvaSpec2048.htm.
5. Malinowski, E. R.: *Factor Analysis in Chemistry* (Third Edition), John Wiley and Sons, Inc., New York 2002.
6. Pelikán, P., Čeppan M., Liška M.: *Application of Numerical methods in Molecular Spectroscopy,* CRC Press, Boca Raton 1994.
7. Kubelka P., Munk F.: Zeits. f. Physik *12*, 593 (1931).
8. Čeppan M., Fedák J., Dvonka V., Veselý M., Zmeskal O.: J. Imag. Sci. Technol. *47*, 171 (2003).

L14 PHYSICAL CHEMISTRY OF FRACTAL STRUCTURE MATERIALS

OLDŘICH ZMEŠKAL, MARTIN VALA
and PAVEL BEDNÁŘ
Institute of Physical and Applied Chemistry, Faculty of Chemistry, Brno University of Technology, Purkyňova 118, 612 00 Brno, Czech Republic, zmeskal@fch.vutbr.cz

Introduction

Fractal geometry is widely used nowadays in many scientific areas. Fractals seem to be very powerful in describing natural objects on all scales. Fractal dimension and fractal measure, are crucial parameters for such description[1].

Fundamental laws describing the heat diffusion in fractal environment are discussed. It is shown that for the three-dimensional space the heat radiation process occur in structures with fractal dimension $0<D<1$, whereas in structures with $1<D<3$ heat conduction and convection have the upper hand (generally in the real gases).

It is shown that the results are comparable to the kinetics theory of real (ideal) gas (compressibility factor, Boyle's temperature)[2]. For the critical temperature the compressibility factor gains $Z=1$ (except for the ideal gas case $D=3$) also for the fractal dimension $D=1/\phi=1.618033989$, where ϕ is the golden mean value of the El Nashie's golden mean field theory[2].

Theoretical background

In papers[4,5,6] the density of fractal physical quantity $C(r)$ in E – dimensional Euclidean space E_n ($E=n$) (the density of heat capacity) was defined as

$$C(r) = k\,n(r) = k\,K\,r^{D-E}\,, \qquad (1)$$

where $n(r)$ is the coverage of space – distribution of particles concentration[4], $k=1.380658\ .\ 10^{-23}$ J K^{-1} is the quantum of heat capacity (Boltzmann constant), r is the radius of elementary quantity, K the fractal measure and D is the fractal dimension. For radial temperature field we can write the dependence of temperature on radius using (1), see (ref.[5]) as:

$$T_\mathrm{r}(r) = -\frac{\hbar c}{k} \cdot \frac{K\, r^{D-E+2}}{D(D-E+2)} \,. \tag{1}$$

From this equation it is obvious that in the space with constant density of the heat capacity *C*(*r*) (i. e. for $D=E$) the temperature increases with second power. In the case of point-like source of the heat radiation (i. e. for $D=E-3$, $E=3$) the temperature decreases with the distance by $1/r$. Assuming that there is linear source of heat (hot wire, $D=E-2$, $E=3$), the temperature is constant over the whole space.

It is evident that the density of the quantity (the density of heat capacity *C*(*r*)) depends on the fractal dimension *D*, on the fractal measure *K*, and on its distribution in the *E*-dimensional space. This distribution is expressed by Fig. 1a (in appropriate units). It turns out that, for the fully covered space ($D=E$) the distribution of the physical quantity is homogenous in the space. For the space where just one elementary cell is placed the charge density in the cell of size *r* is given by $\rho(r) = 1/r^\mathrm{E}$ (with the growing size of the cell, the coverage of space decreases). The dependence of the potential of physical field's radial part for different values of fractal dimension is presented on Fig. 1b. The potential of physical field (the temperature $T_r(r)$) is positive for $D<E-2$ and negative for $D>E-2$. For $D=E-2$ is potential (temperature) constant (in special case equal to zero: intensity of field is constant – homogenous field).

From the density of the heat capacity (1) and from the temperature (2) the density of energy

$$w(r) = C(r)T_\mathrm{r}(r) = -\hbar c \frac{K^2 r^{2(D-E+1)}}{D(D-E+2)} \tag{2}$$

respectively

$$w(T_\mathrm{r}) = K k T_\mathrm{r} \left[\frac{k T_\mathrm{r}\, D(E-D-2)}{K \hbar c} \right]^{\frac{E-D}{E-D-2}} \tag{3}$$

can be determined.

The heat radiation

Let's first consider the properties of heat transfer in the three-dimensional space ($E=3$) just for the fractal dimensions $D \in \langle 0.1)$ of the heat source. In this case, the heat density (4) can be written using generalised Planck radiation law

$$w(T_\mathrm{r}) = K k T_\mathrm{r} \left[\frac{k T_\mathrm{r}\, D(1-D)}{K \hbar c} \right]^{\frac{3-D}{1-D}} . \tag{4}$$

The power of the temperature T_r can gain values from interval $\langle 4, \propto)$.

The wavelength and the fractal dimension are connected by the following equation[7]

$$\bar{\alpha}_\mathrm{w} = \frac{\lambda}{\lambda_0} = \frac{1-D}{D} \,, \tag{5}$$

where $\bar{\alpha}_\mathrm{w} = \bar{\alpha} + 1$ is the inverse coupling constant of the mass energy ($\bar{\alpha}$ is the inverse coupling constant of energy[6]) and λ_0 is the wavelength for fractal dimension $D=1/2$ (maximum of function $D(1-D)$).

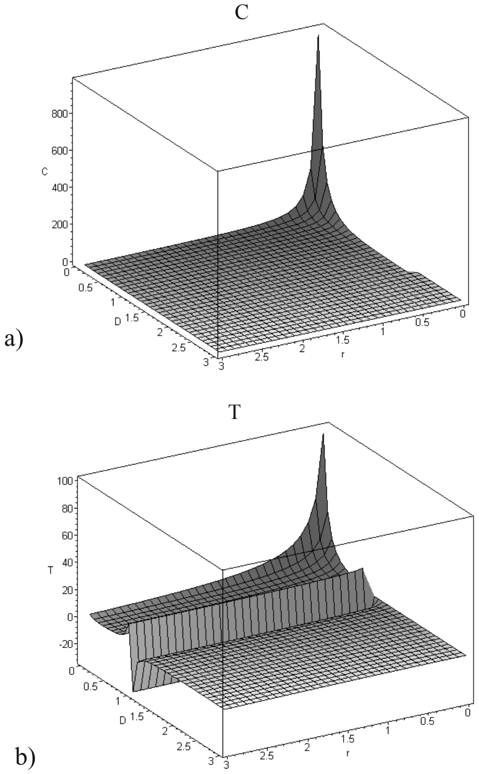

Fig. 1. **The dependences of physical quantities on the distance *r* and fractal dimension *D* for topological dimension *E*=3: a) the density of the heat capacity *C*(*r*, *D*), b) the temperature T_r(*r*, *D*)**

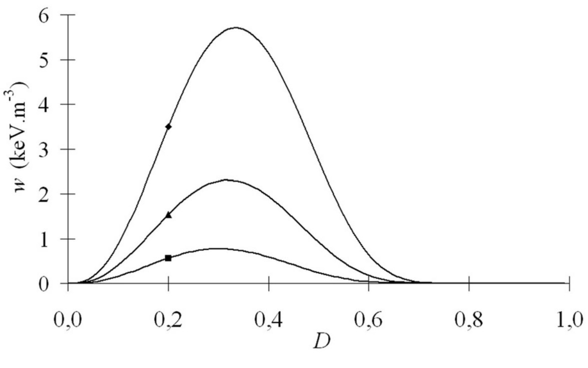

Fig. 2. **The dependency of energy density of heat oscillators on their fractal dimension plotted for three different temperatures (■*T*=4000 K, ▲*T*=5000 K, ♦*T*=6000 K) and constant number of oscillators (*K*=2.2 . 10^6 m^{-3})**

The Fig. 2. shows the dependency of the energy density on fractal dimension for a specific number of oscillators ($K \approx 2.2 \,.\, 10^6$ m^{-3}). The parameter of the dependences is temperature. Its values were chosen to allow comparison with experimentally gained values for the Sun.

Analysing the dependencies expressing the Planck's radiation law, similar results are obtained

$$w_\nu = \frac{\mathrm{d}w_\mathrm{s}}{\mathrm{d}\nu} = \frac{\lambda^2}{c}\frac{\mathrm{d}w_\mathrm{s}}{\mathrm{d}\lambda} = \frac{2\pi h\nu^3}{c^3\left[\exp\left(h\nu/kT\right)-1\right]} = \frac{2\pi h}{\lambda^3\left[\exp\left(hc/\lambda kT\right)-1\right]} \tag{6}$$

where $\nu = c/\lambda$ is the frequency of the electromagnetic wave.

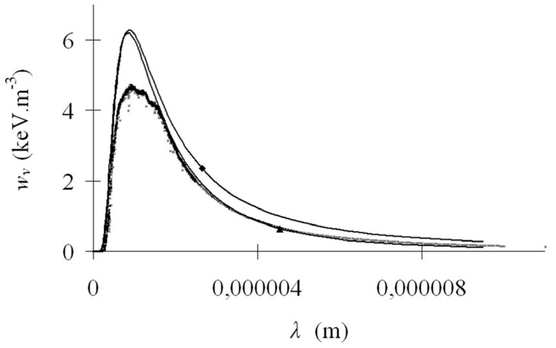

Fig. 3. **The spectral energy density of heat oscillators computed for temperature T=5800 K and K=2.53 . 10^6 m^{-3} using the Plank's radiation law (♦) and dependency defining the energy density of fractal structure (▲). The results are compared with measured values of the Sun**

The Fig. 3. shows the heat density dependency on wavelength (5) computed from Eq. 4 at temperature T=5800 K and assuming that $K\hbar c/kT \approx K\lambda_0 \approx 1$. Experimental results of Sun give (see Fig. 3.) better agreement with the fractal model than with the quantum theory calculations for higher wavelengths. The significant divergences around the maximum, which is at the visible part of the spectrum, are caused by the absorption in the atmosphere.

Heat conduction and flow

This kind of heat transport occurs when the fractal dimension lies in the interval $D \in (1.3\rangle$. In this case the $D(1-D)$ term in Eq. 4 is negative and relation for energy density, which in this case represents the gas pressure (i. e. $w(T_\mathrm{r}) = p(T_\mathrm{r})$), has to be rewritten into

$$p(T_\mathrm{r}) = K k T_\mathrm{r} \left(-1\right)^{\frac{3-D}{1-D}} \left[\frac{kT_\mathrm{r}\, D(D-1)}{K\hbar c}\right]^{\frac{3-D}{1-D}}, \tag{7}$$

where using the Moivre's theorem

$$\left(-1\right)^{\frac{D-3}{D-1}} = \exp\left(\mathrm{j}\pi\frac{D-3}{D-1}\right) = \cos\left(\frac{D-3}{D-1}\pi\right) + \mathrm{j}\cdot\sin\left(\frac{D-3}{D-1}\pi\right) \tag{8}$$

To describe the behaviour of real gases it is more practical to use the so-called compressibility factor. With the help of $p_\mathrm{id} = RT_\mathrm{r}/V_\mathrm{M} = KkT_\mathrm{r}$, where $V\mathrm{M} = \mathrm{N_A}/K$ is the molar gas volume, $R = k\,N_\mathrm{A}$ is the molar gas constant, N_A is the Avogadro constant, which represents the ideal gas equation, it can be defined by the equation

$$Z = \frac{p}{p_\mathrm{id}} = \frac{pV_\mathrm{M}}{RT_\mathrm{r}} = \left(-1\right)^{\frac{D}{1-D}} \left[\frac{kT_\mathrm{r}\, D(D-1)}{K\hbar c}\right]^{\frac{3-D}{1-D}}. \tag{9}$$

It is possible to establish from the dependency shown in the condition^2

$$\left(\frac{\mathrm{d}Z}{\mathrm{d}p}\right)_{T_\mathrm{B}} = \left(\frac{\mathrm{d}Z}{\mathrm{d}D}\right)_{T_\mathrm{B}} \left(\frac{\mathrm{d}D}{\mathrm{d}p}\right)_{T_\mathrm{B}} = 0 \tag{10}$$

,

so-called Boyle temperature (temperature at which real gasses behave as the ideal one – when the pressure is low or the volume is small). The minimum of the dependence (9) function arise when the fractal dimension $D = 3$. According to Eq. 9 we can thus write: $Z_\mathrm{B} = 1$, $T_\mathrm{B} = K\hbar c/6k$, $p_\mathrm{B} = K(K\hbar c)/6$.

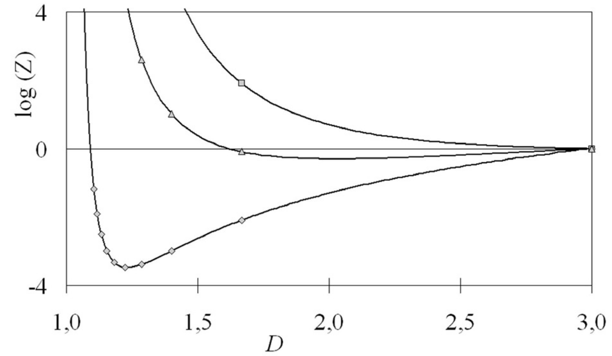

Fig. 4. **The dependency of compressibility factor size on fractal dimension plotted for three different temperatures ■T = 50 000 K, ▲T = 5000 K (i. e. for $K\hbar c \approx kT_\mathrm{r}$), ♦$T$ = 500 K, and constant number of oscillators (K=2.2 . 10^6 m^{-3})**

The dependency of the compressibility factor size on the fractal dimension at three different temperatures is plotted in Fig. 4. Assuming that the temperature is low the compressibility factor has a growing tendency straight away from the beginning (when the fractal dimension decreases). In the other cases the compressibility factor begins to grow only after previous decreasing period. At critical temperature the system ($K\hbar c \approx kT_\mathrm{r}$) gains $Z = 1$ (except for the case of the ideal gas $D = 3$) also for the fractal dimension $D = 1/\phi = 1.618033989$, where ϕ is the golden mean value of El Nashie's golden mean field theory.

Conclusion

The properties of heat radiation conduction and convection in fractal structures were discussed. It is shown that the dependency of energy density on fractal dimension

$w = \mathrm{f}(D)$ (4) is connected with the Planck radiation law (i. e. the spectral radiant excitance on wavelength $H_\lambda = \mathrm{f}(\lambda)$) for structures with fractal dimensions from the interval $D \in \langle 0.1)$.

On the other hand, structures with fractal dimensions $D \in (1.3\rangle$ behave as real gases. The energy density $w = \mathrm{f}(D)$ gains generally complex values within this interval (7) and describes the behaviour of a real (cohesive) gas. Only at specific values of fractal dimension the gas behave as the ideal one (the energy density is real-valued). Again, it was shown that in three-dimensional space ($E = 3$) at temperatures above the critical temperature ($kT > K\hbar c$) the maximum of the dependency $p = \mathrm{f}(D)$ (7) gives results reconcilable with the kinetic theory of real (ideal) gasses (van der Waals equation of state, compressibility factor, Boyle's temperature). At the critical temperature ($K\hbar c = kT_r$) the compressibility factor gains value $Z = 1$ (except for the case of $D = 3$) also for the fractal dimension $D = 1/\phi = 1.618033989$, which is the golden mean value of the El Nashie's golden mean field theory[3].

REFERENCES

1. Mandelbrot B. B.: *Fractal geometry of nature*. New York: W. H. Freeman and Co.; 1983.
2. Atkins P. W.: *Physical Chemistry*. Oxford University Press, 1998.
3. El Naschie M. S.: Chaos, Solitons & Fractals *16*, 353 (2004).
4. Zmeskal O., Nezadal M., Buchnicek M.: Chaos, Solitons & Fractals *17*, 113 (2003).
5. Zmeskal O., Nezadal M., Buchnicek M.: Chaos, Solitons & Fractals *19*, 1013 (2004).
6. Zmeskal O., Buchnicek M., Bednar P.: Chaos, Solitons & Fractals *22*, 985 (2004).
7. Zmeskal O., Buchnicek M., Vala M.: Chaos, Soliton & Fractals *25*, 941 (2005).

L15 STUDY OF HUMIC ACIDS FRACTIONATION

MARTINA KLUČÁKOVÁ
Institute of Physical and Applied Chemistry, Faculty of Chemistry, Brno University of Technology, Purkyňova 118, 612 00 Brno, Czech Republic, klucakova@fch.vutbr.cz

Introduction

Humic acids (HA) are natural compounds which cannot be characterized by chemical formula. They are not chemical individual but a heterogeneous mixture of various organic compounds. HA are traditionally defined according to their solubility in alkaline solutions[1–3]. In previous work[4] it was confirmed that it is possible to subdivide HA into their fraction by dissolving in buffer solution with various pH. The increasing alkalinity of buffers causes higher HA solubility and therefore large heterogeneity of extracted fractions. Because HA is a mixture of compound with various solubility and structure, the maximum absorbance of obtained fractions was not proportional to concentration of HA fraction in buffers. The maximum wavelength increased with pH-value, which could be caused by higher degree of condensation of aromatic cycles[4].

In this contribution some organic solvents were used for HA fractionation. In view of HA unique structure various polar and non-polar solvents were chosen for this study. The motivation for HA fractionation by organic solvents is the utilization of different solvents for extraction of HA, coal and other organic substances by some authors[5–7].

Experimental part

HA were isolated from South-Moravia lignite (Mikulčice) by alkaline extraction[8]. Soxhlet extractor and simple stirring of HA particles with organic solvent were used for HA fractionation. The solid/solvent ratio was 1 g/10 cm^3. HA were extracted by solvents always for 24 hours. Obtained fractions were analyzed by FT-IR spectroscopy as thin film on silicon plate (Nicolet Impact 400) and UV/VIS spectroscopy (Hitachi U-3300) as solution of HA in given solvent.

Results and discussion

Preliminary results from HA fractionation by organic solvents were published[9]. The yields of extraction in Soxhlet apparatus are listed in Table I. We can see that extraction yields for non-polar solvents are very low and the highest values were obtained for alcohols and acetates. On the other hand, no yield was observed in case of pentyl acetate. The highest value was obtained for extra pure ethanol. But if technical ethanol was used, extraction yield decreased to 2.08 %. Generally, polar solvent have higher efficiency of HA extraction than non-polar ones due to their lower hydrophobicity.

Calculated absorbance ratios A_{465}/A_{665} are also listed in Table I. This ratio (called also humification index) is most often used for characterization of humic substances. Its value for HA is usually <5 and decreases with increasing molecular weight and condensation degree. The majority of obtained fractions have humification index <5. Extremely high values (>10) were obtained for butyl acetate, heptanol and propanol. Probably, low molecular weight fractions are preferentially dissolved by these solvents. The lowest value was determined for toluene fraction, which has also the lowest extraction yield. No weight loss was observed in case of pentyl acetate, but the presence of small amount of HA fraction in this solvent was detected by UV/VIS spectroscopy. The maximum wavelength of HA fractions in non-polar solvents increases with dielectric constant from 226 nm to 297 nm. Alcohol solutions of HA have maximum wavelength between 210 nm and 220 nm except for 2-methyl-1-propanol (237 nm). HA fractions dissolved in acetates have maximum wavelength between 250 nm and 260 nm. Therefore acetates are probably able to dissolve HA fractions with higher degree of condensation of aromatic cycles. Differences between individual fraction were indicated also various tinges of colours.

Table I

Extraction yields in dependence on solvent polarity and UV/VIS characterization of obtained fractions (Soxhlet apparatus)

Solvent	Dielectric constant	Yield [% wt.]	A_{465}/A_{665}
hexane	0.72	1.30	2.00
benzene	0.33	2.30	1.07
toluene	2.40	0.01	0.71
xylene	2.45	0.37	1.31
hexyl acetate	4.42	2.30	4.57
pentyl acetate	4.79	0.00	1.86
butyl acetate	5.07	2.59	17.58
propyl acetate	5.62	4.52	5.10
ethyl acetate	6.08	2.60	4.54
methyl acetate	7.07	6.62	2.78
heptanol	11.75	6.52	22.17
2-methyl-2-propanol	12.47	4.12	7.24
hexanol	13.30	6.48	5.86
pentanol	15.13	4.01	6.18
butanol	17.84	5.53	4.62
2-methyl-1-propanol	17.93	4.33	7.27
propanol	19.75	2.79	47.75
ethanol	25.30	11.56	9.36
methanol	32.70	2.62	5.00

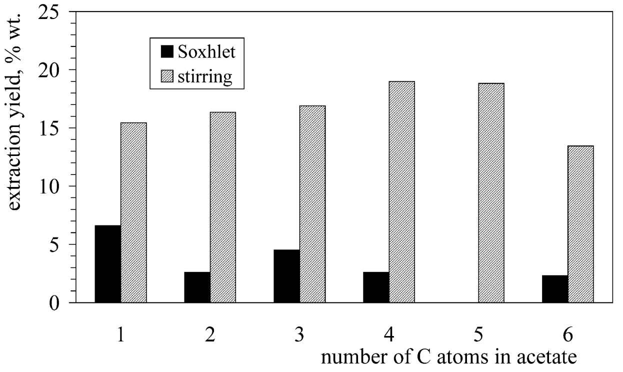

Fig. 1. **Comparison of HA extraction yields for stirring and Soxhlet apparatus**

Other way of HA extraction into organic solvents is mixing and stirring in closed vessel at laboratory temperature. It was observed that the efficiency of this method is much higher than the use of Soxhlet apparatus, which HA are extracted under relatively high temperatures in. The comparison of extraction efficiency of both methods is shown in Fig. 1. It is interesting that chain length causes positively on HA extraction by stirring but negatively in case of Soxhlet apparatus. Humification indexes for HA solutions obtained by stirring were always lower than value determined for Soxhlet apparatus. Their value was usually 1.5–3 for acetates and 2–6 for alcohols and it increased with chain length.

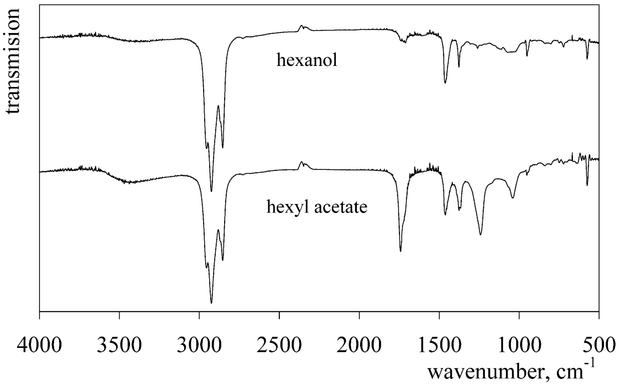

Fig. 2. **FT-IR spectra of HA fractions soluble in hexanol and hexyl acetate**

The comparison of FT-IR spectra of HA fractions in hexanol and hexyl acetate is shown in Fig. 2. Stretching vibration of aliphatic and OH groups are observed in region 3300–2600 cm^{-1}. Differences between both spectra in "fingerprint" area are clearly evident. Two peaks obtained for HA fraction in hexyl acetate between 1200–1000 cm^{-1} belong to anhydride and ester structures. It corresponds with the intensive absorption band about 1700 cm^{-1}. Similar results were obtained for other alcohols and acetates.

Conclusions

It was confirmed that HA are heterogeneous mixture of various compounds, which are partially soluble in organic solvents. Simple stirring HA with solvents was more effective than use of Soxhlet apparatus. The highest extraction yields were obtained for alcohols and acetates. UV/VIS and FT-IR spectra showed differences between individual fractions.

This work was supported by Grant Agency of Czech Republic – Project No. 104/02/D036.

REFERENCES

1. Schnitzer M., Kahn S. U.: *Humic Substances in the Environment.* Dekker, New York 1972.
2. Frimmel F. H., Christmann R. F.: *Humic Substances and Their Role in Environment.* Wiley, Chichester 1988.
3. Aiken G. A., McKnight M. D., Wershaw R. L., MacCarthy P.: *Humic Substances in Soil, Sediment and Water.* Wiley, New York 1985.
4. Klučáková M.: *Proceedings of International Scientific Conference Humic Substances in Ecosystems 5* (Gonet S S., Zaujec A., Debska B., eds.), p. *39*. Duszniki Zdroj 2003.
5. Fukushima M., Taga M.., Nakamura H..: Anal. Chim. Acta *289*, 223 (1994).
6. Nederlof M. M., van Riemsdijk W. H., Koopal L. K.: J. Colloid Inter. Sci. *135*, 140 (1990).
7. Rate A. W., McLaren R. G.: Environ. Sci. Technol. *27*, 1408 (1993).

8. Klučáková M., Kaláb M., Pekař M., Lapčík L.: J. Polym. Mater. *19*, 287 (2002).
9. Klučáková M., Zemanová A.: Chem. listy *96*, S77 (2002).

L16 Π-CONJUGATED POLYMERS BASED ELECTRONIC DEVICES

MARTIN WEITER[a], MARTIN VALA[a]
and STANISLAV NEŠPŮREK[a, b]
[a]Institute of Physical and Applied Chemistry, Faculty of Chemistry, Brno University of Technology, Purkyňova 118, 612 00, Brno, weiter@fch.vutbr.cz, [b]Institute of Macromolecular Chemistry, Academy of Sciences of the Czech Republic, Heyrovský Sq. 2, 162 06 Prague 6, Czech Republic

Introduction

In the last years the potential use of the semiconducting polymers for the construction of optoelectronic devices has stimulated considerable interest. New polymer materials are able not only to substitute the expensive crystalline semiconductors in these devices, but their specific properties originate the principle new devices and technologies. Good processability (film-forming) is utilized in many polymeric devices such as polymer electroluminescence diodes and displays, sensors and photodetectors, thin film transistors and solar cells. Nowadays the functional polymers are applied even in the logical circuits, which give rise to a new branch – “Plastic Logic”.

The aim of the proposed contribution is to introduce the recent results and experiences of our group dealing with the characterization of selected conjugated polymers for optoelectronic applications such as electroluminescence diodes, solar cells, photodetectors and light driven molecular current switches. In spite of much progress that has been made in the understanding of the underlying science that controls the properties of the devices, still relatively little is known about the optoelectronic properties of these materials. Therefore we focuse on detailed studies of physical processes e. g. photoconductivity[1–3] and photochromic phenomena[4] and their dynamics in π-conjugated polymers. Photoinduced charge generation, transport and recombination are key elementary processes underlying the function of these polymers in organic solar cells and light detectors. The electrical and optical properties of pristine π-conjugated polymers have been well characterized, which allow us to study the polymer blend comprising of hole conducting polymer and photochromic spiropyrane with high dipole moment in metastable form. This would provide better insight into the mechanism of carrier transport and thus would make way to improve device performance.

A relation between properties of individual molecules and properties of macroscopic molecular systems allows one to envisage construction of molecular-scale electronic devices. The switch should consist of a molecular transport material (molecular wire) with suitably attached side groups containing reversible photochromic moieties. The molecular wire should be realized by π-conjugated polymers. In these polymers the charge carrier delocalization and transport is influenced by resonant orbital phenomena. With reference to the photochromic moieties our interest is aimed to the class of molecules which dipole moments are strongly increased in the metastable forms. This feature allows control the heights of the potential barriers over the polymer chain, the level of conjugation and charge delocalization, and hence to change the on-chain mobility of charge carriers[4–6].

Experimental

The studied systems consisted of poly[2-methoxy, 5-(2’-ethyl-hexyloxy)-1,4-phenylenevinylene] (MEH-PPV), poly[2-methoxy, 5-(3’,7’-dimethyloctyloxy)-1,4-phenylenevinylene] (MDMO-PPV) or poly[(p-phenylenevinylene)--alt-(2-methoxy, 5-(2-ethylhexyloxy)-p-phenylenevinylene)] (MEHPO-alt-PV) doped at a broad range of dopant concentration by photochromic spiropyrane (SP; 6-nitro-1’,3’,3’-trimethylspiro[2H-1-benzopyran-2,2’-indoline]) or by trinitrofluorene (TNF). The electrical measurements were performed on a sandwich cell with a dielectric layer. It was prepared by spin coating of a 1% (by weight) polymer solution in chloroform onto an ITO (indium tin oxide) electrode. Top thick Al-layer served as a top electrode. The thickness of the layer was typically 150 nm. The multilayered devices were created by the introduction of an evaporated SP layer between a polymeric layer and electrode. In selected samples an electron and/or a hole transport layers were introduced between the active material and appropriate electrode. Dielectric properties were studied using a Hewlett Packard 4192A impedance analyzer. The time dependences of capacitance and conductance were recorded at constant frequency (1 kHz). The photochromic reaction was activated using a mercury discharge lamp HBO-200 with band filter (360 ± 20) nm and was studied by UV-VIS and photoluminescence spectroscopy. The measurements were performed in vacuum in the temperature range 298–350 K.

Results and discussion

In conjugated polymers containing suitable photochromic species the photochromic reaction should eventuate in changes of electrical properties such as conductivity. In molecular materials the transport of charge carriers are influenced by traps induced by non intentional or intentional dopants. Guest molecules will in general have different energy levels from the host. In particular, if ionization energies and electron affinities are suitably different, charge carrier traps can be formed. A special type of traps may occur if guest molecules possess a permanent dipole moment. The dipole moment contributes to the field acting on surrounding molecules and influences polarization energy. These dipolar traps are formed on neighbouring host molecules, even though the impurity itself does not necessarily form a chemical trap. As was mentioned above, the studied systems consisted of different types of π-conjugated poly(phenylenevinylene) derivatives with admixed photochromic spiropyran. Under irradiation spiropyran exhibits photochromism as shown in Fig. 1. The compound is stable in its colorless closed-ring isomeric form, while UV irradiation produces a metastable open-ring isomer (M) absorbing at 550–600 nm. The photoinduced color change of SP is caused by the extension of conjugation in the M isomer. Thermal fading in the dark or the reverse photochemical reaction following irradiation with a He-Ne laser gradually restores the original spectrum, the change being fully reversible. Dipole moments of stable forms of spiro molecules ranges typically within (2 ~ 5) D depending on substituents attached to their backbones, whereas the moments of the merocyanine form may exceed 10 D. Thus, during the SP → M photochromic reaction dipolar species are formed. As was mentioned above, in polymer matrix they can generate dipolar traps reducing the charge carrier mobility. Consequently, a decrease of the dark current and/or photocurrent can be observed. The formation of traps during the irradiation was checked by impedance measurements. The result is depicted in Fig. 2. During the illumination of the sample photocurrent decay was observed instead of expected current saturation; we attribute the phenomnon to the formation of the metastable species during the photochromic reaction. Simultaneously, the capacitance of the system was found to increase due to the formation of dipolar species. When the light was switched off, the rapid decrease of the photocurrent was observed, whereas the capacitance of the system was found to decrease slowly following the kinetics of the back ring closure reaction, M → SP. The rate constant of the process follows the Arrhenius equation with activation energy dependent on the polymer type matrix. The values are in a qualitatively good agreement with the results obtained from the optical measurements. We can conclude that photochromic transformation of spiropyran produced charge carrier traps affecting the electrical properties of the polymer matrix, capacitance and photoconductivity in particular. Thus, an optical signal can be transformed into an electrical one and a polymeric optron can be, in principle, constructed.

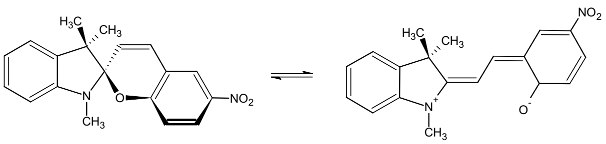

Fig. 1. **Photochromism of the spiropyrane molecule**

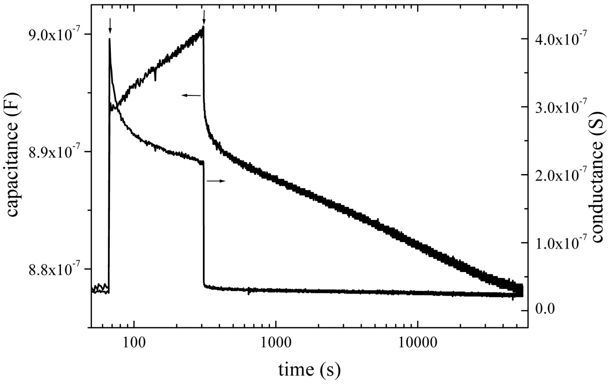

Fig. 2. **Time evolution of the conductance and capacitance of the sample measured by impedance spectroscopy at room temperature. The vertical arrows indicate the time when the UV irradiation was switched on and off, respectively**

This work was supported by the grant 203/03/133 from the Czech Science Foundation and by the project No. 0021630501 from the Ministry of Education, Youth and Sports.

REFERENCES

1 Weiter M., Arkhipov V. I., Bässler H., Synth. Met *141*, 165 (2004).

2. Weiter M., Bässler H., Gulbinas V., Scherf U., Chem. Phys. Lett. *379*, 177 (2003).

3. Weiter M., Bässler H., J. Photolum. *112*, 363, (2005).

4. Nešpůrek S., Sworakowski J., Wang G. and M. Weiter Appl. Surf. Sci., *234*, 14 (2004).

5. Nešpůrek, S., Sworakowski, J., Thin Solid Films, *393*, 168 (2001).

6. Nešpůrek, S., Toman, P., Sworakowski, J., Thin Solid Films, *438–439, 268* (2003).

L17 EXPERIENCE WITH ULTRASOUND SPECTROSCOPY IN BIOMATERIAL RESEARCH

MILOSLAV PEKAŘ[a], JIŘÍ KUČERÍK[a], TATIANA GLOUKHOVA[b] and DANIELA ŠMEJKALOVÁ[a]

[a]*Brno University of Technology, Faculty of Chemistry, Institute of Physical and Applied Chemistry, Purkyňova 118, 612 00 Brno, Czech Republic, pekar@fch.vutbr.cz,*

[b]*CPN, sro, 561 02 Dolní Dobrouč 401, Czech Republic, gloukhova@contipro.cz*

Introduction

Ultrasound has been used for a long time in colloid chemistry for particle sizing and measurement of electrokinetic potential[1]. Recently, so-called high resolution ultrasound spectrometer started to be available commercially, which substantially enlarged application potential of ultrasound in colloid chemistry[2]. Ultrasound spectrometry is based on detecting interactions of ultrasound wave with studied sample. Two parameters are measured – ultrasound velocity and ultrasound attenuation. Velocity is determined by local elasticity and density the former dominating, usually. Elasticity reflects local molecular organization and intermolecular interactions. Velocity thus probes intermolecular forces. Interpretation of attenuation is a little bit more complex. In heterogeneous samples attenuation is a result of ultrasound scattering on dispersed particles and can be used for their sizing. In homogeneous samples attenuation is due to some relaxation processes if there are any and can be thus used to follow, e. g., fast chemical processes.

High resolution refers to measurement of velocity. Whereas traditional equipments measure velocity with resolution about 0.1 m s^{-1} high resolution apparatus achieves 0.0001 m s^{-1} resolution, i. e. about 10^{-5} % in common aqueous solutions. Moreover, it enables measurement in various modes – kinetic, titration, programmed temperature. This makes high resolution device a powerful aid for colloid chemists. Examples of applications[3] include study of micellization, temperature induced conformation changes in polymer solutions, ligand binding to biopolymer, aggregation in biopolymer solutions, emulsion or suspension stability, gelation etc.

This contribution reports on some data from our first experience in application of high resolution ultrasound spectroscopy to two materials of nature or biological origin – humic (HA) and hyaluronic acids (HYA). The former have been subject of intensive studies of soil, coal, environmental, agriculture chemists for about 200 years yet their structure and detailed composition have not been resolved[4]. It is clear that humic acids is a complex mixture of hundreds or thousands of molecules, which are according to one hypothesis polymers[4] according to another one they are small molecules forming "supramolecular" aggregates[5]. Hyaluronic acid is found in some animal (including human) tissues and liquids where it plays indispensable role. Industrially produced hyaluronic acid is used mainly in medicine, pharmacy, cosmetics. Our aim is to apply ultrasound spectroscopy to characterize aqueous solutions of (sodium salts of) these natural colloids, particularly to study their aggregation behaviour and conformational changes induced by temperature or solution chemistry.

Experimental

Ultrasonic spectrometer HR-US 102 (Ultrasonic Scientific, Ireland) was used to measure the basic ultrasonic parameters. The device consists of two independent measuring cells, which were tempered at 25.00 °C. Experiments were realized in both cells, to avoid the effects associated with possible temperature fluctuations. Frequency used for the measurement was in all measurements 5478 kHz. Following sodium salt aqueous solutions were used: HA (1 g l^{-1}), HYA of molecular weight 29.8 kDa and 560 kDa with concentration 1.5 and 1.61 g l^{-1}, respectively. Further, to evaluate the influence of the electrolyte the latter solutions were prepared in 0.1 M NaCl with concentrations 1.5 g l^{-1}. In case of HA, 1 ml of the solution was placed into the ultrasound cell and 10 µl of 1 M NaCl was injected each approximately 12 minutes. Experiments with HYA were realized vice-versa – 10 or 20 µl of HYA solution was added to the 1 ml of either water or 0.1 M NaCl.

Results and discussion

Titrating solutions of both types of hyaluronic acid into the pure solvent gave only slight increase of ultrasound velocity with concentration. Titrating of hyaluronic solutions containing NaCl into the pure water resulted in much stronger increase (see example in Fig. 1.). Final concentration of both preparations was still under gelation threshold. In all cases, the change of velocity with concentration was practically linear. Linear change indicates no aggregation or conformation changes as expected for this highly hydrophilic material.

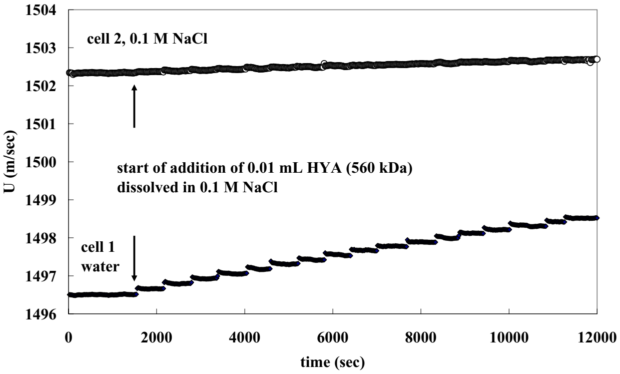

Fig. 1. **Change of ultrasound velocity upon titration of hyaluronic solution (560 kDa) into water or NaCl solution**

Strong increase of ultrasound velocity of electrolyte-containing solutions upon dilution with water (in comparison with experiments with aqueous solutions) means formation some more rigid structures. Generally, ultrasound velocity decreases in the order solids > liquids > gases. Diluting hyaluronate solution supports its dissociation. Formed charged particles, either hyaluronate anion or (more probably) sodium cation, are subsequently hydrated. Main effect on velocity increase should be probably attributed to sodium cations as indicates the much lower velocity increase in the cell containing NaCl solution. Water in hydration shells is less compressible, more rigid than bulk water molecules, which results in increase of ultrasound velocity. It can be thus speculated that the well-known affinity of hyaluronic acid to water is tightly connected to its dissociation and is promoted by it.

No principal qualitative differences were observed for solutions for the two molecular weight preparations. Differences in ultrasound velocities are negligible, thus interactions with ultrasound are dominated by the hydration shell, well developed around the hyaluronic backbone regardless its molecular weight.

Recently, we have reported on similar experiments made with sodium humate solution[6]. Titrating it into the water resulted in linear increase of ultrasound velocity indicating no structural changes, e. g. no aggregate forming. However, this may mean that stable aggregates are present in the concentration solution and do not disintegrate upon dilution.

Titrating sodium chloride solution into the sodium humate solution gave similar effect – increasing ultrasound velocity with increasing concentration of the electrolyte (Fig. 2.). It looks like simple dependence of ultrasound velocity of sodium chloride solution on its concentration. Sodium chloride thus behaves like really inert electrolyte, which probably does not penetrate humic structure, does not affect its electrostatic interactions in such a way, which would lead to conformational changes. On the other hand it should be expected that addition of electrolyte should influence electrical double layer on humic particles. These results may indicate that electrostatic interactions are not dominating in humic conformations or, perhaps, aggregation. Potential aggregates should be thus result of other intermolecular forces (hydrogen bonds, van der Waals forces, π-π interactions) as supposed by proponents of aggregate hypothesis[5].

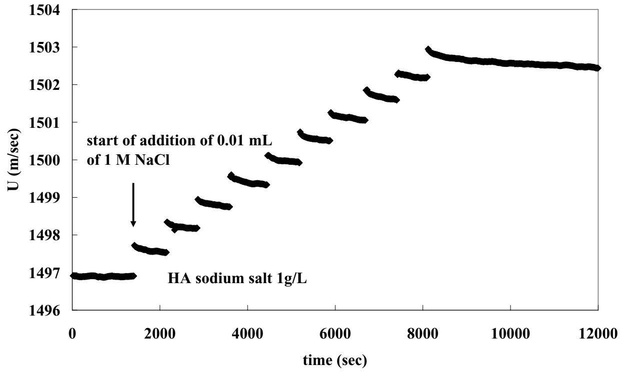

Fig. 2. **Change of ultrasound velocity upon titration of NaCl solution into the humic solution**

Conclusions

High resolution ultrasonic spectroscopy represents promising powerful method in the biomaterial research. It provides a wide scale of possible applications and enables to avoid problems associated with application of other techniques useful for molecular interactions research. On the other hand, in solutions of biomolecules many kinds of inter/intra molecular interactions, having strong influence on ultrasonic parameters, can be found. Hence, the interpretation of observed phenomena must be done very carefully and results of additional analytical techniques should be taken into account.

This work was supported by Ministry of Education, project no. MSM 0021630501.

REFERENCES

1. Dukhin A. S., Goetz P. J.: *Ultrasound for Characterizing Colloids.* Elsevier, Amsterdam, 2002.
2. Buckin V., O'Driscoll B., Smyth C., Alting A. C., Visschers R. W.: Spectroscopy Europe *15*, 22 (2003).
3. www.ultrasonic-scientific.com.
4. Stevenson F. J.: *Humus chemistry. Genesis, Composition and Reaction.* Wiley, New York 1994.
5. Piccolo A., Spiteller M.: Anal. Bioanal. Chem. *33*, 1047 (2003).
6. Pekař M., Kučerík J., Šmejkalová D., Klučáková M.: *Humic Science & Technology VIII.* Abstracts, p. 27. Northeastern University, Boston 2005.